AD_____

Award Number: W81XWH-04-1-0078

TITLE: Periscopic Spine Surgery

PRINCIPAL INVESTIGATOR: Kevin R. Cleary, Ph.D.

CONTRACTING ORGANIZATION: Georgetown University
                          Washington, DC 20057

REPORT DATE: January 2006

TYPE OF REPORT: Annual

PREPARED FOR: U.S. Army Medical Research and Materiel Command
               Fort Detrick, Maryland 21702-5012

DISTRIBUTION STATEMENT: Approved for Public Release;
                        Distribution Unlimited

REPORT DOCUMENTATION PAGE

Form Approved
OMB No. 0704-0188

Public reporting burden for this collection of information is estimated to average 1 hour per response, including the time for reviewing instructions, searching existing data sources, gathering and maintaining the data needed, and completing and reviewing this collection of information. Send comments regarding this burden estimate or any other aspect of this collection of information, including suggestions for reducing this burden to Department of Defense, Washington Headquarters Services, Directorate for Information Operations and Reports (0704-0188), 1215 Jefferson Davis Highway, Suite 1204, Arlington, VA 22202-4302. Respondents should be aware that notwithstanding any other provision of law, no person shall be subject to any penalty for failing to comply with a collection of information if it does not display a currently valid OMB control number. **PLEASE DO NOT RETURN YOUR FORM TO THE ABOVE ADDRESS.**

1. REPORT DATE 01-01-2006	2. REPORT TYPE Annual	3. DATES COVERED 22 Dec 2004– 21 Dec 2005
4. TITLE AND SUBTITLE Periscopic Spine Surgery		**5a. CONTRACT NUMBER**
		5b. GRANT NUMBER W81XWH-04-1-0078
		5c. PROGRAM ELEMENT NUMBER
6. AUTHOR(S) Kevin R. Cleary, Ph.D.		**5d. PROJECT NUMBER**
		5e. TASK NUMBER
		5f. WORK UNIT NUMBER
7. PERFORMING ORGANIZATION NAME(S) AND ADDRESS(ES) Georgetown University Washington, DC 20057		**8. PERFORMING ORGANIZATION REPORT NUMBER**
9. SPONSORING / MONITORING AGENCY NAME(S) AND ADDRESS(ES) U.S. Army Medical Research and Materiel Command Fort Detrick, Maryland 21702-5012		**10. SPONSOR/MONITOR'S ACRONYM(S)**
		11. SPONSOR/MONITOR'S REPORT NUMBER(S)

12. DISTRIBUTION / AVAILABILITY STATEMENT
Approved for Public Release; Distribution Unlimited

13. SUPPLEMENTARY NOTES
 Original contains colored plates: ALL DTIC reproductions will be in black and white.

14. **ABSTRACT**
The Periscopic Spine Surgery project was envisioned to lay the ground work for developing the physician assist systems of the future. These systems will incorporate robotics, tracking, and visualization to improve the precision of instrument placement and manipulation in minimally invasive procedures. This project has enabled the Georgetown team to become a world leader in the emerging fields of computer aided surgery and medical robotics. Our goal will continue to be to develop systems to add the physician in these demanding minimally invasive procedures with the ultimate aim of improving patient care. Key research accomplishments included: 1. Investigated methods for slice to volume registration of CT fluoroscopy images to provide image guidance for lung biopsy. 2. Completed an approved swine study in the CT procedure room demonstrating the feasibility of electromagnetic position sensing for image guidance. 3. Completed an initial accuracy study of electromagnetic position sensing in the CyberKnife suite and showed that relatively good accuracy could be obtained even with the LINAC (radiation beam) turned on. 4. Developed the software architecture and software implementation for an open source image-guided surgery toolkit. 5. Completed an initial study of workflow in the interventional suite for spinal nerve blocks.

15. SUBJECT TERMS
Minimally invasive procedures, technology development, medical robotics, electromagnetic tracking, workflow, open source software

16. SECURITY CLASSIFICATION OF:			17. LIMITATION OF ABSTRACT	18. NUMBER OF PAGES	19a. NAME OF RESPONSIBLE PERSON USAMRMC
a. REPORT U	**b. ABSTRACT** U	**c. THIS PAGE** U	UU	30	**19b. TELEPHONE NUMBER** *(include area code)*

Standard Form 298 (Rev. 8-98)
Prescribed by ANSI Std. Z39.18

1   Table of Contents

List of Figures

2   Introduction

This project is aimed at improving the state of the art of image-guided and minimally invasive procedures by developing a new generation of clinical techniques along with the computer-based hardware and software needed for their implementation. The focus of the project is to develop physician assist systems incorporating robotics, tracking, and visualization to improve the precision of instrument placement and manipulation in minimally invasive procedures. The project is led by the Imaging Sciences and Information Systems (ISIS) Center of the Department of Radiology at Georgetown University. Project collaborators include the Department of Radiation Medicine at Georgetown, the Urology Robotics Group at Johns Hopkins Medical Institutions, the NSF sponsored Engineering Research Center for Computer Integrated Surgical Systems and Technology at Johns Hopkins University, and the Engineering School at the Catholic University of America, as well as several commercial collaborators. Commercial collaborators include Kitware Inc., Traxtal Inc., Accuray Inc., and Siemens Medical Systems.

3   Report Body

This section describes the research accomplishments associated with each task in the statement of work. A brief overview will be given and the reader will be referred to the published papers in the appendix for more details. This is an annual report and includes research performed from December 22, 2004 to December 20, 2005. The award number is W81XWH-04-1-0078.

3.1 Task 1: Spinal Robotics for Precision Placement

This work has focused on two tasks: 1) continuation of the second phase of an FDA approved clinical trial for robotically assisted spinal nerve blocks; and 2) continued work in developing tracking algorithms for robotically assisted lung biopsy. As part of this work, Dr. Cleary recently completed an article on interventional robotic systems. This article is provided in the appendix [Cleary 2006].

As detailed in the last annual report, the initial clinical trial of 20 patients using the needle driver robot for spinal blocks was conducted at Georgetown University from August 2002 to December 2002. A picture of the robot is shown in Figure 1 and a picture of the first patient is shown in Figure 2. The work is in collaboration with the Urology Robotics Program at Johns Hopkins Medical Institutions (Dan Stoianovici, PhD). After some delays due to other pressing projects, we have started recruiting patients for this clinical trial and recently did four additional cases (we are approved for up to 80 additional patients but plan to collect 20 more patients at this point).
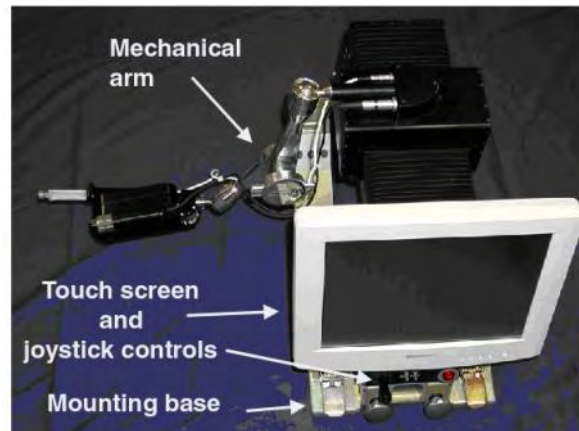
Figure 1: Robotic device showing mechanical arm and joystick control
(courtesy of Dan Stoianovici, PhD, Johns Hopkins Urology Robotics)
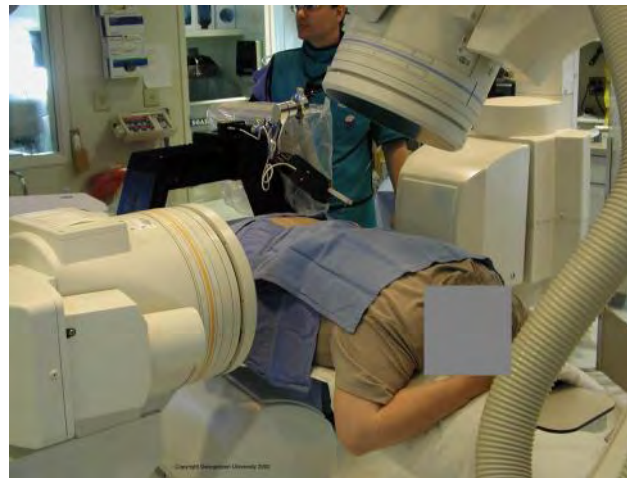
Figure 2: Clinical trial of robotic device for nerve and facet blocks at Georgetown University (interventional radiologist is Vance Watson, MD)

The robotically assisted lung biopsy work continues to evolve. The initial work on this project was done by Sheng Xu, PhD, who recently received his PhD from Johns Hopkins University. This work was collaboration with the NSF sponsored Engineering Research Center for Computer Integrated Surgical Systems and Technology at Johns Hopkins University (Russell Taylor, PhD). The work is being published and presented at the SPIE Medical Imaging 2006 conference this month (February 2006) and the abstract is reproduced in the next paragraph. Copies of this paper [Xu 2006] and the others are in the appendix.

Lung biopsy is a common interventional radiology procedure. One of the difficulties in performing the lung biopsy is that lesions move with respiration. This paper presents a new robotically assisted lung biopsy system for CT fluoroscopy that can automatically compensate for the respiratory motion during the intervention. The system consists of a needle placement robot to hold the needle on the CT scan plane, a radiolucent Z-frame for registration of the CT and robot coordinate systems, and a frame grabber to obtain the

CT fluoroscopy image in real-time (Figure 3). The CT fluoroscopy images are used to noninvasively track the motion of a pulmonary lesion in real-time. The position of the lesion in the images is automatically determined by the image processing software and the motion of the robot is controlled to compensate for the lesion motion. The system was validated under CT fluoroscopy using a respiratory motion simulator. A swine study was also done to show the feasibility of the technique in a respiring animal.
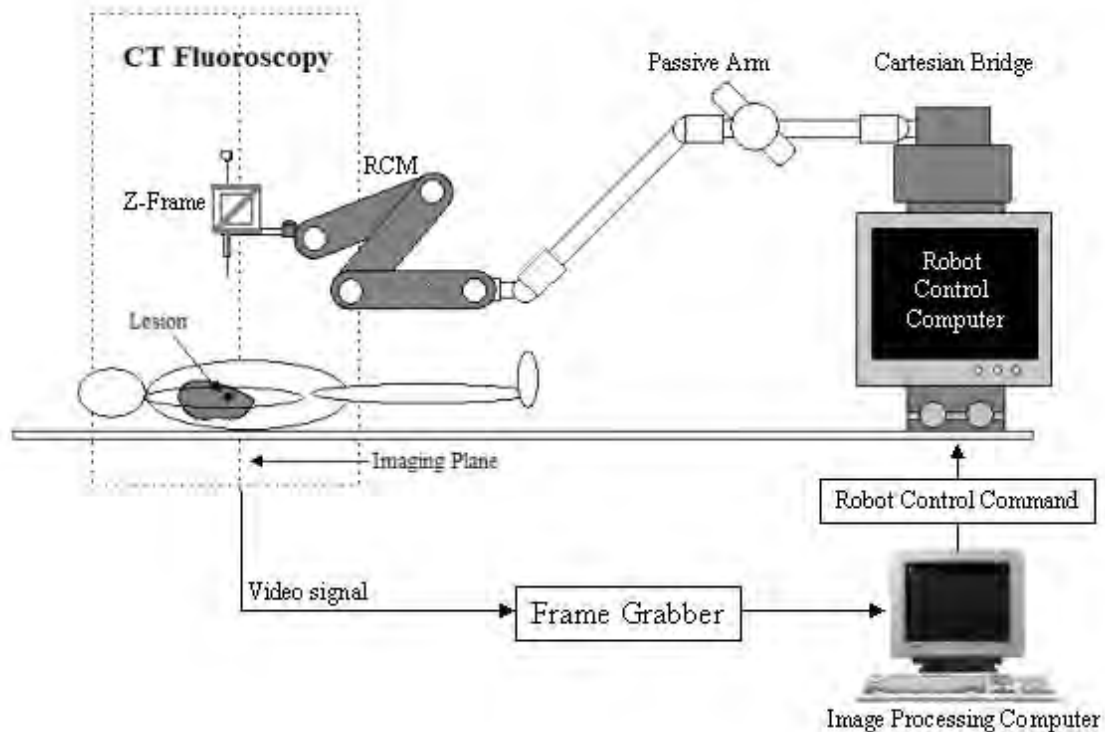
Figure 3: System components for robotically assisted lung biopsy using CT fluoroscopy

In addition to this work on developing tracking algorithms, we also began to investigate registration methods for merging CT fluoroscopy with the pre-procedure CT data set [Yaniv 2006a]. The details are given in the paper in the appendix and the abstract and some figures are reproduced below.

Lung cancer screening for early diagnosis is a clinically important problem. One screening method is to test tissue samples obtained from CT-fluoroscopy (CTF) guided lung biopsy. CTF provides real-time imaging; however on most machines the view is limited to a single slice. Mentally reconstructing the direction of the needle when it is not in the imaging plane is a difficult task. We are currently developing 3D visualization software that will augment the physician's ability to perform this task. At the beginning of the procedure a CT scan is acquired at breath-hold. The physician then specifies an entry point and a target point on the CT. As the procedure advances the physician acquires a CTF image, at breath-hold; the system then registers the current setup to the CT scan, enabling comparison between the plan and current situation. As the CT and CTF data are acquired at different breath-holds we expect them to exhibit

displacements of up to 4mm. To assess the performance of different registration algorithms for CTF/CT registration we propose to use simulated CTF images. These images are created by deforming the original CT volume and extracting a slice from it. Realistic deformation of the CT volume is achieved by using positional information from electromagnetically tracked fiducials, acquired throughout the respiratory cycle. To estimate the dense displacement field underlying the sparse displacement field provided by the fiducials we use radial basis function interpolation. Finally, we evaluated Thirion's "demons" algorithm, as implemented in ITK, for the task of slice-to-volume registration. We found it to be unsuitable for this task, as in most cases the recovered displacements were less than 50% of the original ones. As part of this task, we developed an algorithm for segmentation of the lung region as shown in Figure 4.
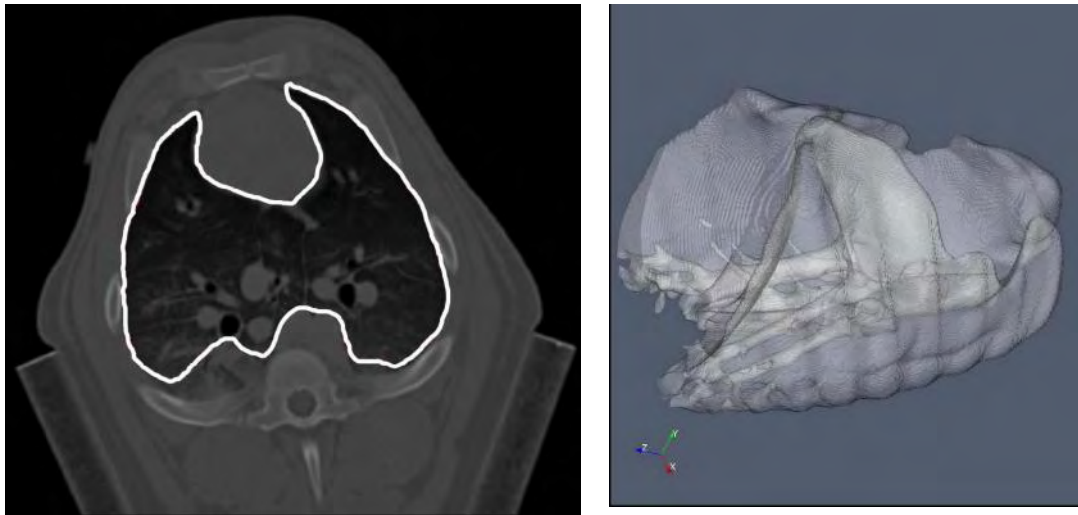
Figure 4: Segmentation of lung region from CT data set (left side) and volume rendering of segmented region (right side)

3.2 Task 2: Organ Tracking using Electromagnetic Position Sensing

The goal of this task is to investigate the use of electromagnetic tracking for precisely locating internal organs such as the liver during interventional procedures. This is an ongoing collaboration with Northern Digital (Waterloo, Canada) and Traxtal Technologies (Bellaire, Texas). Northern Digital has developed the AURORA™ electromagnetic tracking system, which enables instruments that are fitted with a sensing coil to be tracked and overlaid on an image of the anatomy. Our research group at Georgetown served as a beta test site and was one of the first research groups worldwide to receive this equipment (Figure 5). The system has recently been released as a commercial product and we are actively pursuing several applications with this technology.
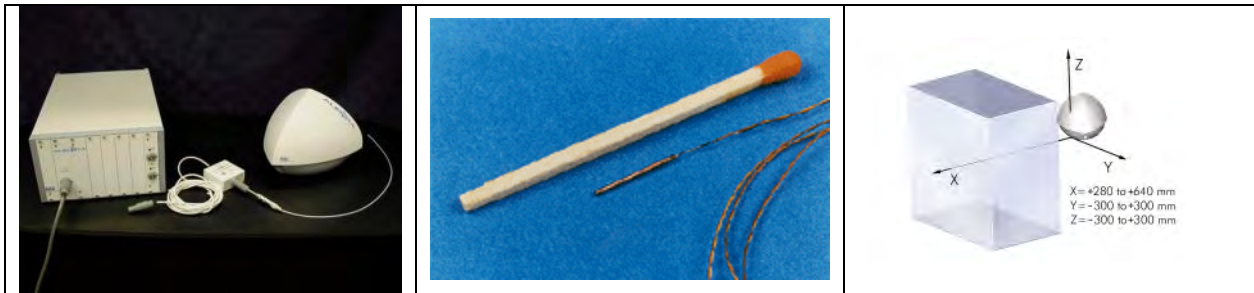
Figure 5: AURORA™ sensors, electromagnetic tracking system components, and measurement volume
The left picture shows (from left to right) the control unit, sensor interface device, and electromagnetic field generator. The middle picture shows the sensor coils along with the electrical wires protruding from the coil, compared to a match. The right picture shows the measurement volume in mm relative to the location of the field generator. (Photos courtesy of Northern Digital, Inc.)

In the past year, we have focused on developing this technology for liver procedures in the CT suite. As part of this research, we have developed an image-guided surgery system incorporating electromagnetic tracking. Figure 6 shows the tracking system as recently used in an approved swine study in the CT suite. Electromagnetic tracking of instruments in the interventional suite enables image overlay of preoperative CT scans and provides multimodality guidance while decreasing x-ray dose.

Figure 6: Swine study in CT suite with tracking of instruments and virtual overlay on monitor (interventional radiologist is Filip Banovac, MD)

In addition to this study in the CT suite, we carried out extensive experiments to characterize the performance of electromagnetic tracking in the fluoroscopy procedure room as well [Yaniv 2006b]. The abstract and a figure are reproduced below.

Tracking organ motion due to respiration is important to enable precise interventions in the regions of the abdomen and thorax. Respiratory induced motion in these regions may limit the accuracy of interventions which do not employ some type of tracking. One method of tracking organ motion is to use a predictive model based on external tracking that is correlated to internal motion. This approach depends on the accuracy of the model used for correlating the two motions. Ideally, one would track the internal motion directly. We are investigating the use of electromagnetically tracked fiducials to enable real-time tracking of internal organ motion. To investigate the in-vivo accuracy of this approach we propose to use stereo-fluoroscopy. In this paper we show that stereo-fluoroscopy is accurate enough to serve as a validation method, displaying sub-millimetric accuracy (maximal error of 0.66mm). We study the effect of the bi-plane fluoroscopes on the electromagnetic systems' accuracy, and show that placing the bi-plane fluoroscopes in a typical intra-operative setup has a negligible effect on the tracking accuracy (maximal error of 1.4mm). Finally, we compare the results of stereo-fluoroscopy tracking and electromagnetic tracking of needles in an animal study, showing a mean (std) difference of 1.4 (1.5) mm between modalities. These results show that stereo-fluoroscopy can be used in conjunction with electromagnetic tracking with minimal effect, and that the electromagnetic system is accurate enough for motion tracking of internal organs. A picture of the test setup is shown in Figure 7.

Figure 7: Electromagnetic tracking study in biplane fluoroscopy suite showing both fluoroscopes, dummy torso and moving liver, electromagnetically tracked needles embedded in liver, and electromagnetic field generator

3.3 Task 3: Tracking for Radiation Treatment

Organs in the abdomen and thorax move and deform during respiration, and these changes place a severe limitation on the effectiveness of radiation medicine in the lungs, liver, and pancreas. Georgetown University Medical Center is an emerging leader in a new form of radiosurgery for these types of tumors. These treatments are enabled by two key technologies: (1) the CyberKnife, a precision radiosurgery machine based around a compact linac and a robotic positioning arm, and (2) Synchrony, a system for optically tracking respiratory motion and steering the radiation beam to follow a moving tumor. This research is being carried out in conjunction with the Radiation Medicine Department at Medstar Georgetown University Hospital.

**Figure 8: Photograph of CyberKnife Stereotactic Radiosurgery System
(Accuray, Sunnyvale, CA)**

As part of this task, we performed an accuracy evaluation of electromagnetic tracking in the CyberKnife suite [Wilson 2006]. Electromagnetic trackers have found inroads into medical applications as a tool for navigation in recent years. Their susceptibility to interference from both electromagnetic and ferromagnetic sources has prompted several accuracy assessment studies in past years. To the best of our knowledge, this is the first accuracy study conducted to characterize measurement accuracy of an NDI AURORA electromagnetic tracker within a CyberKnife radiosurgery suite. This paper uses a data collection protocol to collect uniformly distributed data points within a subset of the AURORA measurement volume in a CyberKnife suite. The key aim of the study is to determine the extent to which large metal components of the CyberKnife stereotactic radiosurgery device and robot mount contribute to overall system performance for the AURORA electromagnetic device. A secondary goal of the work is to determine the variation in accuracy and device behavior with the presence of ionizing radiation when

the LINAC is turned on.   The test setup in shown in Figure 9 and the details of the experiments can be found in the paper in the appendix [Wilson 2006].
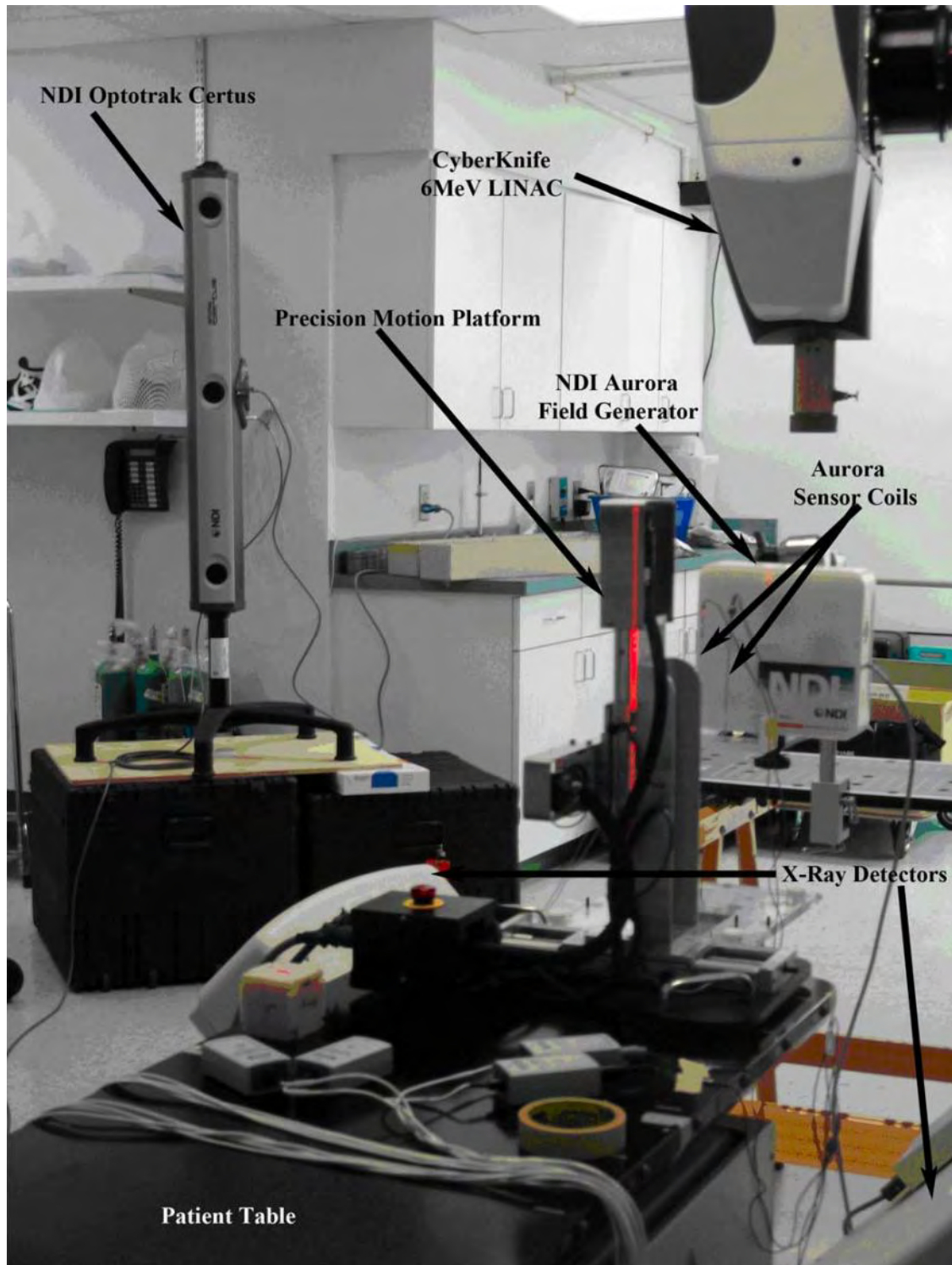

Figure 9: Test setup within the CyberKnife suite

3.4 Task 4: Rehabilitation Robotics

The primary goal of this effort is to develop robotic systems for assessment and physical therapy. The secondary goal is to expand this capability to the Internet. We currently have several projects in rehabilitation robotics spanning three robotic testbeds described briefly below. We will continue to expand our activities in this area through ongoing collaborations with the National Rehabilitation Hospital, the University of Maryland, the Center of Excellence for Remote and Medically Under Served Areas (CERMUSA), and Interactive Motion Technologies, Inc. As some of these devices may be controlled through the Internet, a systematic study of information assurance and vulnerabilities will be an integral part of this effort. Details of this work are provided in the three papers in the appendix: [Carignan 2005], [Roderick 2005], and [Tang 2005].

3.4.1 InMotion2 Robot

We are currently using the IM2 testbed for two projects: a neuroscience clinical trial and telerobotic rehabilitation over the Internet. The first project is to test sensorimotor adaptation of subjects when exposed to kinematic and force distortions (Figure 10). The eventual goal of this project is to develop therapy for Parkinsonian patients. The trial is now complete and we are currently processing the data. The second project is to develop cooperative, functional rehabilitation for populations with neurological deficits using virtual reality technologies. We have developed several tasks, the most recent is a cooperative tandem canoe task that can be performed over the Internet between patient and therapist (Figure 11).
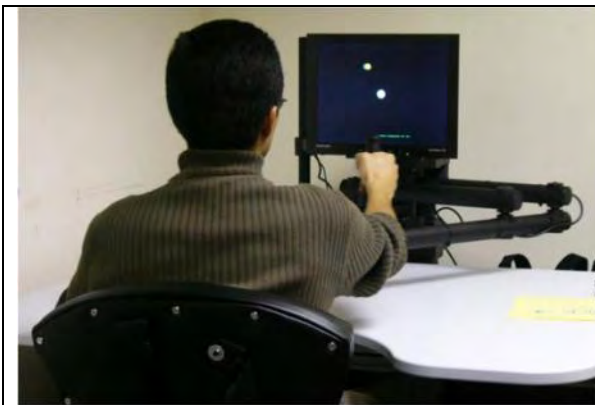
| **Figure 10: Operator interface being used for sensorimotor clinical trial.** | **Figure 11: Cooperative tandem canoe task using InMotion2 Robot.** |

3.4.2 MGA Arm Exoskeleton

We are currently building an upper arm robotic exoskeleton for shoulder rehabilitation. This project is a joint venture between CAIMR and the Space Systems Laboratory (SSL) at the University of Maryland. The mechanical hardware was designed and built by the SSL robotics group, and CAIMR is developing the electronics and control system. The hardware for the exoskeleton has been built (Figure 12 and Figure 13), and the system is

currently undergoing electronic integration. We expect operation to begin in the summer of 2006.

| **Figure 12: Exoskeleton prototype being test fitted on human subject.** | **Figure 13: Close-up of the exoskeleton shoulder rotation assembly.** |

3.4.3 Keiser Arm Curl Machine

We are developing an actively controlled exercise machine for elbow rehabilitation. A Keiser Arm Curl 250 was retrofitted with a motor and lead screw assembly as shown in Figure 14. Resistance laws were programmed on a PC and an admittance controller outputs commands to the motor. Preliminary results for simulating free weight and viscoelastic resistances were encouraging (Figure 15). Future clinical work will focus on designing resistance laws tailored for individual rehabilitation of the hand/elbow following surgery.

| **Figure 14: Keiser Arm Curl 250 retrofitted with SmartMotor actuator.** | **Figure 15: Experimental results for simulating free weight repetition.** |
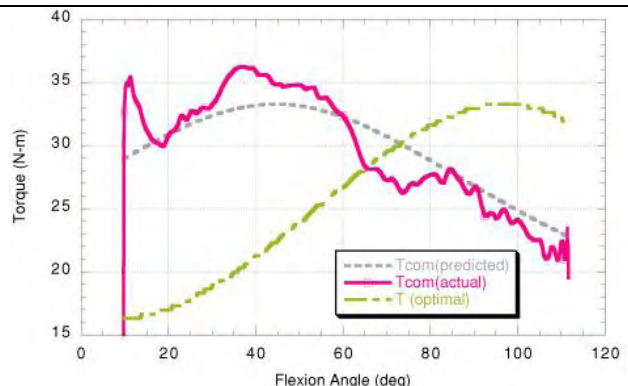
3.5 Task 5: Interventional Suite of the Future

The goal of this task is to develop the integrated interventional suite of the future. This task is a follow-up to the OR2020 workshop (Operating Room of the Future) organized by Dr. Cleary in March 2004. During the past year, we have worked with Georgetown University Hospital and MedStar Health to issue a purchase order for a new interventional suite in the Department of Radiology. This suite is based on a Siemens angiography system with a flat panel detector. The flat panel provides greater dynamic range which should enable better visualization of soft tissue during image-guided interventions. We are currently working out the details of a research agreement with Siemens to integrate the electromagnetic tracking technology described above into this new interventional suite.

In related work, we have been developing the software architecture for an open source toolkit for image-guided surgery (IGSTK). This software project is jointly funded by the National Institute for Biomedical Imaging and Bioengineering at NIH. The open source movement is growing in popularity since it allows researcher to easily share software and avoids duplication of effort. Since software is increasingly important in medical research, open source can greatly improve the productivity of research groups.

The IGSTK project will be demonstrated this month (February 2006) at the SPIE Medical Imaging Conference in San Diego. The Image-Guided Surgery Toolkit (IGSTK) is an open source software toolkit based on ITK, VTK, and FLTK, and uses the cross-platform tools CMAKE and DART to support common operating systems such as Linux, Windows, and MacOS. IGSTK integrates the basic components needed in surgical guidance applications and provides a common platform for fast prototyping and development of robust image-guided applications. The paper in the appendix gives an overview of the IGSTK framework and current status of development followed by an example needle biopsy application using this toolkit [Cheng 2006].

Figure 16: IGSTK open source toolkit screen shot

3.6 Task 6: Nano-Technology Medical Sensors

This task is to develop a nano-sensor that can be used on a probe tip to assess cell death in applications such as targeted drug or radiation therapy. This is a new collaboration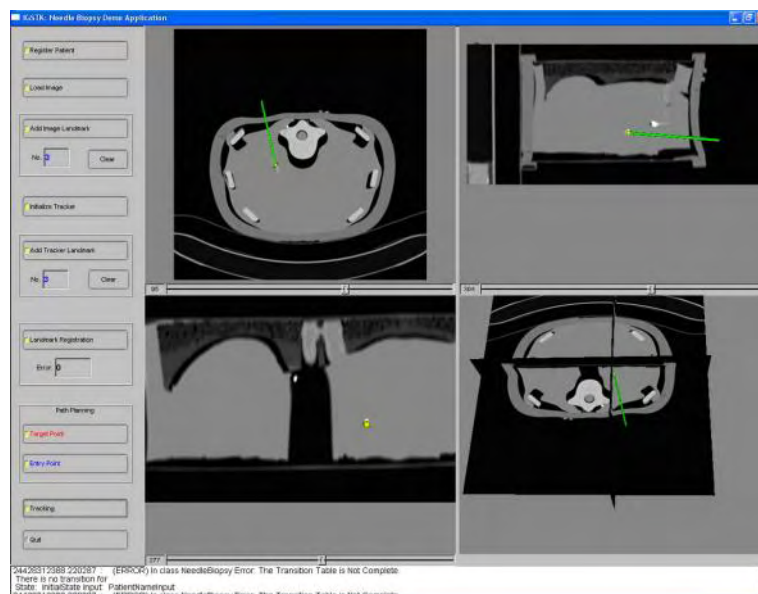 with the Physics Department at Georgetown and Professor John Currie, who is an expert in micro-fabrication techniques. Unfortunately, due to time constraints on Dr. Currie and several other pressing projects in his laboratory, this task has not made progress during the past year. However, we have had recent renewed discussions with Dr. Currie and are optimistic about moving this project forward in 2006.

3.7 Task 7: Grid Computing & Electronic Patient Record

This project is a medical informatics task to look at the electronic patient record and the use of emerging technologies such as grid computing to provide a seamless repository of clinical records. During the past year, we have begun this task by establishing a workflow project in interventional radiology to track patient cases during spinal nerve blocks. The idea is that workflow analysis can show us where the bottlenecks are in the system and what information is needed at what time and in what place. Our initial workflow results will be reported at SPIE Medical Imaging 2006 [Siddoway 2006] and are summarized here.

Workflow management has the potential to dramatically improve the efficiency and clinical outcomes of medical procedures. In this study, we recorded the workflow for nerve block and facet block procedures in the interventional radiology suite at Georgetown University Hospital in Washington, DC, USA. We employed a custom client / server software architecture developed by the Innovation Center for Computer Assisted Surgery (ICCAS) at the University of Leipzig, Germany. This software runs in an internet browser, and allows the user to record the actions taken by the physician during a procedure as shown in Figure 17. The data recorded during the procedure is stored as an XML document, which can then be further processed. We have successfully gathered data on a number if cases using a tablet PC with a touch screen, and these preliminary results show the feasibility of using this software in an interventional radiology setting. We are currently accruing additional cases and when more data has been collected we will analyze the workflow of these procedures to look for inefficiencies and potential improvements.

Figure 17: Interface screen for recording workflow during spinal nerve blocks

4 Key Research Outcomes

This section provides a bulleted list of key research accomplishments during the entire project:

- Investigated methods for slice to volume registration of CT fluoroscopy images to provide image guidance for lung biopsy

- Completed an approved swine study in the CT procedure room demonstrating the feasibility of electromagnetic position sensing for image guidance

- Demonstrated an accuracy of 1.4 mm with a standard deviation of 1.5 mm for electromagnetic position sensing in the interventional suite using biplane fluoroscopy

- Completed an initial accuracy study of electromagnetic position sensing in the CyberKnife suite and showed that relatively good accuracy could be obtained even with the LINAC (radiation beam) turned on

- Developed the software architecture and software implementation for an open source image-guided surgery toolkit

- Completed an initial study of workflow in the interventional suite for spinal nerve blocks

5 Reportable Outcomes

This section provides a list of reportable outcomes. The major product of this year is the list of papers given in Section 7 (References). Copies of these documents are provided in the appendix.

In addition, several proposals to the National Institutes of Health were submitted based on this work. Several small business grants were received with company partners, including one on electromagnetic tracking for the CyberKnife suite.

A master's student from Catholic University (Emmanuel Wilson) was supported for the electromagnetic tracking work in CT and the CyberKnife suite. A PhD student from Johns Hopkins University (Sheng Xu) was supported to assist in software development for the robotic needle driver. The research group at Georgetown continued to take a lead in the Washington Area Computer Aided Surgery Society (www.washcas.org), which was formed in 2000 to promote research in the field.

6 Conclusions

The Periscopic Spine Surgery project has continued to lay the ground work for developing the physician assist systems of the future. These systems will incorporate robotics, tracking, and visualization to improve the precision of instrument placement and manipulation in minimally invasive procedures. We have begun to show the feasibility of electromagnetic position sensing and image overlay in the clinical environment and plan to apply for FDA approval soon. We have reached an agreement to install a new angiography suite at the hospital incorporating a flat panel detector and many of our future activities will be focused here. We have continued our work on respiratory motion compensation as a theme which cuts across many of our efforts. This project has enabled the Georgetown team to become a world leader in the emerging fields of computer aided surgery and medical robotics. Our goal will continue to be to develop systems to add the physician in these demanding minimally invasive procedures with the ultimate aim of improving patient care.

7   References

[Carignan 2005]   Craig Carignan, Micheal Liska, and Stephen Roderick, "Design of an Exoskeleton with Scapula Motion for Shoulder Rehabilitation," *Proc. IEEE Int. Conf. on Advanced Robotics (ICAR),* Seattle, 524-531, July 2005.

[Cheng 2006]   Peng Cheng, Hui Zhang, Hee-su Kim, Kevin Gary, M. Brian Blake, David Gobbi, Stephen Aylward, Julien Jomier, Andinet Enquobahrie, Rick Avila, Luis Ibanez, and Kevin Cleary, "IGSTK: Framework and Example Application Using an Open Source Toolkit for Image-Guided Surgery Applications," presented at the *SPIE Medical Imaging Symposium* and to be published in the *PACS and Imaging Informatics* track, San Diego, CA, 11-16 February 2006.

[Cleary 2006]   Kevin Cleary, Vance Watson, Dan Stoianovici, Gernot Kronreif, and Andreas Melzer, "Interventional robotic systems: applications and technology state-of-the-art," *Minimally Invasive Therapy and Allied Technology,* Volume 15, Issue 2, Taylor & Francis, 2006.

[Roderick 2005]   Stephen Roderick and Craig Carignan, "An Approach to Designing Software Safety Systems for Rehabilitation Robots," *Proc. Int. Conf. on Rehabilitation Robotics (ICORR)*, Chicago, 252-257, June 2005.

[Siddoway 2006]   Donald Siddoway, Mary Lou Ingeholm, Oliver Burgert, Thomas Neumuth, Vance Watson, and Kevin Cleary, "Workflow in Interventional Radiology: Nerve Blocks and Facet Blocks," presented at the *SPIE Medical Imaging Symposium* and to be published in the *PACS and Imaging Informatics* track, San Diego, CA, 11-16 February 2006.

[Tang 2005]   Jonathan Tang, Craig Carignan, Shailesh Gattewar, "Virtual Environment for Robotic Tele-Rehabilitation," *Proc. Int. Conf. on Rehabilitation Robotics (ICORR)*, Chicago, 365-370, June 2005.

[Wilson 2006]   Emmanuel Wilson, Rebecca Slack, Filip Banovac, Sonja Dieterich, Hui Zhang, and Kevin Cleary, "Electromagnetic tracker accuracy in the CyberKnife suite," presented at the *SPIE Medical Imaging Symposium* and to be published in the *Visualization, Image-Guided Procedures, and Display* track, San Diego, CA, 11-16 February 2006.

[Xu 2006]   Sheng Xu, Gabor Fichtinger, Russell H. Taylor, Filip Banovac, and Kevin Cleary, "CT fluoroscopy-guided robotically assisted lung biopsy," presented at the *SPIE Medical Imaging Symposium* and to be published in the *Visualization, Image-Guided Procedures, and Display* track, San Diego, CA, 11-16 February 2006.

[Yaniv 2006a]   Ziv Yaniv, Roland Stenzel, Kevin Cleary, and Filip Banovac, "A realistic simulation framework for assessing deformable slice-to-volume (CT-fluoroscopy/CT) registration," presented at the *SPIE Medical Imaging Symposium* and to be published in the *Visualization, Image-Guided Procedures, and Display* track, San Diego, CA, 11-16 February 2006.

[Yaniv 2006b]   Ziv Yaniv and Kevin Cleary, "Fluoroscopy based accuracy assessment of electromagnetic tracking," presented at the *SPIE Medical Imaging Symposium* and to be published in the *Visualization, Image-Guided Procedures, and Display* track, San Diego, CA, 11-16 February 2006.

8   Appendices (Papers)

Copies of the eight papers published during this report period are reproduced in this section.

8.1 Carignan 2005: Design of an Exoskeleton …

Reprint begins on the next page and is eight pages.

Design of an Arm Exoskeleton with Scapula Motion for Shoulder Rehabilitation

Craig Carignan

Imaging Science and Information Systems (ISIS) Center
Department of Radiology
Georgetown University
Washington, DC 20057
Email: crc32@georgetown.edu

Michael Liszka
Stephen Roderick

Space Systems Laboratory (SSL)
Department of Aerospace Engineering
University of Maryland
College Park, MD 20742
Email: liszka@ssl.umd.edu, roderick@ssl.umd.edu

Abstract— **The evolution of an arm exoskeleton design for treating shoulder pathology is examined. Tradeoffs between various kinematics configurations are explored, and a device with five active degrees of freedom is proposed. Two rapid-prototype designs were built and fitted to several subjects to verify the kinematic design and determine passive link adjustments. Control modes are developed for exercise therapy and functional rehabilitation, and a distributed software architecture that incorporates computer safety monitoring is described. Although intended primarily for therapy, the exoskeleton will also be used to monitor progress in strength, range of motion, and functional task performance.**

I. Introduction

The development of robotic exoskeletons for physical therapy is relatively recent in the field of robotics. Powered orthotic devices have been in use for over a decade, but the focus of these mechanisms has been assistive rather than rehabilitative. The primary role of exoskeletons thus far has been as a haptic device for virtual reality (VR) applications. Prime examples of these devices include the portable, back-mounted *EXOS Force ArmMaster* and the floor-mounted *FREFLEX Exoskeleton* [4].

When designing portable exoskeletons, the classic tradeoff between power and weight always emerges. VR exoskeletons are almost always motor-driven in order to attain the high control bandwidths required for simulating contact with virtual environments. Unfortunately, motors have very low power-to-weight ratios, which tend to limit the force output of the exoskeleton for physical therapy application. Pneumatic-actuators, on the other hand, have high power-to-weight ratios but poor actuator response, rendering them too bandwidth-limited for functional rehabilitation.

This work builds upon advances in actuator/drive technology to develop a lightweight but powerful exoskeleton that can be used for exercise therapy and functional rehabilitation. The article begins with a brief survey of previous arm exoskeletons in Section II. The kinematic and mechanical designs are discussed in Section III. The exoskeleton control system and operational modes are discussed in Section IV. The software architecture and safety system are addressed in Section V. Some conclusions are observed in Section VI, and the status of the exoskeleton development is reviewed.

II. Previous Work

In order to closely follow the motion of the human arm, exoskeletons are typically designed with the seven principal degrees of freedom (DOF) of the human arm: shoulder (3), elbow (1), and wrist (3). The sequence of rotations shown in Figure 1 reflects the convention commonly used in the biomechanics community [18]. The glenohumeral (GH) joint is modeled as a 3-DOF ball and socket joint defined by a set of rotating coordinates. The first joint, shoulder flexion/extension, is defined as the rotation of the shoulder about an axis through the GH joint and perpendicular to the longitudinal body axis. The second axis, shoulder abduction/adduction, is the rotation of the upper arm toward/away from the body about an axis that is perpendicular to the flexion axis and the longitudinal axis through the upper arm. The third axis, shoulder medial/lateral (internal/external) rotation, is the roll about the longitudinal axis of the upper arm. Note that this GH model is purely rotational; it does not include translation of the glenohumeral joint caused by scapulothoracic motion, clavicle rotation, and other joints in the shoulder [13].
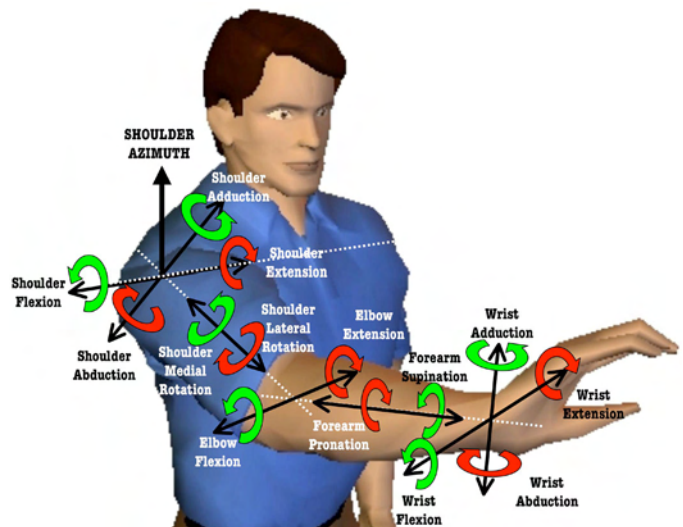

Fig. 1.   The seven principal degrees of freedom of the human arm (adapted from [18]).

Alternatively, several bioengineering researchers have favored the "azimuth-elevation-roll" convention commonly used in scientific practice [23]. In this standard, the first shoulder rotation, "azimuth," is the rotation about a vertical axis through the shoulder. The second rotation, "elevation," is rotation of the upper arm about an axis orthogonal to both the azimuth axis and the longitudinal axis of the upper arm. The third shoulder axis, "roll," is the rotation of the upper arm about its longitudinal axis and is the same as the "shoulder" rotation in the biomechanics convention.

Several of the arm exoskeleton prototypes that have been built to-date are listed in Table I. The table lists the number of joints, power source, mass, upper/forearm lengths, and the shoulder type. If the exoskeleton is portable, then the mass of the backpack and exoskeleton are each given. The two lengths reported are for the upper arm and forearm links. Four different shoulder types appear based upon the sequence of rotations in the shoulder. The range of motion and continuous static torques for several of these devices are listed in Table II and Table III.

The majority of exoskeletons listed in Table I were developed as haptic devices for virtual reality (VR) applications. Haptic devices are typically driven by motors to provide the high control bandwidth required for interaction with virtual environments and thus have relatively low power output as seen in Table III. The only exoskeleton that even comes close to human output capability is the hydraulically-powered *Sarcos Dextrous Arm Master* developed as a force-reflecting master arm for teleoperation applications [11]. While this may be the most powerful exoskeleton, it is also the heaviest.

TABLE I

ARM EXOSKELETON PROTOTYPES.

DEVICE	DOF #	Port? Y/N	Power *	Mass† (kg)	Length‡ (cm)	Type △
EXOS [4]	5	Y	E	8.2/1.8	?/?	FAR
Dex [11]	7	N	H	20.9	31.1/25.9	FAR
Sensor [21]	7	N	E	6	24.0/28.5	FAR
GIA [2], [16]	5	N	E	10	30.5/25.0	AFR
ATHD [8]	7	Y	E	?/2.3	?/?	BSR
MB [22]	7	Y	∅	?/15	28.3/26.5	ZLR
FreFlex [10]	7	N	E	?	37.2/29.9	AFR
pMA [25]	7	N	P	2	?/?	FAR
Salford [5]	9	Y	∅	?/0.75	?/?	AFR
MULOS [12]	5	N	E	2	?/?	ZLR
UWash [24]	7	N	E	?	?/?	AFR

* E-electric, H-hydraulic, P-pneumatic, ∅-unactuated
† Backpack/Arm (from first GH joint)
‡ Upper Arm (GH to Elbow)/Forearm (Elbow to Wrist)
△ FAR (flexion-abduction-rotation), AFR (abduction-flexion-rotation), ZLR (azimuth-elevation-roll), BSR (ball&socket-rotation)

A number of unactuated devices have also been built for gathering anthropomorphic data such as the *MB Exoskeleton* developed for the U.S. Air Force and shown in Figure 2 [22]. Although this device is passive, it incorporated a number of features important for physiotherapy applications such as good range of motion, adjustable link lengths (±2.5 cm upper

arm, ±2.0 cm forearm), and portability. The project was discontinued before a powered exoskeleton was built, but first-hand observation provided a lot of valuable information.

Fig. 2. SSL personnel dons the MB Exoskeleton during visit to Wright-Patterson Air Force Base. (SSL Photo Archives – used with permission of the Wright-Patterson Air Force Research Laboratory)

The tradeoff between power-to-weight ratio and control bandwidth for haptic devices has been addressed by several researchers [4]. Recent articles suggest a trend toward using pneumatically powered exoskeletons for physical therapy. Examples of these include the *pMA Exoskeleton* which utilizes pneumatic muscle actuators (pMA) [25] and the *Skil Mate* wearable elbow/forearm exoskeleton powered by McKibben artificial muscles [26] and developed for astronaut extravehicular activity (EVA). While these devices have excellent power-to-weight ratios, they have relatively low bandwidth capability ($\approx 0.5 Hz$), making them poorly suited at present for virtual reality applications. However, they do show excellent promise as assistive and resistive training devices.

The Motorized Upper Limb Orthotic System (*MULOS*) is a wheelchair-mounted exoskeleton developed for use by persons with weak upper limbs [12]; thus, it is not intended as an exercise system for fit adults. In addition, there is no compensation for scapulo-thoracic motion, which is considered key for shoulder rehabilitation. Nonetheless, *MULOS* provided some valuable guidelines for designing the shoulder kinematics as well as instituting a number of novel safety features, such as a slip clutch for protection against spastic motions.

The only exoskeleton that has explicitly allowed for scapulothoracic motion is the non-driven *Salford ArmMaster* developed for tactile VR applications [5], [6]. This exoskeleton incorporates scapula tilt of up to $60°$ and scapula medial rotation of up to $45°$ that could generate up to 12 cm of scapula elevation/depression. *MULOS* researchers examined the translation of the GH joint for several assistive tasks and

deemed that the motion was not critical in their application [3]. The Japanese-designed *ATHD* has used flex cables to drive the shoulder rotational degrees of freedom from motors mounted in a backpack, an approach that could allow for motion of the GH-joint, but only at the expense of shoulder rotation.

TABLE II
EXOSKELETON JOINT RANGES OF MOTION (DEG).

JOINT	Man [18][†]	Exos [4]	Dex [4]	Fre [10]	GIA [2]	Sen [20]	HD [8]	MB [22]
shoulder flex/ext	188 /61	120	180	130 /52	55 /36	150 /30	180 /50	130
shoulder abd/add	134 /48	120	180	28 /18	73 /73	50 /0	180 /0	135
shoulder med/lat	97 /34	100	180	90 /90	77 /81	60 /60	90 /90	260
elbow flex/ext	142 /0	100	105	166 /-3	89 /15	90 /0	115 /0	135
forearm pro/sup	85 /90	100	105	90 /90	99 /88	90 /90	90 /90	215
wrist flex/ext	90 /99	—	180	38 /39	50 /20	60 /60	70 /90	90
wrist abd/add	47 /27	—	100	57 /52	80 /80	15 /15	55 /25	30

[†]Mean values for dominant arm of 39 males

TABLE III
EXOSKELETON MAXIMUM JOINT TORQUES (N-M).

JOINT	Human [9][†] [1][‡]	Exos [4]	Dex [4]	Fre [10]	GIA [16]	pMA [25]
shoulder flex/ext	115 /110	6.4	97	34	20	30
shoulder abd/add	134 /94	6.4	97	34	20	27
shoulder med/lat	—	2.3	50	17	10	6
elbow flex/ext	72.5 /42.1	1.6	50	17	10	6
forearm sup/pro	9.1 /7.3	0.4	50	5.6	2	5
wrist flex/ext	19.8 /10.2	—	5.5	2.8	—	4
wrist abd/add	20.8 /17.8	—	5.5	2.8	—	4

[†]Mean values for male shoulder, dominant arm
[‡]Mean values for male elbow/wrist, dominant arm

III. MECHANICAL DESIGN

A driving goal for the Maryland-Georgetown-Army (MGA) Exoskeleton was to use the lowest number of DOFs possible to allow for full exercise therapy of the shoulder complex. Considering the design from a biomechanical perspective, it was determined that five powered degrees of freedom would be required. Based on first hand experience of several physical therapists, allowing for incidental or deliberate motion of the scapulothoracic joint would be critical to achieving our goals so a scapula joint was included in the design. Three joints would be required for glenohumural shoulder rotation. An elbow joint was needed since several flexion/extension muscles (triceps and biceps brachii) are articulated through the shoulder

[13]. The inclusion of the elbow implied the addition of a forearm linkage, so the forearm roll was added as a passive joint. The following sections will review the development of the kinematics, construction of the rapid-prototypes, and selection of the hardware.

A. Kinematics

Two major issues arose in the design of the exoskeleton: how to articulate translation of the shoulder joint and where to place the shoulder singularity. It was clear that designing a device to fully articulate 11 or more DOFs of the shoulder complex would not be reasonable [19], so our goal was to use a single rotary joint as a first order approximation of shoulder translation. In addition, the singularity or "gimbal lock" that results from using three single-axis shoulder joints had to be addressed. The intent was to place the singularity at an azimuth and elevation that would be least likely to interfere with rehabilitation tasks.

Since our goal was to capture as much of the scapulothoracic motion as possible using a single rotary joint, we decided to focus on the largest motion, which is shoulder elevation and depression. Shoulder elevation can occur either deliberately, e.g. shoulder shrug, or incidentally during rotation of the glenohumeral (GH) joint. An example of the latter occurs during shoulder abduction starting from the arm hanging straight down by the side of the leg and moving in a circular arc above the head like in a jumping jack motion.

Figure 3 shows the translation of the GH joint in the frontal plane and was generated by using video capture data from a shoulder abduction movement [19]. The vertical displacement (elevation) of the shoulder was found to be far greater than the horizontal (protraction) displacement, with a sharp point in the curve where the adduction angle reaches $90°$ (arm is horizontal). This point corresponds to the onset of rotation of the clavicle, which then thrusts the acromio-clavicular (AC) joint and consequently the GH joint as the shoulder continues to elevate.
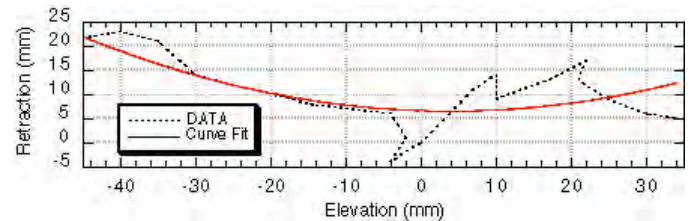
Fig. 3. Displacement of shoulder in frontal plane during a $180°$ shoulder abduction using data taken from [19] (curve fit is 2nd order polynomial).

If a circular curve could be fit to data similar to Figure 3, an axis of rotation could be identified for placement of a scapulothoracic joint. Since the axis of this joint is perpendicular to the frontal plane, it could be mounted anywhere along a line normal to the back. Therefore, the motor can be conveniently mounted on a backpack strapped to the subject's torso and can yield the desired elevation and depression of the shoulder joint.

Shoulder singularities were the second major issue to be confronted. The GH joint is usually modeled kinematically as a ball and socket joint. However, attempting to implement the same type of joint in the exoskeleton would pose severe design challenges as well as introduce interference between the human joint and robotic joint. Instead, the ball and socket joint is replaced by three serially connected pin joints. Although the pin joints create three DOFs around a single point, they do not exactly replicate the kinematics of a ball and socket joint. Most importantly, the series of pin joints create two singularities, $180°$ apart from one another. These singularities can be moved, but cannot be eliminated.

Design of the elbow joint is considerably more straightforward because it can be approximated as a single pin joint. The actuator corresponding to this joint will incorporate a torque-limiting slip clutch, which decouples the actuator from the frame of the robotic arm if a predetermined torque value is exceeded. This device will help protect the user from injury by allowing free movement in the elbow if a spasm occurs in that joint.

The forearm roll will be the terminal joint on this prototype. It will be equipped with an encoder to measure the joint angle, but will not be driven. A mounting bracket for a hand grip will be rigidly attached to the forearm link through a six-axis force/torque sensor. Thus the wrist abduction and flexion joints will be fixed in the first hardware prototype.

B. Rapid-Prototyped Models

Two rapid-prototyped (RPT) models of the MGA Exoskeleton were built. The first prototype was used mainly to evaluate the kinematics and to decide what passive link adjustments would be required. The second prototype reflected kinematics changes following a design review and closely matched the final design. The prototypes were attached to the back of a neopreme *Uni-Vest* ^{TM} weight vest for portability, and a set of passive adjustments between the scapula and shoulder joints allowed for a customized fit.

1) Prototype I: A 3D model of the first prototype is shown in Figure 4. An adjustable linkage connects the scapulo-thoracic joint to the first shoulder pin joint which is oriented horizontally as seen in Figure 5. This segment has two angular adjustments accounting for curvature in the back, and a prismatic adjustment accounting for varying distance between the scalupo-thoracic joint and the GH joint.

The second joint axis was mounted orthogonally to the first, and the third joint axis was mounted orthogonally to the second. When the three GH joint axes become coplanar, the shoulder becomes singular. For an orthogonal triad, this singularity occurs when the first and third joint axes align producing a singularity along the direction of the first joint axis. The direction of this singularity can be changed using the second angular adjustment in the first linkage. Since this passive adjustment is oriented vertically, the singularity remains in the transverse plane.

The third GH joint axis is the shoulder internal/external rotation. A "C"-shaped linkage fits over the upper arm as

shown previously in Figure 5. A strap secures a rotational joint on this linkage to the arm so that the joint moves with the arm. Modifications to the design of the first prototype began before the elbow linkage was constructed.
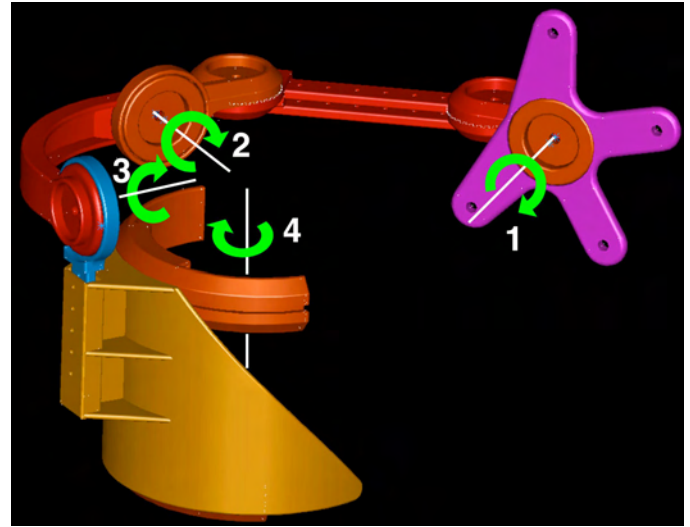
Fig. 4.   CAD schematic of Prototype I.

Fig. 5.   Side view of Prototype I with elbow and shoulder at $90°$ flexion.

2) Prototype II: A schematic of the second prototype is shown in Figure 6. Significant kinematic changes were implemented from the first prototype to move the singularity out of the transverse plane into a less intrusive location. As in the first prototype, an adjustable linkage connects the scapulothoracic joint to the first GH joint axis as seen in Figure 7. However, an additional passive rotation axis in the transverse plane is used to rotate the first shoulder axis (and thus singularity) about $30°$ from a normal to the plane containing the scapula axis and the GH joint.

Keeping the first axis away from the normal allows the

arm to rest straight down against the side without being in a singular configuration. This alignment of the shoulder singularity with the azimuth axis in the *MB Exoskeleton* was very problematic during our examination (see Figure 2). Realignment of the azimuth axis was also employed in the *MULOS* design, although the tilt was 30° from vertical in the sagittal rather than frontal plane.

The second GH joint axis is oriented 90° from the first and is located to the side and slightly beneath the shoulder, as shown in Figure 7. The third GH joint is perpendicular to the second, but makes a 135°-angle with the first when the arm is in the rest position. The reason for making this angle 135° and not 90° is to allow the arm to abduct further before the first and third GH joints interfere with each other. Although the elbow linkage was not built for the prototype, the attachment to the upper arm can be seen at the base of Figure 7.

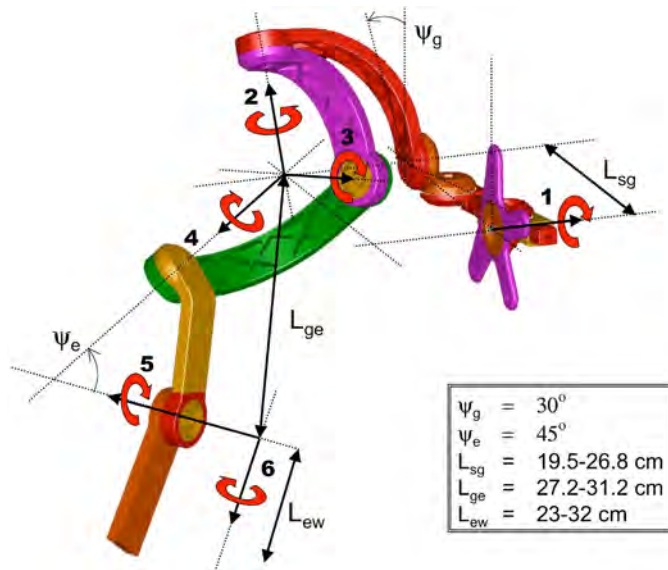Fig. 7. Prototype II is shown at 90° shoulder flexion while mounted to a weight vest.

Fig. 6. CAD schematic of Prototype II.

Each joint (except for the forearm) is driven by a Kollmorgen brushless DC motor and harmonic drive transmission from HD Systems. Harmonic drives were chosen because of their compactness, low backlash, and backdrivability. The elbow is equipped with a slip clutch manufactured by Mayr Power Transmission and has an adjustable torque range of $20-50$ N-m. It also features a synchronous mechanism, which restricts the device from recoupling in all but one position, thus preserving the orientation between the input and the output.

C. Hardware

The objective of the mechanical design was to achieve at least half human strength and 90% of the human range of motion in each joint given previously in Tables II and III. The realized stall torque and range of motion for the active joints are given in Table IV and meet these specifications. A drawing of the final exoskeleton design is shown in Figure 8.

TABLE IV

JOINT CHARACTERISTICS FOR MGA EXOSKELETON.

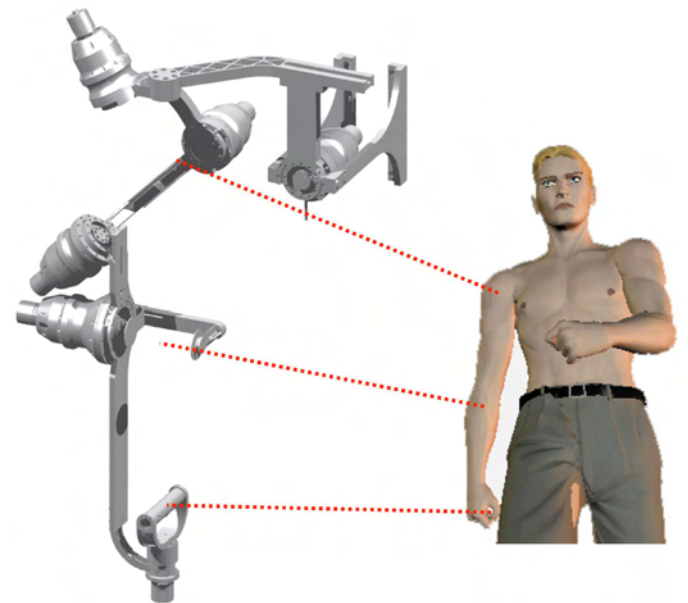| Joint	Gear Ratio	Stall Torque (N-m)	Range (deg)
Scapula	160 : 1	92	$+30/-30$
GHR 1	160 : 1	92	$+180/-45$
GHR 2	160 : 1	92	$+90/-65$
GHR 3	160 : 1	92	$+210/-30$
Elbow	160 : 1	64	$+142/0$

Fig. 8. IDEAS-CAD rendering of final exoskeleton design.

Power and communication is routed through an umbilical using a Galil 6-Axis Motion Control card mounted in the PC and Advanced Motion Control PWM power modules. Motor

position is determined using an 1800-line optical incremental encoder manufactured by Numerik Jena. Single-turn, 12-bit optical absolute encoders manufactured by Gurley Precision Instruments are mounted at the output of the transmission to determine absolution position on start up and to monitor the incremental encoders.

A Model 50M31A force/torque sensor manufactured by JR3, Inc. is used to measure forces and torques on the handle. The sensor has a rating of 25 lb (111 N) in the radial direction and 50 lb (222 N) along the axial direction. The unit is a very compact 50 mm × 31 mm and has a mass of 0.15 kg. The sensor has integrated sensor electronics, and the six-channel digital output is read by a PCI card at 8 KHz. A single-axis torque sensor manufactured by Omega Engineering, Inc. is attached to the output side of the scapula transmission. The sensor is capable of measuring torque levels up to 113 N-m. Two single-axis compression load cells made by Sensotec, Inc. are attached to mounting plates on either side of the elbow to measure axial load at the elbow. Each sensor is capable of measuring forces up to 25 lb (111 N).

IV. Control System

The exoskeleton operates in two modes: Virtual Reality (VR) Mode and Physical Therapy (PT) Mode. In VR Mode, the forces exerted at the hand are controlled by interaction with a virtual environment generated by a computer. In PT Mode, the arm is allowed to rotate about an arbitrary axis through the shoulder using a preset resistance profile. In either mode, the scapula joint moves independently to "accommodate" the patient using sensed torque from the local torque cell. The control of the arm joints and scapula joint are described in more detail below.

A. Virtual Reality Mode

In Virtual Reality (VR) Mode, computer-generated environments are used to simulate daily living tasks for functionally-based rehabilitation. The patient views the simulated task and representation of their arm through a head mounted display while the exoskeleton provides haptic feedback to the patient. A force sensor located at the hand gripper senses the forces being exerted by the patient's "contact" with the virtual environment and relays them to the controller which moves the exoskeleton in response to the interaction.

Because the exoskeleton is kinematically redundant, specification of the wrist position is not enough to specify the three shoulder rotations and elbow pitch. This self-motion manifests itself as the ability of the elbow to "orbit" about the shoulder-wrist axis p_w shown in Figure 9 while the position of the wrist and shoulder are held fixed [14]. The angle formed by the shoulder-elbow-wrist (SEW) plane with a reference vector v is referred to as the "SEW angle."

The admittance controller shown in Figure 10 is used to convert the sensed contact forces at the hand and elbow into desired movements of the exoskeleton [7], [15]. Signals from the force-torque sensor at the hand are relayed to an admittance model of the virtual environment, which then outputs a desired
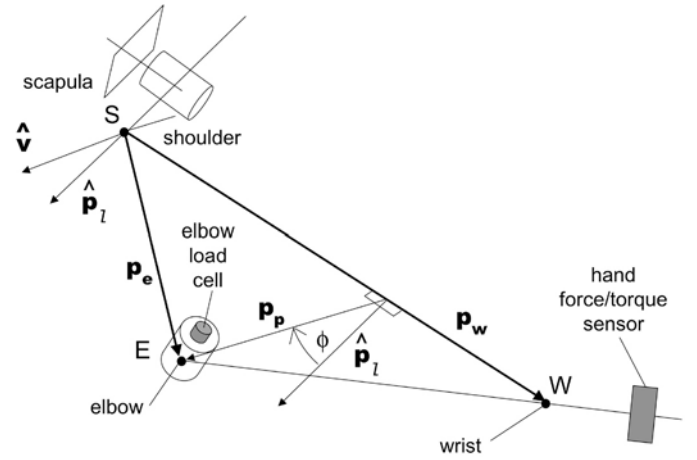

Fig. 9. Definition of shoulder-elbow-wrist (SEW) roll angle and location of gripper force/torque sensor and elbow axial load cells.

velocity for the wrist, $\dot{p}_w$. In addition, a pair of compression load cells mounted along the elbow axis are used to determine the torque, τ_ϕ, exerted about the shoulder-wrist axis, p_w. The SEW torque is then integrated to produce a desired SEW roll velocity $\dot{\phi}_d$ that is proportional to the torque about the p_w axis. The desired wrist and SEW velocities are then converted to desired angular velocities at the joints using the inverse Jacobian, $J_{w\phi}$, and the resultant desired joint angles, $\dot{\theta}_d$, are then tracked using a proportional-derivative (PD) control law.
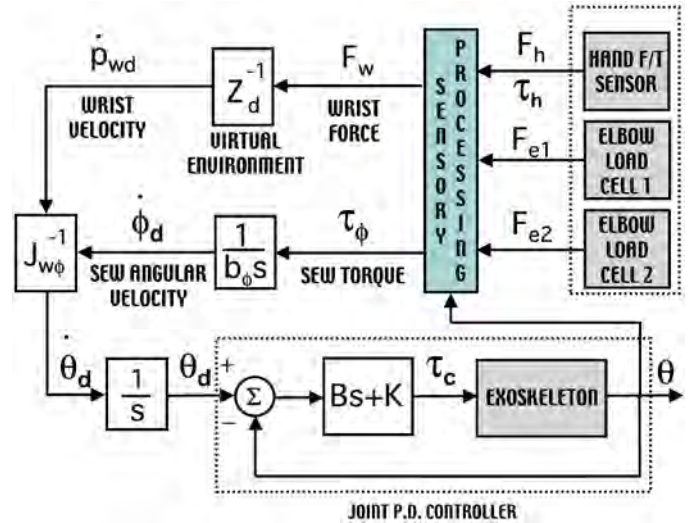
Fig. 10. Admittance controller used in VR Mode.

B. Physical Therapy Mode

In Physical Therapy (PT) Mode, the exoskeleton becomes a programmable resistance trainer that allows the patient to exercise about an arbitrary shoulder rotation axis. For rotator cuff injuries, for example, therapists often prescribe exercises involving lateral/medial rotation of the shoulder. Since there is no single joint corresponding to shoulder rotation, the exercise involves all three shoulder axes of the exoskeleton. Thus, the

controller needs to yield a prescribed resistance profile about the desired axis while preventing rotations about the other shoulder axes.

Since the torques about the shoulder axes cannot be measured directly, an impedance controller is used to realize the desired resistance profile [17]. The shoulder joint velocities are relayed to a Jacobian, J_{GH}, as shown in Figure 11, which then computes the Cartesian velocities about the glenohumeral (GH) joint, ω_{GHd}. These velocities are then multiplied by the desired resistance profile, which outputs the desired torques about the GH axes, τ_{GHd}. These torques are then converted into exoskeleton joint torques using the Jacobian. A feedforward model of the exoskeleton runs in parallel to calculate gravity and other feedforward compensation torques. Since only the GH angles are specified, the elbow pitch is left unconstrained and can be moved however the patient desires.
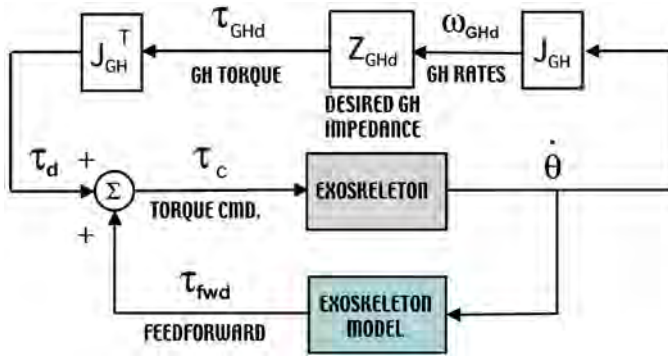

Fig. 11.   Impedance Controller used in PT Mode.

C. Scapula Joint Control

The scapula joint is controlled independently from the arm joints using the admittance controller shown in Figure 12. A torque cell at the output of the transmission directly measures the torque being exerted by the scapula joint, τ_ξ. However, because the applied torque must balance the sum of the gravitational torque and the torque applied by the subject, a gravitational model is used to subtract out the component due to the gravity load. The estimated human torque is then integrated to produce a desired scapula joint velocity, $\dot{\xi}_d$, which is then tracked by a PD controller.
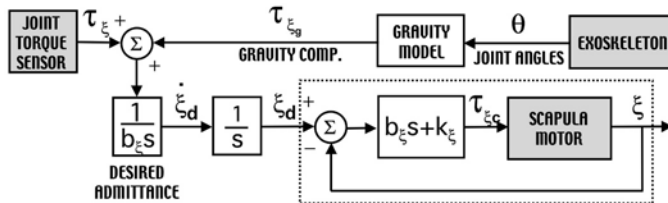

Fig. 12.   Accommodation controller used for scapula joint.

V. SOFTWARE ARCHITECTURE

The architecture of the control system is shown in Figure 13. The health worker interacts with the system through the control station and its user interface. This interface allows the clinician to monitor the robotic system performance, enter patient rehabilitation parameters, and store patient history. The control station communicates over the Internet with the robot control computer, which is responsible for control of the robotic arm and overall patient safety. The arm controllers running on the robot control computer produce either a position or torque command, which is sent to the motor controller. A force-torque sensor attached to the gripper senses the forces and torques exerted by the patient, which are relayed to the robot control computer via a digital acquisition board.

The robot control computer runs the TimeSys Linux real-time operating system, in order to guarantee meeting its safety deadlines. As the operator computer is not involved in safety decisions, it will run a standard desktop operating system (in which the ability to respond to events within a certain time frame is not guaranteed). The arm controller algorithms operate in Cartesian space, utilize force/torque sensor data, and operate at 200 Hz. The PD controller, when required by a particular arm controller, runs at 1000 Hz.
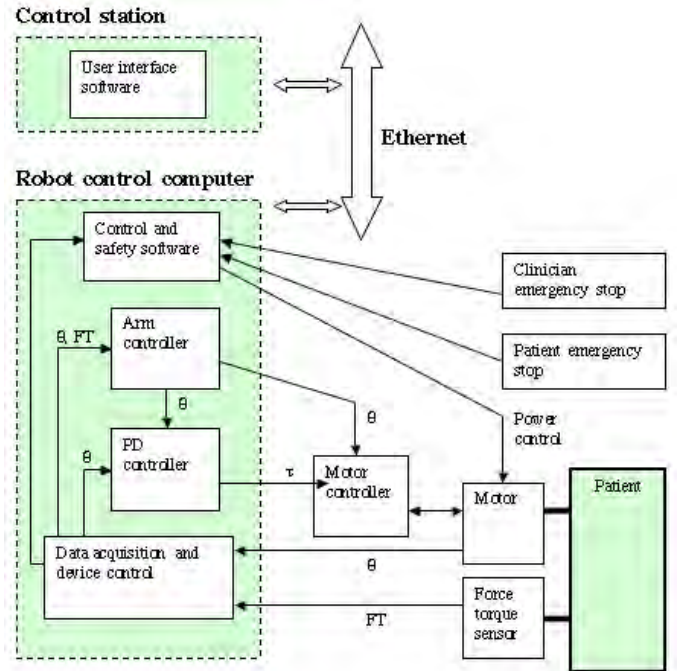
Fig. 13.   Software control architecture.

All safety decisions are carried out within the robot control computer and occur autonomously. This setup allows for very high speed reaction by the computer safety system in the event of a component failure, communication error, or the patient attempting something they should not. The embedded robot system is designed to be a 'fail-safe' system, and is, as much as practical, safe in and of itself. The actual 'safe state' entered will be one of: a) the arm holding its current position and not exerting any force on the patient, or b) a complete power-down of the arm. At any time, either the clinician or the patient are able to manually safe the system by hitting a button or key.

The robot control computer is responsible for enforcing patient-related force, position, and range-of-motion limits; guaranteeing that the heartbeat transmitted by every computer is valid; verifying that all the local electronics are functioning and correctly providing data; and ensuring that the operator computer is functioning. These checks occur at either 200 or 1000 Hz, depending on whether they are associated with the arm or PD controller. Also, the robot control computer is protected by watchdog timers that will safe the system in the event of incorrect operation.

The reaction time of the software safety system determines how much affect a failure can have on the patient, in terms of how much additional force can be applied or how far the arm can move, before the system safes. This effect depends on the reaction time of the robot control computer and the rate of the particular safety check. As software checks are executed at either 200 or 1000 Hz, the reaction time will be a maximum of 5 ms, and a minimum of 1 ms.

VI. CONCLUSION

This paper began with a survey of exoskeletons built to-date and has explored the design tradeoffs between various kinematic designs and actuator technologies. Only one exoskeleton was found that incorporated scapulothoracic motion, but it was not powered. A single rotary joint perpendicular to the back was chosen to accommodate shoulder elevation and depression. The glenohumeral joint is based on an orthogonal axis triad with the first axis tilted at 30° away from the azimuth axis to accommodate the singularity. Two rapid-prototyped versions of the exoskeleton were built prior to final design. Mechanical fabrication is complete, and the exoskeleton is now undergoing electronics integration and testing. Although the prototype mass is only about 12 kg, it will initially be wall-mounted due to the weight of the external components.

ACKNOWLEDGMENT

REFERENCES

[1] K. N. An, L. J. Askew, and E. Y. Chao, "Biomechanics and functional assessment of upper extremeties," in *Trends in Ergonomics/Human Factors III*, W. Karwowski, Ed. North-Holland: Elsevier Science Publishers B. V., 1986.

[2] M. Bergamasco, B. Allotta, L. Bosio, L. Ferretti, G. Parrini, G. Prisco, F. Salsedo, and G. Sartini, "An arm exoskeleton system for teleoperation and virtual environments applications," in *Proc. of the IEEE Intl. Conf. on Robotics and Automation*, San Diego, 1994, pp. 1449–1454.

[3] M. A. Buckley and R. R. Johnson, "Computer simulation of the dynamics of a human arm and orthosis linkage mechanism," in *Proc. Instn. Mech. Engrs. Part H*, vol. 211, 1997, pp. 349–357.

[4] G. C. Burdea, *Force And Touch Feedback For Virtual Reality*. New York: John Wiley and Sons, 1996.

[5] D. G. Caldwell, C. Favede, and N. Tsagarakis, "Dextrous exploration of a virtual world for improved prototyping," in *Proc. of the IEEE Intl. Conf. on Robotics and Automation*, leuven, belgium, may 1998, pp. 298–303.

[6] D. G. Caldwell, O. Kocak, and U. Andersen, "Multi-armed dexterous manipulator operation using glove/exoskeleton control and sensory feedback," in *Proc. of the IEEE/RSJ Intl. Conf. on Intelligent Robots and Systems*, pittsburg, USA, Aug. 1995, pp. 567–572.

[7] C. Carignan and D. Akin, "Achieving impedance objectives in robot teleoperation," in *Proc. of the IEEE Conference on Robotics and Automation*, 1997, pp. 3487–3492.

[8] W. Chou and T. Wang, "Haptic interaction with virtual environment using an arm type exoskeleton device," in *Proc. of the IEEE Intl. Conf. on Robotics and Automation*, new orleans, USA, apr 2004, pp. 1992–1997.

[9] H. P. V. Cott and e. Robert G. Kinkade, *Human Engineering Guide to Equipment Design, rev. ed.* New York: McGraw-Hill, 1963.

[10] R. L. W. II, M. A. Murphy, D. North, J. Berlin, and M. Krier, "Kinesthetic force/moment feedback via active exoskeleton," in *Proc. of the Image Society Conference*, scottsdale, arizona, 1998.

[11] S. C. Jacobsen, F. M. Smith, and D. K. Backman, "High performance, dextrous telerobotic manipulator with force reflection," in *Intervention/ROV'91 Conference and Exposition*. Hollywood, Florida: Marine Technology Society, May 1991, pp. 213–218.

[12] G. R. Johnson, D. A. Carus, G. Parrini, S. S. Marchese, and R. Valeggi, "The design of a five-degree-of-freedom powered orthosis for the upper limb," in *Proc. Instn. Mech. Engrs. Part H*, vol. 215, 2001, pp. 275–284.

[13] E. Kreighbaum and K. M. Barthels, *Biomechanics: a qualitative approach for studying human movement, 4th Ed*. Boston: Allyn and Bacon, 1996.

[14] K. Kreutz-Delgado, M. Long, and H. Seraji, "Kinematic analysis of 7 dof manipulators," *Int. Journal of Robotics Research*, vol. 11, no. 5, pp. 469–481, 1992.

[15] J. Maples and J. Becker, "Experiments in force control of robotic manipulators," in *Proc. of the IEEE Conference on Robotics and Automation*, Apr. 1986, pp. 695–702.

[16] S. Marcheschi, "Progettazione e realizzazione di un sistema di controllo per uninterfaccia aptica a 7 gradi di libert," Master's thesis, Università Degli Studi Di Pisa, apr 2001.

[17] T. Massie and J. K. Salisbury, "The PHANTOM haptic interface: A device for probing virtual objects," in *Proc. ASME Winter Annual Meeting: Symposium on Haptic Interfaces for Virtual Environment and Teleoperator Systems*, Nov. 1994.

[18] E. J. McCormick, Ed., *Human Factors Engineering, 3rd ed.* New York: McGraw-Hill, 1970.

[19] T. B. Moeslund, C. B. Madsen, and E. Granum, "Modelling the 3d pose of a human arm and the shoulder complex utilising only two parameters," in *Proc. of the Intl. Conference on Model-based Imaging, Rendering, Image Analysis and Graphical Special Effects*, INRIA Rocquencourt, France, 2003.

[20] A. Nakai, Y. Kunii, H. Hashimoto, and F. Harashima, "Arm type haptic human interface: Sensor arm," in *Intl. Conf. on Artificial Reality and Tele-Existence (ICAT)*, Tokyo, Japan, Dec. 1997, pp. 77–84.

[21] A. Nakai, T. Ohashi, and H. Hashimoto, "7 dof arm type haptic interface for teleoperation and virtual reality systems," in *Proc. of the IEEE/RSJ Intl. Conf. on Intelligent Robots and Systems*, Victoria, B.C., Canada, Oct. 1998, pp. 1266–1271.

[22] D. W. Repperger, S. J. Remis, and G. Merrill, "Performance measures of teleoperation using an exoskeleton device," in *Proc. of the IEEE Intl. Conf. on Robotics and Automation*, Cincinnati, May 1990, pp. 552–557.

[23] D. P. Romilly, C. Anglin, R. G. Gosine, C. Hershler, and S. U. Raschke, "A functional task analysis and motion simulation for the development of a powered upper-limb orthosis," *IEEE Transactions on Rehabilitation Engineering*, vol. 2, no. 3, pp. 119–129, Sept. 1994.

[24] J. Rosen, B. Hannaford, and S. Burns, "Neural control of an upper limb powered exoskeleton system – grant report," in *Proc. of the First NSF Robotics and Computer Vision (RCV) Workshop*, Los Vegas, Oct. 2003.

[25] N. Tsagarakis, D. G. Caldwell, and G. A. Medrano-Cerda, "A 7 dof pneumatic muscle actuator (pma) powered exoskeleton," in *Proc. of the IEEE Intl. Workshop on Robot and Human Interaction*, Pisa, Italy, sep 1999, pp. 327–333.

[26] Y. Umetani, Y. Yamad, T. Morizono, T. Yoshida, and S. Aoki, "Skil Mate, wearable exoskeleton robot," in *Proc. of the IEEE Intl. Conf. on Robotics and Automation*, 1999, pp. 984–988.

8.2 Cheng 2005: IGSTK Framework …

Reprint begins on the next page and is nine pages.

IGSTK: Framework and Example Application Using an Open Source Toolkit for Image-Guided Surgery Applications

Peng Cheng[a]*, Hui Zhang[a], Hee-su Kim[b], Kevin Gary[c], M. Brian Blake[d], David Gobbi[e], Stephen Aylward[f], Julien Jomier[f], Andinet Enquobahrie[f], Rick Avila[f], Luis Ibanez[f], Kevin Cleary[a]

[a]Imaging Science and Information Systems (ISIS) Center, Dept. of Radiology, Georgetown University, Washington, DC, USA

[b]Department of Computer Science, Kyungpook National University, Korea

[c]Division of Computing Studies, Arizona State University, Mesa, Arizona, 85212, USA

[d]Department of Computer Science, Georgetown University, Washington, DC, 20007, USA

[e]Atamai Inc., London, Ontario, N6B 2R4, Canada

[f]Kitware Inc., Clifton Park, NY, 12065, USA

ABSTRACT

Open source software has tremendous potential for improving the productivity of research labs and enabling the development of new medical applications. The Image-Guided Surgery Toolkit (IGSTK) is an open source software toolkit based on ITK, VTK, and FLTK, and uses the cross-platform tools CMAKE and DART to support common operating systems such as Linux, Windows, and MacOS. IGSTK integrates the basic components needed in surgical guidance applications and provides a common platform for fast prototyping and development of robust image-guided applications. This paper gives an overview of the IGSTK framework and current status of development followed by an example needle biopsy application to demonstrate how to develop an image-guided application using this toolkit.

Keywords: open source, image-guided surgery, surgical guidance, tracking, state machine, needle biopsy, application prototyping

1. PURPOSE

The field of image-guided surgery is rapidly expanding, as new techniques are being developed that minimize treatment invasiveness and thereby reduce trauma and speed recovery for patients. A typical image-guided system consists of tracking subsystems for capturing the movement of instruments and the patient, and a computer subsystem for integrating and displaying pre- and intra-operative images and instrument positions using the tracking data. Most of the development effort is focused on implementing a general software infrastructure that supports the basic capabilities and inter-operation of these components. As new trackers and data integration algorithms are developed, maintaining a general infrastructure that nevertheless allows new features to be exploited is even more challenging, as most software platforms are not designed to be extendable from the outset. Testing such systems can also be an extensive process, and the lack of proper testing expose risks to patients and surgeons. The purpose of IGSTK is to enable the creation and validation of reusable, robust image-guided software as open-source, free of commercial licensing restrictions. This component-based software toolkit should make it easy for researchers to prototype and develop image-guided surgery applications.

2. METHODS

IGSTK has been under development for over a year and a public beta release will be available by the time of this conference (February 2006). IGSTK is based on the following existing open source software toolkits: ITK for segmentation and registration [1], VTK for visualization [2], CMake for cross-platform building and DART for cross-

---

* peng@isis.georgetown.edu; Telephone 1-202-687-2902; Fax 1-202-784-3479

platform testing, and FLTK for the user interface [3] (though the user interface layer is designed to allow for future application development with other UI toolkits). The IGSTK toolkit contains the basic software components needed to construct an image-guided system, including support for trackers, data integration algorithms, and a four-quadrant view incorporating image overlay.

1. Given that IGSTK is intended for developing applications that will be used to treat patients, robustness and quality are the highest priorities in the design of the toolkit. To minimize the risk of harm to the patient resulting from misuse of the classes, IGSTK is designed based on the following principles [4]:
2. Requirements are generated by studying and documenting scenarios of the surgical procedures in a clinical environment. By analyzing these scenarios, features that are necessary for fulfilling the requirements are extracted and implemented.
3. All IGSTK components are governed by a state machine. A state machine is contained within the class to control the access to the class. Components are always in a valid state to ensure they will perform in a predictable manner. The use of a state machine also helps enforce high quality standards for code coverage and run-time validation.
4. IGSTK does not directly expose ITK and VTK objects APIs to the application developer. Instead, the ITK and VTK objects are tightly encapsulated by IGSTK objects that provide a minimal but sufficient API for application development. This ensures that any APIs used by developers have been specifically tested for image guidance applications.
5. IGSTK does not utilize dynamic object typing. When IGSTK objects are created they must be declared with full specialization, and all type checking is performed at compile time and never at run time. This reduces the number of software parameters that can be adjusted at run-time, and hence reduces the possibility that the software will be running in an untested configuration.
6. IGSTK uses events to communicated between components, where the events are produced by the state machine of one object and received as inputs to the state machine of one (or more) other objects. The mapping of events to state machine inputs is explicitly defined and deterministic.
7. IGSTK does not use a return value or exception at the application level. Instead it uses events to pass information around.

2.1 State machine

To ensure safety and robustness, the state machine design pattern is incorporated into the IGSTK components. A state machine is defined by a set of states, a set of inputs, and a set of directed transitions between states. Transitions are changes from one state to another when a certain stimulus or input is received. An action may be taken along with a transition, to perform some task on entry to a state, or on exit from a state. State machines support the component-based architecture through encapsulation and extensibility. They ensure that a component is always in a valid state which can guarantee repeatable and deterministic behavior. A description of the state machine theory can be found in [6].

The following points summarize the advantage of using state machine in the toolkit [7]:
1. *Safety and Reliability*: A state machine ensures that component behavior is deterministic and that all components are in a known and error-free state at any given moment.
2. *Cleaner design*: Since developers must anticipate all possible inputs, states, and transitions, the state machine encourages and enforces a cleaner and more robust design, free of untested assumptions.
3. *API simplicity:* A focused, clearly expressed application programming interface (API) is a must for supporting robustness and reliability. In the context of surgical guidance, we believe that *flexibility* and *abundance of features* are undesirable, because they create more opportunities for things to go wrong during a surgical intervention.
4. *A consistent integration pattern*: The toolkit's value as it matures will undoubtedly be tied to the incorporation of additional functionality at the component level. This functionality will often take the form of reusable code from existing toolkits. State machines provide a consistent pattern for integrating this functionality while adhering to the safety-first principles necessitated by the application domain.
5. *Quality Control*: State machines facilitate code coverage in the sense of lines of code tested, as well as path coverage on a per component basis. Using code that is not based on state machines may result in applications that exhibit unreliable behavior. At run time, they can easily enter into any number of untold states that were

never explored by the developer, and can lead to error conditions that may or may not become visible to the users of the application.

The safety emphasis in IGSTK encourages explicit knowledge of component state and determines whether a given behavior may be executed while in that state. Hence, our application is a combination of traditional concepts in reliability (being in a known state) and the State Pattern [8] (for managing availability of behavior dynamically).

2.2 Architecture and components

Figure 1 presents a UML collaboration diagram of the major IGSTK components involved in a typical image-guided surgery application. The key components are from left to right [4, 5]:

1. View classes are used for presenting results and displays to the physician. An internal pulse generator is used to update the scene at specified refresh rate to keep the visual information up-to-date. Currently the IGSTK View classes are built with VTK classes and an FLTK window. They take FL events and translate them into VTK events to enable user interaction within the render window. View2D and View3D are subclasses of View with a different interaction style.

2. SpatialObject and SpatialObjectRepresentation. SpatialObjects classes model physical objects including image data and simple geometrical shapes such as anatomical structures and surgical devices, while SpatialObjectRepresentations classes are responsible for displaying their associated SpatialObject in the scene. IGSTK Spatial Objects can be attached to a Tracker Tool object, so that it can update its position as the Tracker Tool moves. The state machine in SpatialObjects classes enforces this association to be a one time operation. Once a Spatial Object is attached to a tracker tool it is not expected to get back to manual control nor to be re-attached to a second tracker tool. It is no longer possible to change the position of the object programmatically. IGSTK has a variety of SpatialObjects and corresponding SpatialObjectsRepresentations, including basic shapes (Cone, Cylinder, Ellipsoid and so on), ImageSpatialObject, UltrasoundProbeObject, and GroupObject to make composite SpatialObjects.

3. Tracker classes are an abstraction of tracking devices. They communicate with hardware and store data including position, orientation, and other relevant information pertaining to tracked surgical tools. The IGTSK Tracker component is developed based on code donated by Atamai Inc. and wrapped with a state machine. The internals of the Tracker require a separate thread to communicate with tracking hardware at an acceptable frequency. A pulse generator inside the class is used to automatically update the location information of the tracked device with an expiration time and propagate changes to SpatialObjects. IGSTK now supports NDI AURORA, POLARIS, and VICRA trackers (Northern Digital Inc., Waterloo, Canada) and Flock of Birds tracker (Ascension Technology Corporation, Burlington, VT USA), although not all features of these trackers are supported.
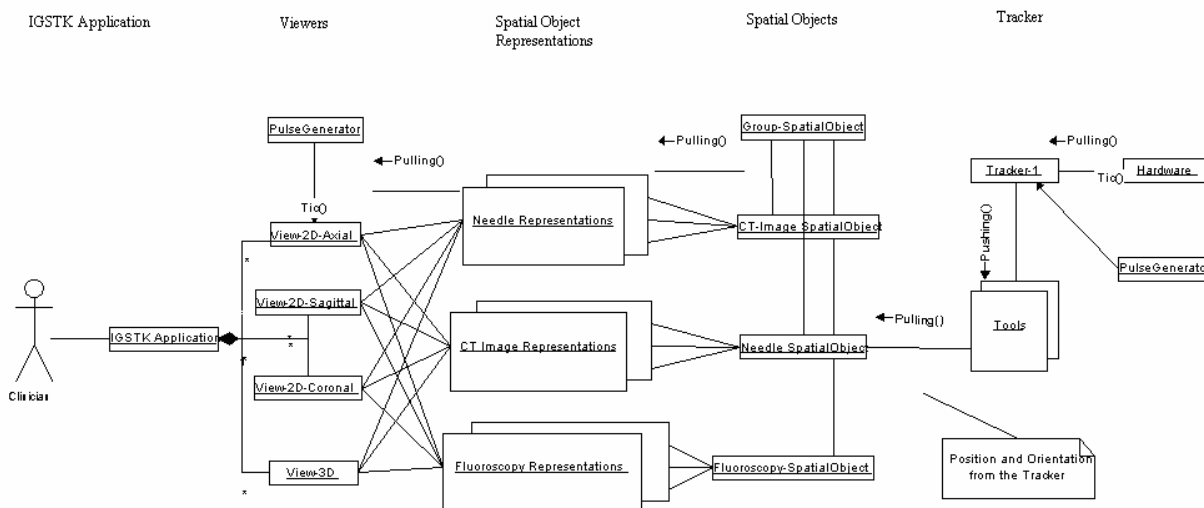

Figure 1: IGSTK Component Architecture

Some other components do not present in Figure 1 include: DICOMImageReader for reading in DICOM images, Landmark3DRegistration for 3D pair-point-based rigid body registration, Logger for logging debug or other information, and Calibration class for calibrating tracker tools. All these together provide essential functionalities to build an image-guided system.

3. EXAMPLE APPLICATION

This section describes the procedure to develop an image-guided biopsy application using IGSTK. A typical image-guided needle biopsy procedure involves first acquiring a pre-operative CT image and then registering the CT image to the patient coordinate system. For this purpose, fiducial-based rigid body registration techniques are commonly used. During the biopsy phase, the needle is tracked by an optical tracking device with real-time visualization of its location overlaid on top of the CT image. This overlay image provides guidance to the surgeon for better targeting of the needle to its desired location. In this example, state machine is being implemented at the application level. While this is not mandatory, it is strongly recommended when using IGSTK. A state machine architecture gives the application developer an easier way to prototype the application and to control the work flow of the surgical procedure, and also adds an extra layer of security to the application to make it more robust. The following sections demonstrate how to write an application using the IGSTK framework.

3.1 Prototyping
The first step is to analyze the surgical application and develop a least a minimal specification. By analyzing a typical needle biopsy procedure, we identify the following essential tasks in this procedure [9].
1. Obtain the patient demographic information (name, etc.).
2. Load in the pre-operative CT image using the DICOM file format. Fiducials (small markers) are usually placed on the anatomy prior to the scan for landmark based registration in Steps 4-7.
3. Verify the patient information against the information in the image. Prompt the surgeon if there is a discrepancy. This step is typical of the error checking that should be done and one should assume that if anything can go wrong it will go wrong and safeguards should be provided.
4. Identify the image landmarks by going through the CT image slices and selecting the fiducials using the mouse. For paired-point based registration, at least three points are required although at least four are preferred.
5. Initialize the tracking device.
6. Add patient landmarks by touching the physical fiducials attached to patient using the tracked pointer device.
7. Perform the image to patient landmark registration.
8. Path planning. The surgeon will select a target point and an entry point to plan the path for the needle puncture.
9. Provide a real-time display of the overlay of the needle probe and pre-operative images in the quadrant viewer window during the biopsy procedure.

Since the application is implemented as a state machine, the completion of each task will cause the application to enter a new state, and there will be a set of states to indicate the status of the application. The user interaction with the GUI can be translated into inputs to the state machine. For instance, when we click on the register patient button, this will generate a "RequestSetPatientNameInput" to the state machine. The state machine will take this input and change its current state from "InitialState" to "WaitingForPatientNameState", and the action is to pop up a window asking for input of the patient name. If the user inputs a valid name, then there will be a "PatientNameInput" which brings the state machine into "PatientNameReadyState", otherwise there will be a "PatientNameEmptyInput", which will return the state machine to the "InitialState". Thus, we can map the application into series of states and inputs and this higher level abstraction will help the developer design a clear work flow for the application. Figure 2 shows the state machine diagram for the needle biopsy application which was generated automatically when the state machine is constructed using the dot tool from graphviz [10].

Figure 2: State machine diagram for needle biopsy application. (Circle for state and arrow for transition and corresponding input)

3.2 Coding the state machine

This section shows how to code the state machine into the needle biopsy application. IGSTK has a number of convenient macros to facilitate the programming of the state machine. The details of these macros can be found in Source/igstkMacro.h. More information on the state machine design pattern and guidelines can be found on the IGSTK wiki page under "Development" section on "Design discussions" page [12]. Note that these URLs are current as of the time of publication (Feb. 2006) but are subject to change in the future.

Once we have the higher level abstraction of the application and prototyped it in the state machine model, we need to take the following steps to program the state machine into the applications.

1. The first step is to use the state machine declaration macro in your class's header file. This macro defines types for state and input, creates a private member variable m_StateMachine, and two private member functions for exporting the state machine description into dot format for the state machine diagram visualization [10] and LTSA (Labeled Transition Systems Analyzer) format for state machine animation and validation [11].
   igstkStateMachineMacro();

2. Then take the states and inputs mapped out during the prototyping stage and define them in the header file using the following macros. To enforce the naming conventions of the state machine, the declaration macros will append "State" or "Input" automatically after the variable name. For instance, the following two lines will define m_InitialState and m_RequestLoadImageInput.
   igstkDeclareStateMacro(Initial);
   igstkDeclareInputMacro(RequestLoadImage);

3. The next step is to construct the state machine in the constructor of the source file. First, we need to add all the states and inputs declared in the header into the state machine.
   igstkAddStateMacro(Initial);
   igstkAddInputMacro(RequestLoadImage);

4. The next step is a crucial step which creates the state machine transition table to control the logic and workflow of the application. This is done using the macro igstkAddTransitionMacro(From_State, Received_Input, To_State, Action). This means when the state machine is in the "From_State" and receives the "Received_Input", it will enter into the "To_State" and evoke the ActionProcessing() as an action for this transition. This macro requires the "ActionProcessing" method to be pre-defined in the class for the state machine to call. For example:
   igstkAddTransitionMacro(Initial, RequestSetPatientName, WaitingForPatientName, SetPatientName);
In this case, we need to have a SetPatientNameProcessing() method defined in the class for this code to compile.

5. After we have setup the transition table, the next step is to select an initial state, and flag the state machine to be ready to run. After the state machine is ready to run, we cannot change the state machine transition table in the code. This is designed this way to enhance the safety of the state machine and prevent accidentally changes to the state machine behavior in the code.
   igstkSetInitialStateMacro(Initial);
   m_StateMachine.SetReadyToRun();

6. Now the state machine is setup and ready to run. We can then export the state machine description in dot format and generate the graphical visualization as shown in Figure 2. This graph will help us to examine the workflow of the application and the state transition table.
   std::ofstream ofile;
   ofile.open("DemoApplicationStateMachineDiagram.dot");
   const bool skipLoops = false;
   this->ExportStateMachineDescription(ofile, skipLoops);
   ofile.close();

This will output the state machine into a dot file when we execute the application. If you have the dot tool installed in your system, then you can run the following command, which will take the dot file and generate a png format picture named "SMDiagram.png" for the state machine.

> *dot –T png –o SMDiagram.png DemoApplicationStateMachineDiagram.dot*

7. All the requests to a state machine should be translated into inputs and the state machine will response to those inputs depending on its current state. These actual actions should be protected methods and only called by the state machine directly. In the code, a click on the load image button will be translated to a 'RequestLoadImageInput', and then we call ProcessInputs() to let the state machine handle this request.

> *igstkPushInputMacro(RequestLoadImage);*
> *m_StateMachine.ProcessInputs();*

If the state machine is in the right state to load the image, a protected method associated with this transition (eg. LoadImageProccessing()) will be evoked by the state machine as defined in the transition table constructed in the constructor.

3.3 Discussion

From the computational theory point of view, all computers are state machines, and all computer programs are state machines regardless of whether the developers used the state machine programming pattern or not. Traditional programming approaches represent the states ambiguously by using a large number of variables and flags, which result in many conditional tests in the code (if-then-else or switchcase statements in C/C++). Programmers could neglect to consider all possible paths in the code while struggling with if-else conditional tests and flag checks. These practices may result in unpredictable behavior and limit safety in the design of the underlying applications. Since predictability is critical for mission critical applications running in the surgery room, this approach is not suitable for our purpose.

In comparison to traditional approaches, state machines will reduce the number of paths in the code, save the developers from convoluted conditional tests, and encourage them to focus on higher level design. From the above example, we can see that the state machine is easy to program and manage under the IGSTK framework. We encourage developers to design and code the state machine of their application first, and then generate the state machine diagram as shown in Figure 2. They can go through the diagram, examine and verify their design of the work flow. If they want to add or change a path of the application, it is just a matter of adding or deleting a transition table entry. This eliminates the level of difficulty required for going through the code and struggling with if-then-else logic. This will largely facilitate the application prototyping, and the implementation code can be plugged into the skeleton program later. These techniques should result in clearer designs and safer applications.

Figure 3 shows the user interface of the needle biopsy application written in FLTK. The left side is the control panel, consists of a set of buttons corresponding to the series of tasks performed during the procedure. These buttons' callbacks should call the public request methods of the application, which will be translated into state machine inputs. The state machine will then take proper action according to its own state. For example, when the patient information is not set, the 'Load Image' button won't respond to the user click. There is no need for conditional checks or disabling of buttons here as these actions are already in the state machine transition table. On the right hand side, there are four standardized views, axial, sagittal, coronal, and 3D view. Here we loaded an abdominal phantom CT image. The green cylinder represents the needle being tracked by the tracker. The viewer will automatically reslice the images as the needle tip is moving in the anatomy.
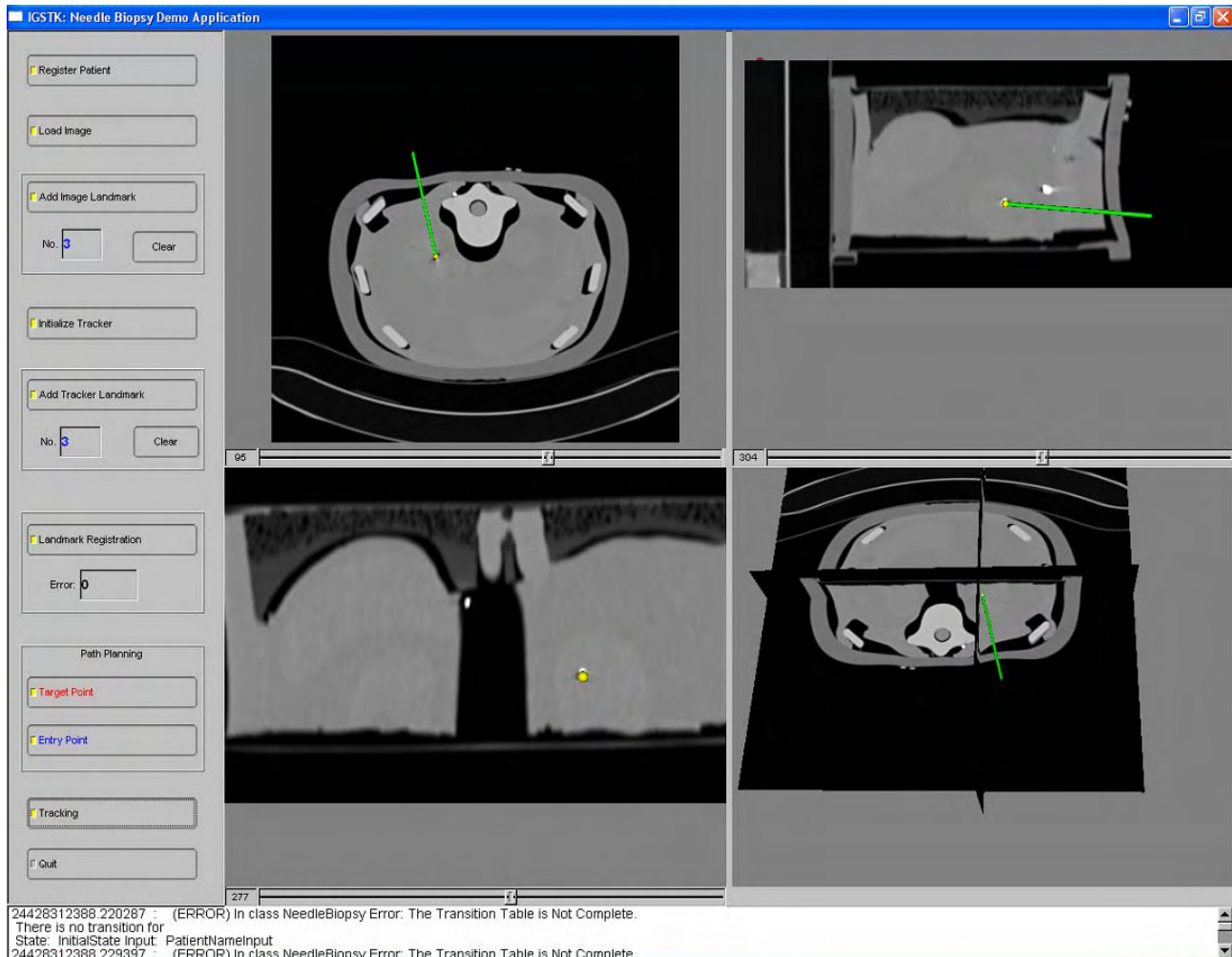
Figure 3: Snapshot of the needle biopsy application

4. CONCLUSIONS

The major components of the toolkit have been completed. Automated nightly testing results can be found at http://public.kitware.com/dashboard.php?name=igstk. The current code coverage on tests is around 95.7%. A state machine validation tool is being developed using LTSA [11], which can animate the transition of the state machine. This tool can be found on the IGSTK wiki page under "Quality" section on "IGSTK State Machine Validation" [12].
This tool is being developed to test all possible combination of inputs to a state machine, which will allow automated testing of applications implemented with state machine. We are planning on releasing three demo applications with this toolkit. The "Needle Biopsy" application as illustrated in the previous sections is available. "Ultrasound Guided RFA" and "Guidewire Tracking" will be available before this phase of the project ends later this year.

The IGSTK toolkit is open source software distributed under a BSD-like license. Basic information related to IGSTK can be found at the website www.igstk.org and the wiki pages [12]. Instructions for configuring and building the toolkit are available at IGSTK wiki page under "Documentation" section on "How to build IGSTK" and "IGSTK: Tutorial". You are welcome to try the software, review the source code and send your comments and report bugs to the IGSTK user list, igstk-users@public.kitware.com. Note that this software should only be used in clinical cases under IRB approval. You are allowed to use IGSTK for free in academic and commercial applications but it is your responsibility to perform the tests and validations required by regulatory bodies such as the U.S. Food and Drug Administration (FDA).

ACKNOWLEDGMENTS

REFERENCES

1. L. Ibanez and W. Schroeder, "The ITK Software Guide", ISBN 1-930934-10-6, 2005 http://www.itk.org/ItkSoftwareGuide.pdf
2. W. Schroeder and K. Martin, B. Lorensen, "The Visualization Toolkit, An Object Oriented Approach to 3D Graphics", Kitware Inc., 1998
3. FLTK a cross-platform C++ GUI Toolkit, http://www.fltk.org/documentation.php/doc-1.1/toc.html
4. L. Ibanez, J. Jomier, D. Gobbi, R. Avila, M. B. Blake, H. Kim, K. Gary, S. Aylward, and K. Cleary. "IGSTK: A State Machine Architecture for an Open Source Software Toolkit for Image-Guided Surgery Applications." Insight journal, Aug 2005
5. K. Cleary, L. Ibanez, S. Ranjan, and M.B. Blake. "IGSTK: A Software Toolkit for Image-Guided Surgery Applications." CARS 2004
6. J.E. Hopcroft, et al., Introduction to Automata Theory, Languages, and Computation, Addison Wesley (2nd ed.), 2000.
7. K. Gary, M. B. Blake, L. Ibanez, D. Gobbi, S. Aylward, and K. Cleary." IGSTK: An Open Source Software Platform for Image-Guided Surgery." Submitted to IEEE Computer
8. E.Gamma, et al., Design Patterns: Elements of Reusable Object-Oriented Software, Addison-Wesley, 1995.
9. F. Banovac, N. D. Glossop, D. Lindisch, D. Tanaka, E. Levy, and K. Cleary: Liver Tumor Biopsy in a Respiring Phantom with the Assistance of a Novel Electromagnetic Navigation Device. MICCAI (1) 2002: 200-207
10. Graphviz - Graph Visualization Software, http://www.graphviz.org
11. LTSA - Labelled Transition System Analyser, http://www.doc.ic.ac.uk/~jnm/book/ltsa-v2
12. IGSTK wiki papge, http://public.kitware.com/IGSTKWIKI

8.3 Cleary 2006: Interventional Robotic Systems …

Reprint begins on the next page and is 21 pages.

Title Page

Interventional robotic systems: applications and technology state-of-the-art

Authors:
Kevin Cleary, PhD (corresponding author)
Vance Watson, MD
Imaging Science and Information Systems (ISIS) Center
Department of Radiology
Georgetown University Medical Center
2115 Wisconsin Ave., Suite 603
Washington, DC 20007
Email: cleary@georgetown.edu, vance@vancewatson.com

Dan Stoianovici, PhD
URobotics Laboratory
Urology Department
Johns Hopkins Medicine
Baltimore, Maryland, USA
Email: dss@jhu.edu

Gernot Kronreif, PhD
Mechatronic Automation Systems - Robotics Lab
ARC Seibersdorf research
A-2444 Seibersdorf / Austria
E-mail: gernot.kronreif@arcs.ac.at

Andreas Melzer, MD
Institute for Innovative Technologies and Management in Medicine INSITE med. &
Dept. of Physical Engineering
University of Applied Sciences
Neidenburger Strasse 43
D-45877 Gelsenkirchen,
Germany
&
St. Mary's Hospital Buer
Dept of Radiology
45894 Gelsenkirchen Buer
e-mail: andreas.melzer@fh-gelsenkirchen.de

Abstract

Many different robotic systems have been developed for invasive medical procedures. In this article we will focus on robotic systems for image-guided interventions such as biopsy of suspicious lesions, interstitial tumor treatment, or needle placement for spinal blocks and neurolysis. Medical robotics is a young and evolving field and the ultimate role of these systems has yet to be determined. This paper presents four interventional robotics systems designed to work with MRI, CT, fluoroscopy, and ultrasound imaging devices. The details of each system are given along with any phantom, animal, or human trials. The systems include the AcuBot for active needle insertion under CT or fluoroscopy, the B-Rob systems for needle placement using CT or ultrasound, the INNOMOTION for MRI and CT interventions, and the MRBot for MRI procedures. Following these descriptions, the technology issues of imager compatibility, registration, patient movement and respiration, force feedback, and control mode are briefly discussed. It is our belief that robotic systems will be an important part of future interventions, but more research and clinical trials are needed. The possibility of performing new clinical procedures that the human cannot achieve remains an ultimate goal for medical robotics. Engineers and physicians should work together to create and validate these systems for the benefits of patients everywhere.

1   Introduction

Many different robotic systems have been developed for invasive medical procedures. In this article we will focus on robotic systems for minimally invasive interventions such as biopsy of suspicious lesions or needle placement for spinal blocks. According to the Robotic Institute of America, a robot is "a reprogrammable, multifunctional manipulator designed to move materials, parts, tools, or other specialized devices through various programmed motions for the performance of a variety of tasks." For our purposes, this definition fits most medical robotics systems fairly well, in that they are typically mechanical manipulators with rigid links connected by joints that allow relative motion from one link to another (1).

Medical robotics is a relatively young field, with the first recorded medical application of a robot occurring in 1985 (2). Unlike factory robotics, in which virtually all operations are now automated and the use of robotics is widespread, medical robotics is still a niche field. While medical robots have been applied in many fields such as neurosurgery, orthopedics, and urology, they are not the standard of care in any field and in fact very limited market penetration has occurred. This limited use is no doubt due to the many challenges that need to be overcome in developing a robotic system for a medical application. In particular, safety is an overriding concern and must be considered from the start in any medical robotic system. Note that in the factory, we do everything we can to keep people away from robots, but in the medical environment many robotic systems are designed to work with people nearby, and all medical robotics systems must ensure safe operation with a patient in the workspace of the robot. Despite these challenges, we believe that medical robotic systems have a place in minimally invasive procedures and this article describes several systems developed by the authors for this purpose.

There are many other robotic systems which have been developed and there are several review articles that have been written in the past few years such as (3-6) In particular, there are two systems that are currently used in clinical practice that should be mentioned here. The first system is the da Vinci® from Intuitive Surgical (Sunnyvale, California, USA) which functions along the line of a master – slave telemanipulator for endoscopic surgical procedures (7). The da Vinci consists of the surgeon's viewing and control console, a control unit, and a three-arm surgical manipulator (8). While the initial application of the system was cardiac surgery, a recent focus of the company has been on urological surgery, specifically minimally invasive prostatectomy. According to the manufacturer, about 400 systems have been installed to date. The second system is the CyberKnife® from Accuray (Sunnyvale, California, USA) for stereotactic radiosurgery. The CyberKnife consists of a lightweight linear accelerator, a KUKA robot, paired orthogonal x-ray imagers, and a treatment couch (9). The system was originally developed to treat tumors in the brain and spine, but is now FDA approved to treat lesions anywhere in the body including the lung and pancreas. According to the manufacturer, over 100 systems have been sold to date.

The article is organized as follows. In Section 2, which is the bulk of the article, we describe four interventional systems designed to work with MRI, CT, fluoroscopy, and ultrasound imaging devices. The details of each system are given along with any

phantom, animal, or human trials. The paper concludes with a presentation of some technology issues in Section 3 and a discussion and summary in Section 4.

2   Interventional Robotics Systems

In this section, four interventional robotics systems which were developed by the authors will be presented. Table 1 lists the system name, institution where the system was developed, the status (phantom, animals, clinical trial), and the imaging modality used. Note that these systems are representative examples of the state of the art in interventional robotics. There are other systems that have been built and the reader is referred to the review articles listed earlier for more details.

System	Institution	Status	Imaging Modality	Section in paper
AcuBot	Hopkins/Georgetown (USA)	Cadaver studies Animal studies Clinical trial done	Fluoroscopy and CT	2.1
B-Rob	ARC Seibersdorf research (Austria)	Phantom studies	CT and ultrasound	2.2
INNOMOTION	Innomedic/FZK/ FH Ge (Germany)	Animal studies Clinical use starting CE marked	MRI and CT	2.3
MRBot	Hopkins (USA)	Phantom studies	MRI	2.4

Table 1: The four interventional robot systems described in this article

2.1   Acubot

The AcuBot (10) robot presents a modular structure of several functionally distinctive components that have been developed over the past five years in the URobotics Laboratory at Johns Hopkins Medical Institutions (Baltimore, USA). The AcuBot incorporates the original PAKY (percutaneous access of the kidney) radiolucent needle driver (11); a RCM (remote center of motion) module capable of needle orientation (12); an XYZ Cartesian stage for translational positioning of the needle tip; and a passive positioning arm (S-arm) mounted onto a bridge frame.

Figure 1 shows two views of the robot mounted on a CT scanner. The base of the robot [2] provides a bridge-like structure over the table. The robot has a total of six active degrees of freedom (DOF) configured for decoupled positioning, orientation, and instrument insertion.
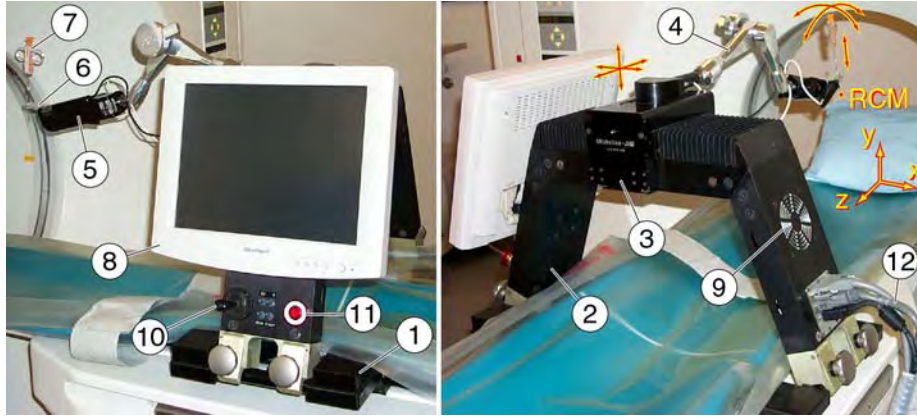

Figure 1: a) Front and b) side views of the AcuBot

The instrument [7] is loaded in PAKY [6], which is an active radiolucent needle driver (T translation). PAKY is held by the RCM (11) module [5]. This module is capable of precisely orienting the instrument about two nearly perpendicular directions (Rx and Rz) coincident at the RCM point, thus allowing a pivoting motion about that point. The RCM is supported by a passive positioning arm [4], called the S-ARM, with 7 DOF (S1 spherical, R revolute, S2 spherical). The arm can be positioned and rigidly locked from a single lever. The base of the arm [4] is mounted in a 3 DOF Cartesian stage [3], the XYZ module (Tx, Ty, and Tz translations). The user interface consists of a 15" resistive touch screen [8], a two-axis joystick, a switch panel [10], and an emergency stop button [11]. These components are mounted on the front side of the bridge. A speaker [9] and the cable connector [12] are located on its back side.

2.1.1 Needle Registration and Clinical Studies in CT Scanners

The method is based on aligning the procedure needle held by the robot with the laser markers of the CT scanner. The robot can then automatically orient the needle toward a target selected in a CT slice. The skin entry point and target location may be contained in different slices. Needle insertion may then be performed under joystick control or automatically under CT fluoroscopy (CTF) monitoring by the physician.

This method showed an experimental accuracy of less than 1 mm in-slice and 1.5 mm for out-of-slice targets. Four clinical cases of kidney and spine biopsy and RF ablation (Figure 2), and a nephrostomy tube placement were successfully performed with no complications (13). These cases demonstrated a significant improvement over the manual method, in which the needle is typically restricted to the CTF plane so that the needle can always be seen by the physician.

Another study (14) with the same robotic system found the in-vitro accuracy of the robot to be 0.6° angular and 1.65 mm linear. The clinical study included 10 percutaneous core biopsies (7 kidney, 2 lung, 1 liver), 11 RF ablations (9 kidney, 2 spine), 1 nephrostomy tube placement, and one neobladder access. In four cases, the target was not met adequately, and fine-tuning adjustment with the joystick was required to reach the target. In all cases, however, the study showed that the use of the robot reduced radiation exposure for the patient and medical personnel.
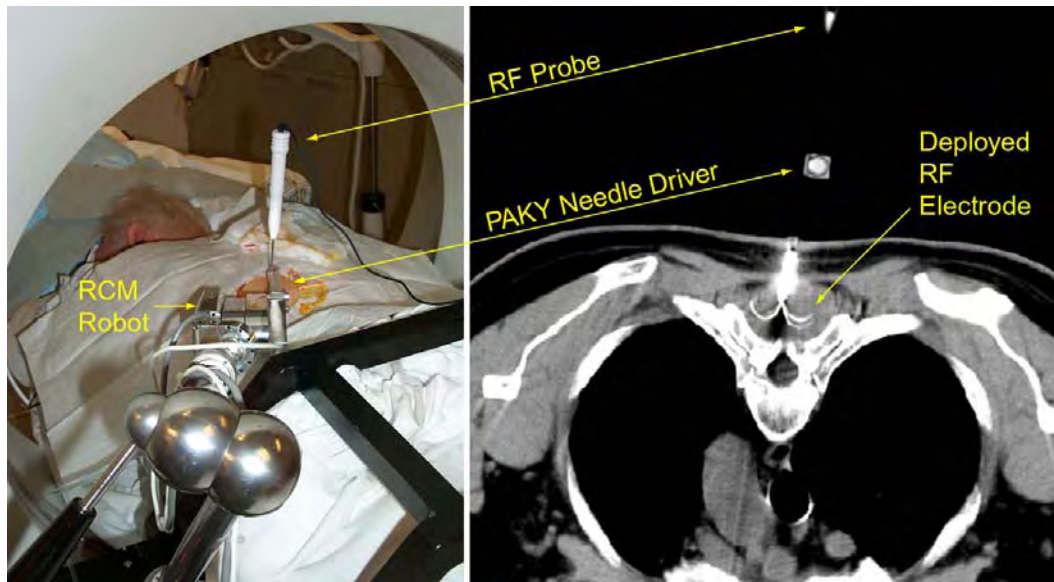

Figure 2: CT-guided RF ablation with PAKY-RCM system and laser based registration

2.1.2 Clinical Trial for Nerve Blocks under Fluoroscopy

After cadaver studies using the robot to precisely position a needle in the lumbar spine were successfully completed (15) in the Department of Radiology at Georgetown University, a randomized clinical trial of 20 patients undergoing nerve and facet blocks was approved by the FDA and the local institutional review board. The procedure was done following the usual clinical practice except the robot was used to position, orient, and drive the needle under physician control. A/P fluoroscopy was used to position and orient the needle, and lateral fluoroscopy was used to monitor the depth of insertion.

The robot was mounted on the interventional table using a custom-designed locking mechanism. The robot was positioned initially near the skin entry point by loosening the passive gross positioning mechanism and moving the needle driver end of the robot by hand. Once this initial position had been attained, the mechanism was locked and the robot was switched to operate by physician control using the joystick.

The study was completed by a single fellowship trained interventional neuroradiologist at Georgetown University Hospital using a Siemens Neurostar bi-plane fluoroscopy system. The standard manual technique was used on 10 patients and the robotic device was used on 10 patients. The patients ranged in age from 30 to 70 years. The spine

levels were from S-1 to L-5. No complications were observed in the study. One of the patients in the robotics arm had to be converted to a manual procedure due to slippage of the needle driver. This conversion was done without difficulty or complications. There were two outcome measures: 1) accuracy of needle placement and 2) pain relief. Accuracy of needle placement was determined as follows. Before the interventionalist began placing the needle, both an A/P and lateral image of the patient were obtained. The interventionalist would then annotate each image with an arrow to indicate the desired target location of the needle (the interventionalist was not blinded as to manual/robotic technique as this was not practical). After the needle was placed, an A/P and lateral image was again obtained. The two sets of images were compared to determine the distance between the intended location of the needle and the actual location of the needle. Pain relief was measured using a visual-analog scale, with 0 representing no pain and 10 representing excruciating pain.

The results to date show that is feasible to use a joystick controlled robot for nerve and facet blocks. An example case is shown in Figure 3. While this was a pilot study and not enough data was gathered for statistical significance, some general trends can be observed. The mean accuracy in the robot (1.105 mm) and manual (1.238 mm) is about the same. Therefore, it appears that the robot is capable of accurate needle placement.

As expected, the pain score post-treatment was significantly less than the pain score pre-treatment in both the robot and manual arms. In the robot arm, pain scores fell from a mean of 6.3 pre-treatment to 1.8 post-treatment. In the manual arm, pain scores fell from 6.0 pre-treatment to 0.9 post-treatment. Patients had to sign an informed consent form and were generally receptive to the use of the robot.
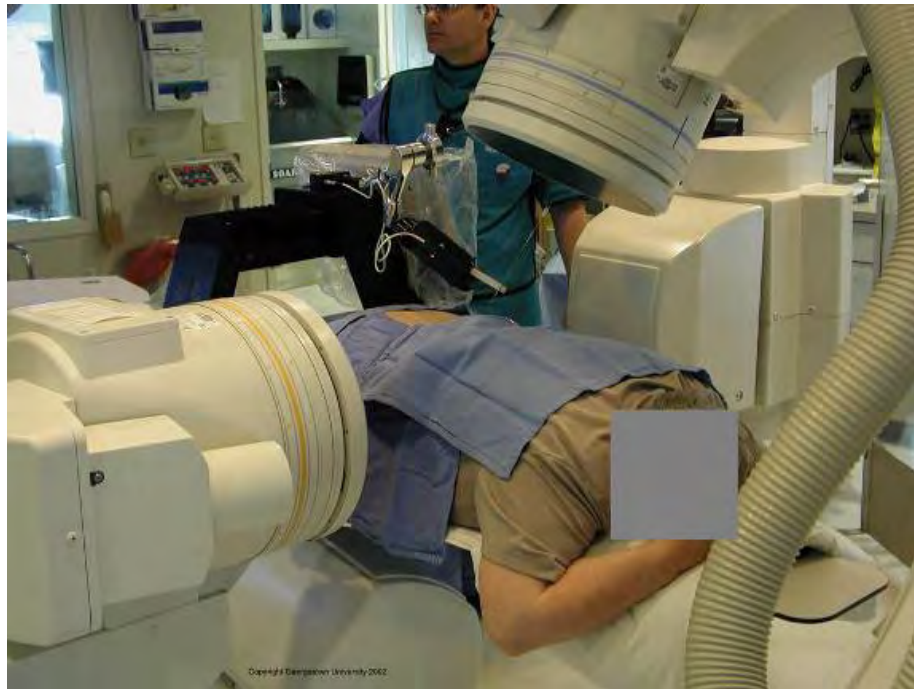

**Figure 3: Clinical trial of robotically assisted nerve blocks
at Georgetown University under biplane fluoroscopy**

2.2   B-Rob Systems – ARC Seibersdorf Research

Robotic systems for CT and ultrasound-guided biopsies have been developed by the robotics laboratory of ARC Seibersdorf Research in Austria. The two systems developed by this group are presented here.

2.2.1   Prototype Biopsy Robot I (B-RobI)

The first prototype biopsy robot was called B-RobI and was a seven degree of freedom (DOF) stand-alone robot system integrated on a mobile rack (16). The biopsy instrument is positioned at the skin entry point by a 4-DOF gross positioning system consisting of three Cartesian linear axes together with one additional rotational link for a rough orientation of the needle. For final orientation of the needle the robot is equipped with a "Needle Positioning Unit" (NPU) consisting of two linear DOFs which move two parallel carbon "fingers" connected by spherical links. Another linear DOF with a limited stroke of 50mm can move the entire NPU toward the skin entry point in a safe approach movement, i.e., with minimal velocity and force. The needle orientation stage is thus strictly decoupled from movement of any axis of the gross positioning system. A remote center of motion ("pivot point") for angulation of the needle is maintained by the kinematic structure of the NPU as another safety measure during the intervention.

The robot system is controlled by two industrial PCs. One PC provides high-level control of the robot system and a second PC handles the interface to the optical tracker system (Polaris, Northern Digital) as well as the planning and monitoring software. This PC also includes a video capture card (WinTV-PCI-FM 718, Hauppauge) for grabbing images from an ultrasound probe or the CT monitor to support planning of an intervention. After acquisition of images of the target region, the physician selects the desired skin entry point as well as the target point. With that information the relevant data (angulation, distance to the target lesion) are calculated and automatically sent to the robot controller via TCP/IP socket connection. Using the GUI of the planning software, the virtual trajectory of the biopsy can be viewed in all CT-slices involved to verify the intervention path. After planning of the intervention, the robot can be moved towards its final position by a coordinated motion of the axes. The gross positioning unit can then be locked if desired. The NPU is then moved to the skin entry point under very controlled conditions (at low speed and with limited distance) and the needle can be manually inserted.

The performance of the complete system has been extensively evaluated in a series of in vitro tests using a needle-penetrable phantom (17-19). Peas (mean diameter=9.4±0.7mm) were embedded as targets within a custom-made gel-phantom. Based on the intervention plan, the NPU was commanded to the desired skin entry point to provide guidance for a 17-gauge coaxial puncture needle and an 18-gauge long biopsy needle. After manual needle insertion, sample harvesting was performed by means of an automated biopsy device (Magnum Core high speed; 22-mm excursion). The distance between the actual needle tract and the centre of the target was evaluated in two orthogonal axes using ultra-sonography - the length of the harvested biopsy specimen also was evaluated by direct measurement. Test series were performed for both US-guided biopsies (scanning head C4-2; US-System HDI-UM 9, Advanced Technology Laboratories, USA) as well as for CT-guided interventions (Multidetector CT,

Siemens Somatom Sensation 16; CareVision Mode, 0.75 c 0.75, 80kV, 160 mAs, 0.5 sec). Photographs of the CT tests are shown in Figure 4 and Figure 5.

The system showed sufficient operational stability and accuracy for the procedures under consideration. The measured targeting accuracy (1.48mm ± 0.62mm) is better compared to traditional techniques by additionally combining the advantages of needle guidance and free-hand technique. Integration of the complete system on a mobile rack allows short setup time and easy installation of the system at different sites. On the other hand, the chosen approach leads to a very bulky system and to a very high grade of automation.

**Figure 4: Biopsy robot I during in vitro testing for
image-guided interventions under CT fluoroscopy**

Figure 5: Close-up of testing showing phantom (peas can be seen in the bag), needle positioning unit (NPU), and optical trackers

2.2.2 Biopsy Robot II (B-RobII)

The main goal for this new design was to transfer the concepts demonstrated from the B-RobI prototype into a practical clinical setup. The major goals for the new development were:

1. a modular setup for a broad variety of clinical applications,
2. a significant reduction of technical complexity (compared to the previous prototype) to reach an acceptable cost/benefit ratio for the entire system,
3. easy integration to devices used in interventional radiology,
4. seamless integration to clinical workflow, and
5. a "plug&play" philosophy.

The mechanical architecture for the new design was based on the parallelogram mechanism already realized for the NPU of the B-RobI prototype. For easy sterilization, the two carbon "fingers" - together with the polymer bearings and the needle guideway - can be disconnected from the positioning module (i.e. the robot) by means of a rapid-change bayonet connection. The mechanical design of the device is low-profile (dimensions of one 2DOF module: WxLxH = 100mm x 150mm x 30mm) in order to use the system inside of the CT gantry without major restrictions. Following the general idea of modularity, different configurations are supported in order to allow simple 2DOF

needle angulation (+/- 30°), 2DOF positioning (+/- 20 mm) as well as (optional) maintaining a software defined pivot point for angulation. For gross positioning of the needle entry point, the module(s) are mounted on one or two passive 7DOF multi-functional holding arm(s) (ATLAS arm, Medical Intelligence GmbH, Schwabmünchen, Germany).

The robot control system was developed in-house and consists of two axis controllers for each module, a safety card which disconnects all motors from the power supply in case of an emergency stop, and a power supply module – all of which are integrated into a HF-dense 19" housing. All modules are interconnected via a standard RS485 bus system. Operation of the entire system is synchronized either via a PC (MDD certified computer or panel PC) connected to the RS485 bus or via a hand-held control unit in stand-alone operation. Thanks to this modular setup, single modules can be easily replaced and the system can be expanded easily.

Planning of the intervention is based on imaging data sets acquired immediately before an intervention. The spatial relation between the imaging space and the targeting device is either established by means of a tracker system (optical or mechanical) or via robot registration based on a CT-data set. After graphical selection of the target and manual pre-positioning of the device, the correct angulation will be set automatically by the system. During the intervention, the robotic kinematics holds the needle guide in a predefined position and orientation. However, the insertion of the needle itself will be performed manually by the physician.

The first in vitro trials of the system using a penetrable gel phantom show that B-RobII allows image-guided positioning of a biopsy needle with high accuracy (0.66mm ± 0.27mm). The system is easy to use and does not considerably interfere with the clinical work-flow. A risk analysis of the complete system (20) did not find any major risks. A series of quantitative evaluation studies - for both US and CT guided biopsies and for different system setups (no/ mechanical/ optical tracker; remote controlled operation) is currently in process. Beside biopsy procedures, further clinical applications are currently under evaluation at different research centers. The long-term goal of this work is to create a multi-purpose system for a broad range of percutaneous treatments, in any part of the body, using any kind of intra-operative image guidance.

Figure 6: Biopsy robot II in a 2 by 2 degree of freedom configuration mounted on two passive holding arms

Figure 7: Biopsy robot II during initial phantom study

2.3   CT and MR-Compatible Robotic Instrument Guiding System INNOMOTION

MR-guided percutaneous interventions have been clinically established with open low field MR systems (21). As the imaging quality of closed bore scanners is superior to open field system but the access to the patient is limited a fully MR-compatible assistance system INNOMOTION (Innomedic, Herxheim & FZK Karlsruhe Germany) {Gutmann, 2002 #47;Bock, 2004 #48}) was developed to provide precise and reproducible instrument positioning inside the magnet. MRI compatibility has been achieved through testing of all components and the complete system in different field strength magnets including a 1.5 T Siemens Magnetom Symphony and Philips 1.0 T Gyroscan and 1.5 T magnets. Targeting precision has been determined with a mechanical FARO arm on ex vivo organ models embedded in agarose gel. Targeting precision has also been evaluated during MRI guided percutaneous interventions in a porcine animal model. The system is shown in Figure 8.

2.3.1 Technology

The pneumatic robotic assistance system is fully MR-compatible and consists of a robot arm which can be manipulated in 6 degrees of freedom (22-23). The robot arm is attached to a 260° arch that is mounted to the patient table of the scanner and can be passively prepositioned on either side of the arch at 0°, 30° and 60° to the vertical

according to the region of interest (e.g. spine, liver, kidney, breast). Active positioning measurements are achieved via fiber optically coupled limit switches, along with rotational and linear incremental sensors. The kinematics of the device has been carefully optimized for use in close bore MRI scanners and the CT gantry. Piezoelectric drives were tested but due to the RF noise during MRI scanning and the risk of inductive heating of the electric power lines they were not used and pneumatic cylinders with slow motion control have been developed instead to drive all six degrees of freedom.

A module for application of coaxial probes (e.g. cannulae for biopsies, RF or Laser Probe, endoscopes, etc.) provides two degrees of freedom in X and Z axes and is attached to a robotic arm with 4 degrees of freedom. This design assures stable positioning of the instrument with in a tool center point that keeps the "invariant point of insertion" at the skin entry point.
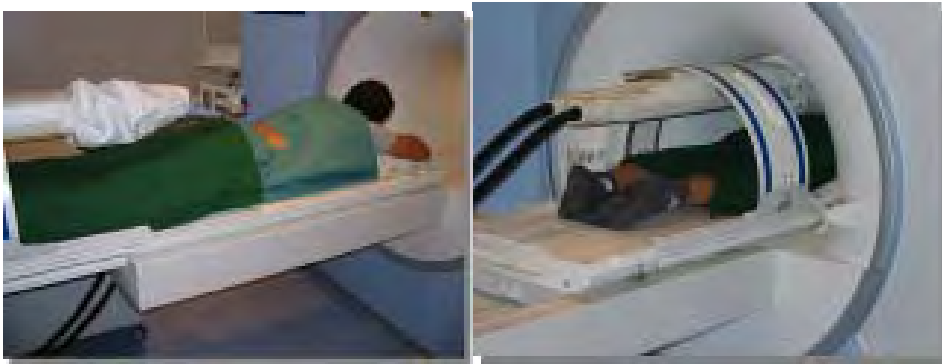

Figure 8: INNOMOTION robot for MRI-guided procedures

The application module (Figure 9) for clinical use provides manual translation and rotation of the cannula. A pneumatic drive has been developed to insert the cannula in incremental steps of 1 – 20 mm. In conjunction with the two axes for movement about the tool center point (+/- 30°) the instrument trajectory can be changed to other targets without moving the robot arm or repositioning the arm on the arch. The arch is movable and can be firmly attached to the patient table of the MR system with exchangeable fittings easily adapted to other MRI platforms (Figure 10). A graphical user interface provides trajectory planning directly on the MRI images (Figure 11 e).

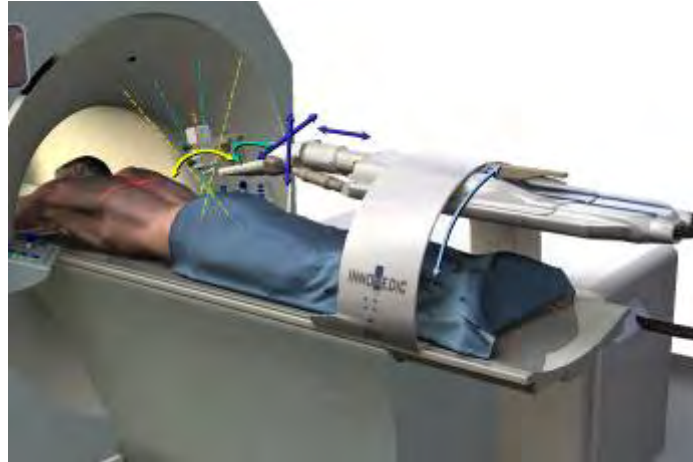**Figure 9: Application module for manual cannula insertion**

Figure 10: INNOMOTION with six degrees of freedom can be mounted on different types of MRI patient beds
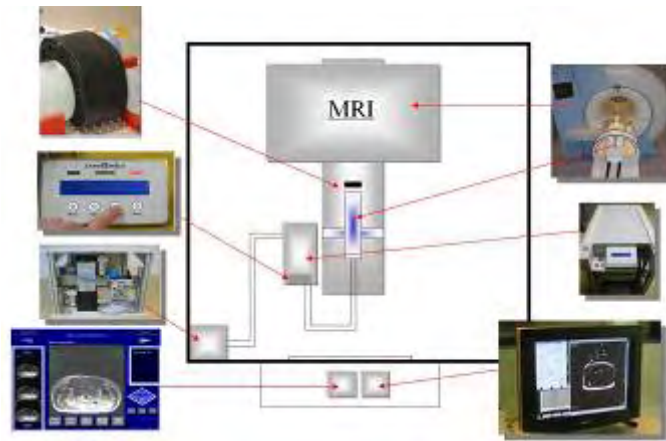

Figure 11: Equipment set up (a) phantom, (b) input panel and (c) in room control unit , (d) pneumatic control, (e) graphical user interface and (f) MRI monitor

2.3.2 Procedure Technique

The patient is placed in a predetermined position suitable for the intervention (supine, prone or lateral). The system is prepositioned and firmly attached to the table with clamps. Based on the pre-interventional images and the anatomical region of interest the table is moved using the projection of the laser lights from the MRI gantry. The robot is referenced to the coordinate system of the MR scanner using the same laser line. The arm moves back and forth and returns so that the light detectors at the upper part of the application module are aligned with the laser (within +/- 0.5 mm). The laser light is switched off and the table is automatically moved in to the MRI bore until the position of the laser line matches with the zero position of the Z-axis of the MRI scanner. Planning for the intervention is performed by using fast gradient echo sequences in transverse, sagittal or coronal orientation. Suitable slices are selected and sent via the network in DICOM format to the computer of the robotic assist system. The insertion site and a target point are selected on the graphical user interface and the corresponding coordinates are sent to the control unit. The drives are activated and the application

module is moved with the tool center point to the insertion site on the skin. The cannula can then be inserted through a guiding sleeve or along an open angle.

2.3.3 Evaluation of Targeting Precision

Mechanical targeting precision has been determined with a FARO arm under dry lab conditions. The MRI procedures were performed on 1.5 T Siemens Magnetom Symphony, and a Philips 1.0 T Gyroscan and 1.5 T Intera. The test were done on ex vivo organ models which consisted of fresh porcine kidney embedded in Agarose and Gelatine (Figure 12).
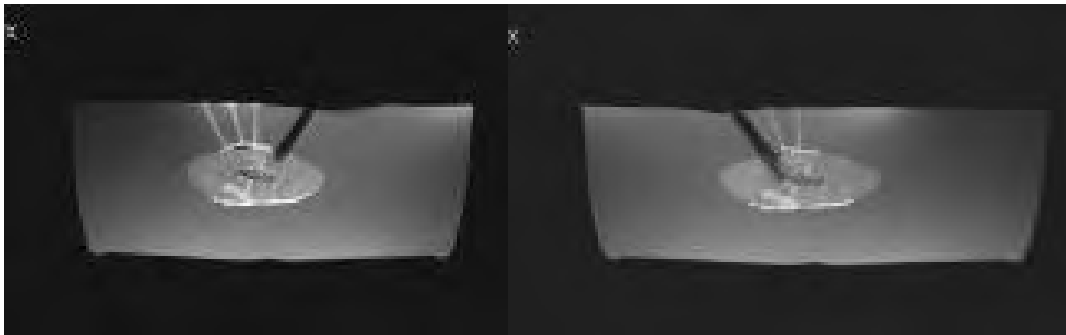

Figure 12: MRI Target precision of 20 Gauge cannula insertion into a porcine kidney embedded in Agarose

Targeting precision was also evaluated during MRI-guided percutaneous interventions in an porcine animal model under general anesthesia (Isoflurane). The animals (four 3-month old domestic pigs 30 – 40 kg) were placed prone on the patient table and a surface coil was fixed around the planed insertion site lateral to the spine. Using T1- and T2-weighted planning images, the appropriate region of interest was defined on the graphical user interface of the INNOMOTION control computer (Figure 13). The robot arm then moved and oriented the needle holder to the insertion point automatically. 20 and 22 gauge MR-compatible Titanium grade 4 cannulae (MRI Devices-Daum, Schwerin, Germany) were then manually inserted. Subsequent to an initial insertion of about 10 mm the table was repositioned in the MRI bore and control images were acquired. The precision of the insertion point and the insertion angle were determined by overlaying the pre-interventional images with the new MRI image.

Figure 13: Overlay images on the INNOMOTION screen for evaluation of target precision

The intervention was completed within the magnet from the rear opening, where an MR-compatible in-room monitor was placed. During the insertion of the needle, real-time MR images were acquired for guidance. To visualize the advancement of the cannula in the tissue fast Gradient Echoes sequences (TR = 4.4 ms; TE = 2.2 ms; FA 70°; TA = 0.7 s) were used. At the desired region of interest (nerve root, plexus coeliacus) spin echo images were acquired for verification of the cannula position through a test bolus of contrast agent solution (NaCl/GdDTPA: 100/1itre of 0.8% saline solution). The injection was done under real-time MRI (TR = 1.8 ms; TE = 4.3 ms ; TA = 0.5 - 0.8sec.; FA = 20°) to visualize the drug distribution. Final therapeutic injection of 10-25 ml with contrast dotted Mepivacainhydrochlorid (Scandicain®1%, Astra - Zeneca, Germany) was performed.

2.3.4 Results and Discussion

All procedures were completed successfully including injections at the sympathetic chain, sciatic nerve and coeliac plexus. The direct MRI control and new sequences techniques allows correction of the insertion path in case of misdirection due to anatomical structures. The insertion site and the insertion angle have been evaluated by manual measurement on overlays of the planning image of INNOMOTION and the subsequent MR control image (Fig. 13). The position and orientation of all cannula insertions were appropriately visualized on axial MRI images. The precision of the insertion site in the axial plane was +/- 1mm (minimum of 0.5 mm and maximum of 3 mm). The angular deviation in the transverse plane of the cannulae was +/- 1° with a minimum of 0.5° and maximum of 3°.

Cross platform MRI compatibility can be achieved by using polymers, ceramics, pneumatic drives and optoelectronic sensors. For MRI-guided cannula interventions, as the cannula is currently advanced manually, the access is difficult if the insertion is done inside the magnet. Therefore, the direct control of the insertion under real-time MRI is recommended to allow correcting the insertion in case of misdirection of the cannula and

to precisely position the tip of the cannula in the volume of interest. To ease the procedure tip tracking techniques haven been evaluated (23).

2.4 MrBot: A Fully MRI Compatible Robot for Prostate Image-Guided Interventions

A new robot, MrBot (24), has been recently developed at Hopkins for fully-automated image-guided access of the prostate gland. The robot is customized for transperineal needle insertion and designed to be compatible with all known types of medical imaging equipment. This includes uncompromised compatibility with MRI scanners of the highest field strength, size accessibility within closed-bore tunnel-shaped scanners, and clinical intervention safety.

The robot is designed to accommodate various end-effectors for different percutaneous interventions such as biopsy, serum injections, or brachytherapy. The first end-effector developed is customized for fully-automated low dose radiation seed brachytherapy. For MRI compatibility the robot is exclusively constructed of nonmagnetic and dielectric materials such as plastics, ceramics, and rubbers and is electricity free. The system utilizes a new type of motors specifically designed for this application, the pneumatic step motors (PneuStep) (25). These uniquely provide easily controllable precise and safe pneumatic actuation. Fiber optic encoding is used for feedback, so that all electric components are distally located outside the imager's room. A photograph of the robot on the MR scanner table is shown in Figure 14.

Figure 14: MR compatible robot developed for prostate brachytherapy at Johns Hopkins (simulation of a clinical procedure)

Motion repeatability tests performed in the MRI scanner show mean errors of 0.076 mm. The robot was found to be compatible with several different imaging devices [25]. The clinical utility of the system remains to be investigated. We are currently evaluating needle insertion accuracy with in-vitro and ex-vivo experiments. An animal protocol has already been filed and approved for in-vivo studies. An institutional review board approval was also received for human trials on robot-scanner ergonomics.

3 Technical Issues

In this section the following technical issues will be briefly discussed:
- o Imager compatibility
- o Registration
- o Patient movement and respiration
- o Force feedback
- o Mode of control

Imager compatibility. For MRI systems, compatibility can be achieved by using nonmagnetic and nonconductive materials. For CT systems, radiolucency of the end-effector is important so that it can hold the instrument on the scan plane. The robot system must also be easily interfaced with the imaging system and allow quick access to the patient in emergency situations. When the robot system is actuated it should not interfere with the imaging system. The kinematic structure of the robot must allow it to reach inside the gantry, which is one reason why specially designed robots are needed for these procedures.

Registration. For a robot to target the anatomy based on the images, the coordinate system of the robot must be registered to the coordinate system of the imaging device. If the robot is permanently attached to the patient table of the imaging device, this registration can be done once through a calibration procedure. If the robot is designed to be moved from one imaging device to another or to be placed on the table for certain procedures, fast and accurate registration techniques are required.

Patient movement and respiration. A limiting problem in some interventional techniques is organ movement due to respiration. A robotic system could react faster than a human and compensate for respiration. This compensation would first require that target movement due to respiration be recognized and accurately tracked. However, for such a system to be clinically viable, robustness and safety would need to be demonstrated.

Force feedback. For robotic systems that include an active needle driver, at present there is no force feedback provided to the operator. The importance of this feedback is a subject of current debate but there are some clinical applications where it seems desirable. However, there is no accurate way to measure the force at the tip of surgical instruments and existing force feedback devices are too bulky for the clinical environment. In addition, friction forces on the cannula and tissue during insertion are high which compromise the accuracy of force feedback measurements. Therefore, this topic must be considered a research issue at this time.

Mode of control. The "best" user interface for an interventional robot has yet to be determined. For many procedures, joystick control seems well-suited and keeps the physician firmly in control. Master/slave systems are also possible and as noted above

force feedback may be helpful here. However, there are procedures such as biopsy where a straight-line trajectory needs to be followed and some degree of autonomy seems appropriate if robustness can be achieved.

4   Discussion and Summary

As percutaneous procedures with cannulae and probes under image guidance continue to increase in numbers and importance, as they have the past several years, there will be more demand for technological assistance.   In this role, image-guided robots may have a place and this place needs to be demonstrated in randomized clinical trials. Ten years ago image-guided procedures largely consisted of biopsies. Over the past decade interventional techniques have blossomed and include procedures to ablate tissue with energies such as radiofrequency, heat, cold, and laser. Reconstructive procedures have also developed. An example is vertebroplasty and kyphoplasty in which methymethacrylate is injected into vertebra to increase stability and to reduce pain.

Robots have some potential advantages over the human operator in certain applications. Examples include working in hazardous environments such as imaging rooms where radiation is used. During fluoroscopic or CT guided procedures the operator frequently advances the cannula with the imaging beam off and then acquires an image to identify the current position of the tip. Options to overcome the limitation of intermittent imaging include stand-off devices to keep the operators hands out of the direct x-ray beam. These devices are clumsy and still force the operator to be too close to the radiation.

During percutaneous radiotherapy procedures radioactive seeds or probes are inserted into the patient. These are dangerous to have close to the operator. Other potential uses are to integrate robots with image guidance, including multimodality integration, and the integration of tracking technologies such as optical or mechanical trackers. The robots can perform active guidance in procedures where path planning and execution are difficult or provide a zone of constraint to keep the operator out of dangerous areas. A robot can also be integrated with active control to compensate for motion such as respiration. By compensating for patient motion the target can be made to appear static.

To be accepted in clinical practice, however, a robot must be intuitive and require minimal operator training. It must also be quick and easy to setup and not significantly increase the length of procedures. Robot must also be cost effective. The possibility of performing procedures that the human cannot perform and are clinically necessary remains an ultimate goal for medical robotics. Engineers and physicians should work together to create and validate these systems for the benefits of patients everywhere.

5   Acknowledgements

6   References

1.	Craig JJ. Introduction to Robotics. 2nd ed: Addison-Wesley; 1989.
2.	Kwoh YS, Hou J, Jonckheere EA, Hayati S. A robot with improved absolute positioning accuracy for CT guided stereotactic brain surgery. IEEE Transactions on Biomedical Engineering 1988;35(2):153-160.
3.	Davies B. A review of robotics in surgery. Proc Inst Mech Eng [H] 2000;214:129-140.
4.	Cleary K, Nguyen C. State of the art in surgical robotics: clinical applications and technology challenges. Comput Aided Surg 2001;6(6):312-28.
5.	Taylor RH, Stoianovici D. Medical robotics in computer-integrated surgery. Robotics and Automation, IEEE Transactions on 2003;19(5):765-781.
6.	Pott PP, Scharf HP, Schwarz ML. Today's state of the art in surgical robotics. Comput Aided Surg 2005;10(2):101-32.
7.	Melzer A, Schurr MO, Kunert W, Buess G, Voges U, Meyer JU. Intelligent Surgical Instrument System ISIS. Concept and Preliminary experimental application of components and prototypes. Endoscopic Surgery and Allied Technologies, 1:165-170, 1993
 8.	Guthart GS, J. Kenneth Salisbury J. The intuitive telesurgery system: overview and application. In: IEEE International Conference on Robotics and Automation; 2000; 2000. p. 618-621.
9.	Adler JR, Jr., Murphy MJ, Chang SD, Hancock SL. Image-guided robotic radiosurgery. Neurosurgery 1999;44(6):1299-1306; discussion 1306-7.
10.	Stoianovici D, Cleary K, Patriciu A, Mazilu D, Stanimir A, Craciunoiu N, Watson V, Kavoussi LR. AcuBot: A Robot for Radiological Interventions. IEEE Transactions on Robotics and Automation 2003;19(5):926-30.
11.	Stoianovici D, Cadeddu JA, Demaree RD, Basile SA, Taylor RH, Whitcomb LL, Sharpe WN, Kavoussi LR. An efficient needle injection technique and radiological guidance method for percutaneous procedures. In: Troccaz J, Grimson E, editors. Computer Vision, Virtual Reality and Robotics in Medicine - Medical Robotics and Computer-Assisted Surgery (CVRMed-MRCAS'97); 1997 March, 1997; Grenoble, France: Springer-Verlag; 1997. p. 295-298.
12.	Stoianovici D, Whitcomb LL, Anderson JH, Taylor RH, Kavoussi LR. A modular surgical robotic system for image guided percutaneous procedures. In: Medical Image Computing and Computer-Assisted Intervention; 1998: Springer-Verlag; 1998. p. 404-410.
13.	Patriciu A, Solomon S, Kavoussi LR, Stoianovici D. Robotic Kidney and Spine Percutaneous Procedures Using a New Laser-Based CT Registration Method. In: Niessen W, Viergever MA, editors. Medical Image Computing and Computer-Assisted Intervention; 2001 October 14-17, 2001; Utrecht, Netherlands: Springer-Verlag; 2001. p. 249-258.
14.	Solomon SB, Patriciu A, Bohlman ME, Kavoussi LR, Stoianovici D. Robotically Driven Interventions: A Method of Using CT Fluoroscopy without Radiation Exposure to the Physician. Radiology 2002;225(1):277-82.
15.	Cleary K, Stoianovici D, Patriciu A, Mazilu D, Lindisch D, Watson V. Robotically assisted nerve and facet blocks: a cadaveric study. Academic Radiology 2002;9(7):821-5.
16.	Kronreif G, Fürst M, Kettenbach J, Figl M, Hanel R. Robotic guidance for percutaneous interventions. Advanced Robotics 2003;17(6):541-560.
17.	Kronreif G, Kettenbach J, Figl M, Kleiser L, Ptacek W, Fürst M. Evaluation of a robotic targeting device for interventional radiology. In: Computer Assisted Radiology and Surgery (CARS); 2004: Elsevier; 2004. p. 486-491.

18.   Kettenbach J, Kronreif G, Figl M, Furst M, Birkfellner W, Hanel R, Ptacek W, Bergmann H. Robot-assisted biopsy using computed tomography-guidance: initial results from in vitro tests. Invest Radiol 2005;40(4):219-28.

19.   Kettenbach J, Kronreif G, Figl M, Furst M, Birkfellner W, Hanel R, Bergmann H. Robot-assisted biopsy using ultrasound guidance: initial results from in vitro tests. Eur Radiol 2005;15(4):765-71.

20.   Korb W, Kornfeld M, Birkfellner W, Boesecke R, Figl M, Fuerst M, Kettenbach J, Vogler A, Hassfeld S, Kronreif G. Risk analysis and safety assessment in surgical robotics: A case study on a biopsy robot. Minimally Invasive Therapy & Allied Technologies 2005;14(1):23 - 31.

21.   Melzer A, Seibel R. MR guided therapy of spinal disease. Minimally Invasive Therapy & Allied Technologies 1999(3):89-93.

22.   Gutmann B, Gumb L, Remmele T, Voges U, Fischer H, Melzer A. Principles of MR/CT Compatible Robotics for Image Guided Procedures. In: Radiology Suppl. 0032CEVI; 2002. p. 677.

23.   Bock M, Zimmerman H, Gutmann B, Melzer A, Fischer H, Semmler W. Combination of a Fully MR-compatible Robotical Assistance System for Closed-bore High-field MRI Scanners with Active Device Tracking and Automated Image Slice Positioning. In: Radiological Society of North America Scientific Program, Supplement to Radiology; 2004; p. 398.

24.   Stoianovici D, Patriciu A, Mazilu D, Petrisor D, Muntener M, Kavoussi L. Multi-Imager Compatible Robot for Transperineal Percutaneous Prostate Access. IEEE Transactions on Robotics 2005: submitted.

25.   Stoianovici D, Patriciu A, Mazilu D, Petrisor D, Kavoussi L. Pneumatic Step Motor. IEEE/ASME Transactions on Mechatronics 2005: submitted.

26.   Stoianovici D. Multi-Imager Compatible Actuation Principles in Surgical Robotics. International Journal of Medical Robotics and Computer Assisted Surgery 2005;1(2):86-100.

8.4 Roderick 2005: An Approach to Designing Software …

Reprint begins on the next page and is six pages.

WeD01-04

An Approach to Designing Software Safety Systems for Rehabilitation Robots

Stephen N. Roderick, Craig R. Carignan, *Member, IEEE*

Abstract— **This paper presents a system-level approach to the design of a safety-critical robotic system that is sufficiently safe to satisfy human-subject safety criteria. This system design approach utilizes preliminary hazard analysis, and fault tree analysis, and was successfully applied to a dexterous space robot designed to fly on NASA's space shuttle. An application of this approach to a shoulder rehabilitation exoskeleton will be presented and shown to improve the safety of the overall system.**

I. INTRODUCTION

Safety has always been a paramount concern in robotic systems, particularly when there is a potential for humans to enter the robot's work environment. The situation is often avoided by surrounding the workspace of the robot with a detection device that removes power to the robot if someone or something approaches. Unfortunately, this strategy is obsolete when it comes to medical applications such as surgery and rehabilitation where the robot must interact with the patient directly.

In recent years, robots have made substantial in-roads in the medical field. Devices such as Da Vinci [1], CyberKnife [2], and the IM2 Robot [3], have provided researchers and doctors alike with capabilities not previously available. These additional capabilities have also brought with them the issue of individual patient safety. While the robot must enforce the safety of the patient as an object within its workspace, it must also be able to operate upon, or assist the patient, contrary to most robots that are not allowed to affect the reachable human in any manner. This dichotomy creates the need for a safety system that can allow the robot to interact with the patient, but also enforce all necessary safety precautions at the same time.

In perhaps no other application is patient safety more acute than for exoskeletons in which the human is basically encapsulated in a robotic device. The Maryland-Georgetown-Army (MGA) Exoskeleton, shown in Figure 1, is an arm exoskeleton designed to treat shoulder pathology in a collaborative project between Georgetown University and the University of Maryland. The robot has five degrees of freedom, powered by brushless DC motors through a harmonic drive train capable of exerting up to 92 N-m of

torque at the shoulder. Encoders mounted on the motors and a suite of force sensors at the shoulder, elbow and wrist provide input to the control system to realize desired rehabilitation protocols.

This basic system does not inherently address the needs of safety, as its design can only identify certain basic robotic failures. The electromechanical subsystems, the software subsystems and the control subsystem, all need to be examined to determine overall patient safety. This paper will detail an approach to generating a sufficiently safe system design for safety-critical rehabilitation applications. The safety system of the MGA Exoskeleton will be used as an illustrative example of this approach.

Previous approaches to safety system design will first be examined in Section II, and an existing approach based on the safety system for a dexterous space robot will be presented in Section III. An overview of the MGA arm and its control system in Section IV will be followed by an example application of this safety system approach in Section V. This section will also examine changes in the initial system design necessary to enforce safety.
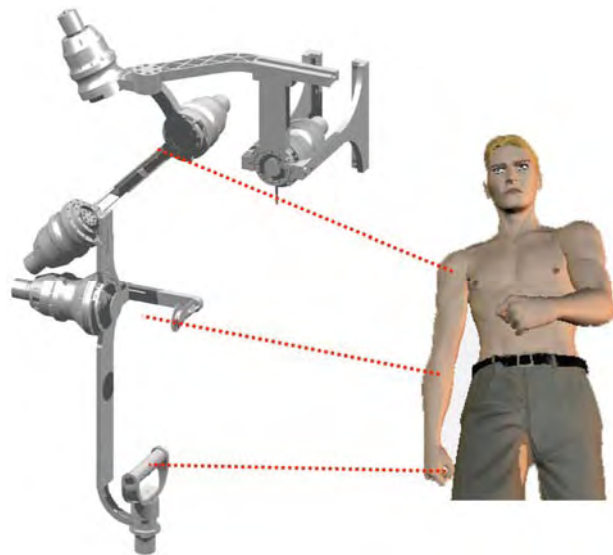

Figure 1 The MGA Exoskeleton designed for shoulder therapy.

S. N. Roderick is a research engineer with the Space Systems Laboratory, Department of Aerospace Engineering, University of Maryland, College Park, MD 20742 USA (e-mail: snrkiwi-ssl@yahoo.com).

C. R. Carignan, is a research associate with the Imaging Science and Information Systems Center, Department of Radiology, Georgetown University Medical Center, Washington, DC 20057 USA (e-mail: carignan@isis.imac.georgetown.edu).

II. PREVIOUS WORK

Previous medical robotics have had to address the issue of patient safety [4] [5]. One of the unique aspects of the medical robotic system presented here, is that the human in the loop is the patient. With surgical or radiological systems

252

such as Da Vinci [1] and Cyberknife [2], a patient is being "operated" on by the robot, however, a clinician is directing the robot. With the MGA system, the patient is both the individual upon whom the robot operates, and also the individual who directs the robot.

Unfortunately, given the infancy of this field, there is no industry-standard approach to designing these safety-critical robot systems [4] [5]. Numerous safety-critical software systems have been developed and deployed in other domains ranging from aircraft flight management systems [6] to nuclear power plants [7]. Analytical methods similar to that presented here are a standard and accepted practice in these domains, when identifying and characterizing the likelihood of hazards [8].

This paper presents an approach that was successfully applied to a space robot designed to fly on the NASA space shuttle [9]. This system was the first - and to date only - American robotic system to be certified through three of the four phases of the NASA Space Shuttle Safety Review process. It pioneered a solely computer-based hazard control system for payloads operating on the shuttle.

The following definitions are used in this paper [10]. A "failure" is an abnormal occurrence, while a "fault" is a higher-order event caused by one or more failures. A "hazard" is a system state and other environmental conditions that inevitably leads to an accident. An "accident" is an undesired and unplanned event that results in a level of loss, in this case, injury to the patient.

III. APPROACH

The process used to determine a sufficiently safe system design is shown in Figure 2. A basic system design that accomplishes the goals of the project is first examined as part of a Preliminary Hazard Analysis (PHA) [11]. A Fault Tree Analysis (FTA) [12] is then developed using the system design and the list of hazards generated by the PHA. The resulting fault trees can be qualitatively examined to determine if the system is "safe enough" for the project's purposes. If not, additional components are typically added to the system in an effort to deal with the specific safety issues raised by the FTA - the system design is modified accordingly - and the process starts again. Once the FTA results show that the project's safety criteria are met, the system design can be considered complete.

The concept of "safe enough" is one that the specific project must establish. It is not possible to make a system absolutely safe, however, if the likelihood of an accident is small enough or the consequences of an accident are negligible enough, the system may be considered safe enough [13] [14]. At some point, continuing to modify a system design to cope with ever more incredible failures simply results in an excessively complex design, and a subsequent reduction in overall system reliability and/or safety. In order to develop a safe system, it is first important to understand how the system is intended to function.
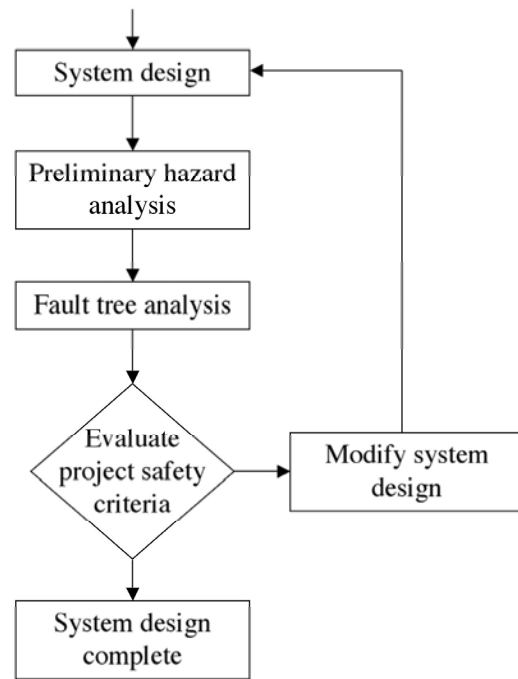

Figure 2 Approach to system design for safety.

IV. CONTROL SYSTEM

The MGA Exoskeleton has two operating modes: Virtual Reality (VR) Mode, and Physical Therapy (PT) Mode. In VR Mode, the forces exerted at the hand are controlled by interaction with a virtual environment generated by a computer. In PT Mode, the shoulder is exercised about an arbitrary axis through the glenohumeral (GH) joint using a preset resistance profile. In both cases, the scapula joint moves independently to "accommodate" shoulder elevation/depression. The two modes generate the need for contrasting control approaches which are described in more detail below [15].

A. Virtual Reality Mode

Virtual Reality Mode uses computer-generated environments to simulate daily living tasks for functional rehabilitation. The patient views the simulated task and representation of their arm through a head mounted display while the exoskeleton provides haptic feedback to the patient. A force sensor located at the hand gripper senses the forces being exerted by the patient's "contact" with the virtual environment and relays them to the controller, which moves the exoskeleton in response to the interaction.

The admittance controller shown in Figure 3 is used to convert sensed contact forces into motion commands [16] [17]. Signals from the gripper force-torque sensor and elbow load cells are input to the virtual environment, which then outputs a desired velocity for the wrist and angular rate of the shoulder-elbow-wrist (SEW) plane roll, ϕ. The desired velocities are then converted into desired joint velocities using the inverse Jacobian, which are then tracked using a proportional-derivative (PD) control law.
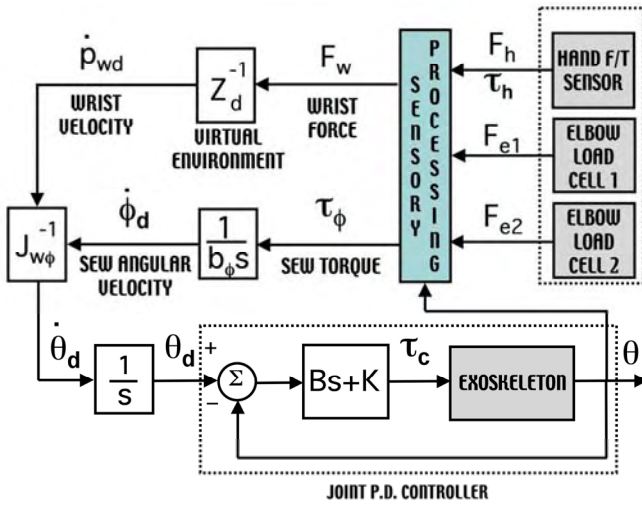
Figure 3 Admittance controller.

B. Physical Therapy Mode

Physical Therapy Mode is basically a programmable resistance trainer that allows the patient to exercise about an arbitrary shoulder rotation axis. For example, to treat rotator cuff injury, therapists often prescribe exercises involving lateral/medial rotation of the shoulder. Since there is no single joint corresponding to shoulder rotation, the exercise involves all three axes of the exoskeleton shoulder. Thus, the controller needs to affect a prescribed resistance profile about the desired axis while preventing rotations about the other shoulder axes.

Since there is no direct way to measure the torques about the shoulder joints, this mode uses an impedance controller with velocity inputs as shown in Figure 4 [18] [19]. In this scheme, the joint velocities are relayed to a Jacobian, J_{GH}, to compute the Cartesian velocities about the GH joint, ω_{GH}. These velocities are then multiplied by the desired resistance profile, which outputs the torques required about the GH axes, τ_{GH}. These torques are then converted into the exoskeleton joint torques using the Jacobian. A dynamic model of the exoskeleton runs in parallel to compute gravity and friction feedforward compensation torques. Since only the shoulder axes are constrained, the elbow pitch is left free to move however the patient desires.
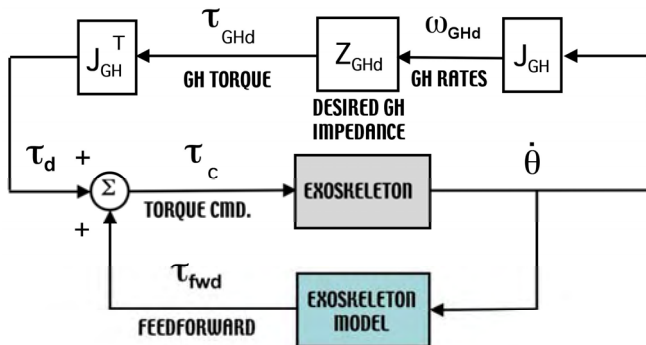

Figure 4 Impedance controller.

In both modes, the scapula joint is controlled independently from the arm joints. The objective is to keep the exoskeleton GH joint as closely aligned with the human GH joint as possible. The desired scapula angle ξ is determined using a biomechanical model of the scapula motion based on the motion of the GH joints. A tracking controller then drives the scapula joint to the desired angle. While only approximate tracking of the GH joint is possible using a single rotary joint, this scenario is preferable to the uncompensated motion observed in simulations of other powered orthoses such as MULOS [20].

The control system defines the minimum suite of sensors and actuators that are required to carry out operations, a partial diagram of which is shown in Figure 5. While this initial system design provides for operational capability, it must be further refined to ensure the patient's safety. The next section will detail an approach to refining a basic system design in order to ensure safety of the patient.
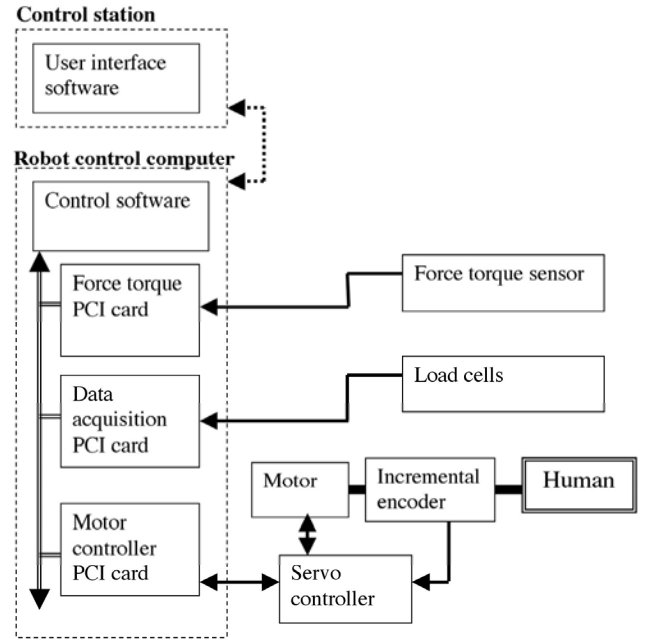

Figure 5 Initial system design. This is the minimum suite of sensors and actuators required for operations. For clarity, only major system components are shown.

V. SYSTEM SAFETY

A preliminary hazard analysis of the MGA system identified three potential hazards (in this context, "excessive" means an unhealthy level, leading to injury):

- Moving the patient outside their safe position range.
- Moving the patient at an excessive velocity.
- Applying excessive torque to the patient or, conversely, allowing the patient to apply excessive torque against the robot.

The project safety criteria specify that no single failure can cause a hazard, and that the system is "fail-safe". A fail-safe system is one that will achieve a safe state in the presence of a detected fault [9]. When a fault is detected, the system will

either a) halt arm motion and hold the current position, or b) safe the arm by removing power to the motors. Removing power has a more pronounced effect on the patient, as they now have to hold up the weight of the device. Thus, this approach is used only when more severe failures occur or when a reliable arm halt cannot be guaranteed. The state of the system, both patient and robotic, is safe for the patient if either a) or b) occurs.

The hazards identified by the PHA each constitute "top events" from which FTA can begin. Each top event is considered individually, and the immediate, necessary, and sufficient causes by which this event could occur are identified. These immediate events will summarily be examined for their causing events, and this step by step analysis continues until individual component failures are reached. These component failures are the basic causes that, when combined in the manner indicated by the fault tree, guarantee that the top level hazard will occur. The symbols used in this work to represent fault tree events and gates are shown in Figure 6. Further details of fault trees and their construction can be found in [12].
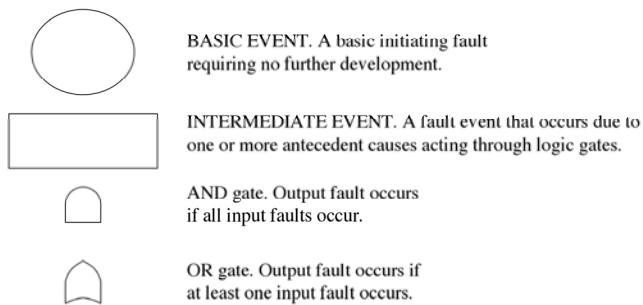

Figure 6 Symbols used in fault trees.

A. Moving the patient outside their safe position range

A fault tree developed from the initial system design of Figure 5, and the top event "Moving the patient outside their safe position range", is shown in Figure 7. This partial fault tree provides an example in which a single fault could cause this hazard. The top event can be caused by any one of numerous possible intermediate events, due to the OR gate attached to the top event. The intermediate event shown, "Uncommanded motion due to joint runaway", can be caused solely by a failure of the incremental encoder, which is a primary component of the control law used to drive the motor.

This scenario fails the project safety criteria, and so additional components were added to the system and the PHA and FTA were repeated. The modified system design is shown in Figure 8, where the shaded components, an absolute encoder and a power amplifier, are additions over the initial system design. Note that for clarity, additional safety components such as emergency stop measures are not shown.
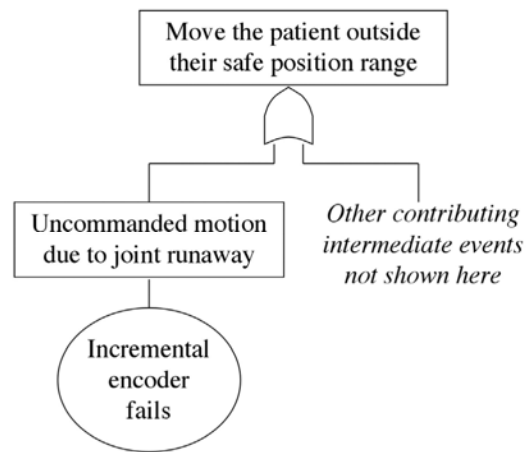

Figure 7 Fault tree for the initial system design and the top event "Moving the patient outside their safe position range". This fault tree shows that a single fault, that of the incremental encoder, could cause the top event to occur.

The fault tree for this top event and the modified system design is shown in Figure 9. This fault tree considers the addition of a second encoder and a software-based divergence check to the system design. The divergence check is designed to detect a failed encoder by comparing the values of the two encoders, and flagging a fault if they differ by more than a prescribed tolerance. This fault tree demonstrates that the addition of the second encoder and the encoder divergence check will satisfy the project safety criteria for this hazard: no one fault is capable of producing the hazard.
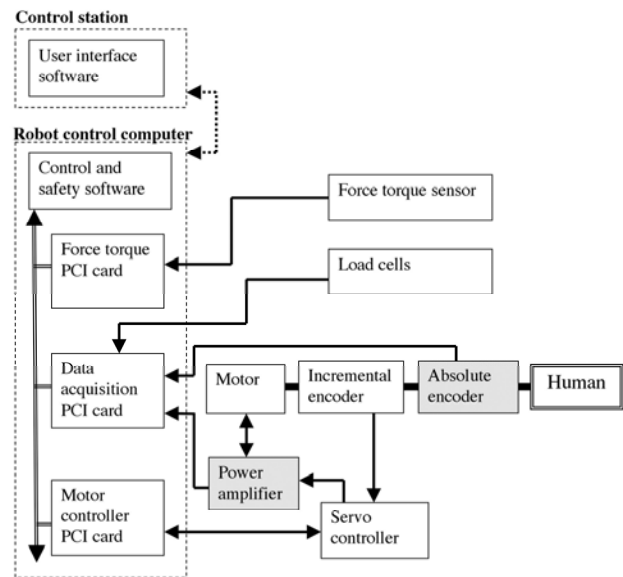
Figure 8 Modified system design with additional components to satisfy project safety criteria. The additions over the initial system design of Figure 5 are shaded. For clarity, only major system components of relevance are shown.

While the modified system design does prevent a single failure from causing this hazard, closer examination of Figure 9 shows that a double failure could still cause the hazard. If both encoders fail in such a way that they output

almost the identical same value they would pass the encoder divergence check. While this failure combination is possible, particularly for certain values (depending on the encoders construction, 0 or -1 are likely candidates), it is highly unlikely to occur at the same time, and thus could be deemed an "incredible" failure and removed from further analysis. While further modifications to the system design, such as a third encoder, may enable detection of such situations, the additional system complexity may be unwarranted as well as potentially contributing to lower system reliability. The tradeoff between these measures is beyond the scope of this paper.
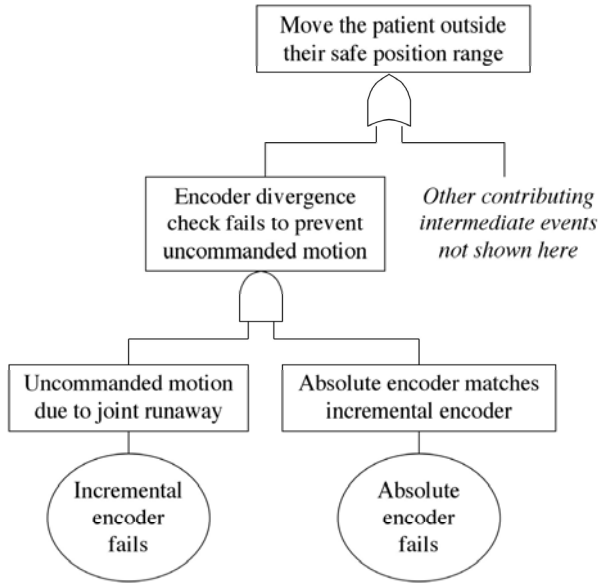

Figure 9 Fault tree for the modified system design and the top event "Moving the patient outside their safe position range". This fault tree indicates that two simultaneous faults are required for the intermediate event shown to cause the top event to occur.

To help determine the overall likelihood of such incredible failures occurring, the fault trees may be quantitatively evaluated. It must be noted, however, that FTA is more a qualitative technique, and that "its absolute accuracy is generally secondary to identification of failure sequences" [21]. Quantitative analysis may therefore be beneficial in simply ranking failures by probabilistic likelihood, versus using the output probabilities as absolute indications of safety [10].

B. Moving the patient at an excessive velocity

The fault trees for this hazard are very similar in structure to those for the previous hazard. This is primarily due to the system computing velocity based on sequential encoder readings, and hence there are identical measures to sense excessive velocity or to detect a failed component that contributes to velocity sensing. Thus, this hazard is not considered further here.

C. Applying excessive torque to the patient

A fault tree for the initial system design and the top event, "Applying excessive torque to the patient", is shown in Figure 10. A single fault of the servo controller, which is responsible for providing power to the motor, is capable of producing uncommanded motion and hence, potentially, applying excessive torque to the patient. The fault tree of Figure 11 is for the modified system design, and shows the addition of a separate power amplifier with built-in motor current sensor, and a software-based motor power check. This power check compares the motor current draw with the requested output of the servo controller, to determine if either component is at fault. This fault tree indicates that the project safety criteria are satisfied by these additions.

Figure 10 Fault tree for the initial system design and the top event "Applying excessive torque to the patient". This fault tree shows that a single fault, that of the servo controller, could cause the top event to occur.

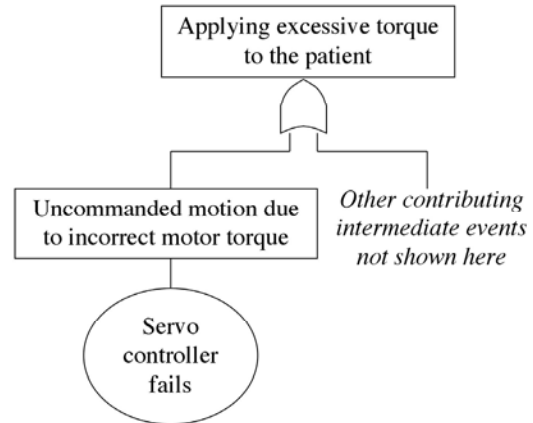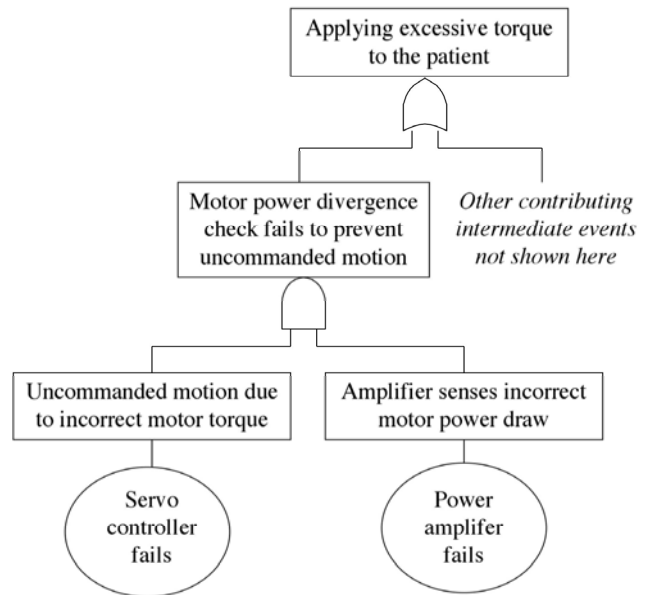**Figure 11 Fault tree for the modified system design and the top event "Applying excessive torque to the patient". This fault tree indicates that two simultaneous faults are required for the intermediate event shown to cause the top event to occur.**

VI. Conclusion

The methodology presented here allows system designers to produce an overall system design that is sufficiently safe to satisfy the project's safety criteria. This approach will often result in additional components being added to a system, to ensure that the safety system can detect failures and act accordingly.

The safety system for the MGA Exoskeleton consists of a suite of interwoven hardware constraints and devices (e.g. secondary encoders, slip clutch), electronic checks (e.g. encoder illegal states), and software checks (e.g. encoder divergence checks, electronic component heartbeats). The system design to date satisfies the project safety criteria, and indeed, carries over much of the safety approach and design elements from its space flight predecessor.

Acknowledgment

References

[1] G. Guthart, J. Kenneth Salisbury Jr, "The intuitive telesurgery system: Overview and application", in Proceedings of the 2000 IEEE International Conference on Robotics and Automation, San Fransisco, CA, 2000, pp 618-622.

[2] Accuray, http://www.accuray.com/

[3] Interactive Motion Technologies, http://interactive-motion.com

[4] P. Varley, "Techniques for Development of Safety-Related Software for Surgical Robots", Information Technology in Biomedicine, IEEE Transactions on, Volume 3, Issue 4, Dec. 1999, pp 261-267

[5] R.H.Taylor, H.A. Paul, P. Kazanzides, B.D. Mittelstadt, W. Hanson, j. Zuhars, B. Williamson, B. Musits, E. Glassman, W.L. Bargar, "Taming the Bull: Safety in a Precise Surgical Robot", in *Robots in Unstructured Environments*, Fifth International Conference on Advanced Robotics, volume 1, 19-22 June 1991, pp 865-870.

[6] D. L. Parnas, G. K. Asmis, and J. Madey, "Assessment of Safety-Critical Software in Nuclear Power Plants," *Nuclear Safety,* 32(2), pp. 189-198, 1991.

[7] J. Potocki de Montalk, "Computer Software in Civil Aircraft," *Microprocessors & Microsystems,* 17(1), pp. 17-23, 1993.

[8] W. Weber, H. Tondok, and M. Bachmayer, "Enhancing Software Safety by Fault Trees: Experiences from an Application to Flight Critical SW," *Proceedings of 22nd International Conference on Computer Safety, Reliability and Security*, Edinburgh, Scotland, 23-26 September, 2003.

[9] S. Roderick, B. Roberts, E. Atkins, P. Churchill, D. Akin, "An Autonomous Software Safety System for a Dexterous Space Robot", Journal of Aerospace Computing, Information, and Communication, AIAA, December 2004.

[10] S. Roderick, "Validation of a Computer-Based Hazard Control System for a Robotic Payload on the Space Shuttle", M.S. Thesis, Department of Aerospace Engineering, University of Maryland, College Park, MD 20742, USA.

[11] N.G. Leveson, "Safeware: System Safety and Computers", Addison-Wesley, 1995.

[12] W.G. Vesely, "Fault Tree Handbook", US Nuclear Regulatory Commission, 1981.

[13] T. Anderson, "Safety – Status and Perspectives", in *Proceedings of the 12th International Conference on Computer Safety, Reliability, and Security*, Poznan-Kierkz, Poland, 27-29 October 1993.

[14] R. Shaw, "Safety cases – How Did We Get Here?", in *Safety and Reliability of Software-Based Systems*, 12th Annual CSR Workshop, Bruges, 12-15 September 1995.

[15] C. Carignan, K. Cleary: Closed-Loop Force Control for Haptic Simulation of Virtual Environments, Haptics-e, The Electronic Journal of Haptics Research (http://www.haptics-e.org), Vol. 2, No. 2, 1-14, Feb. 2000

[16] J. Maples, and J. Becker, "Experiments in Force Control of Robotic Manipulators", *Proceedings IEEE Intl. Conf. on Robotics and Automation*, April 1986

[17] C. Carignan, D. Akin: Achieving Impedance Objectives in Robot Teleoperation, *Proceedings IEEE Int. Conf. on Robotics and Automation*, Albuquerque, 3487-3492, Apr. 1997

[18] N. Hogan, "Impedance Control: An Approach to Manipulation", Journal of Dynamic Systems, Measurement, and Control, Vol. 108, March 1985

[19] T. Massie and J.K. Salisbury, "The PHANToM Haptic Interface: A Device for Probing Virtual Objects", *Proceedings ASME Winter Annual Meeting: Symposium on Haptic Interfaces for Virtual Environment and Teleoperator Systems*, Nov. 1994

[20] M. Buckley, and R. Johnson, "Computer Simulation of the Dynamics of a Human Arm and Orthosis Linkage Mechanism", Proc. Instn. Mech. Engrs. Part H, Vo. 211, pp. 349-357, 1997

[21] H. Ozog and L.M. Bendixen "Hazards Identification and Quantification", Hazard Prevention, Sept/Oct 1987, pp 6-13.

257

8.5 Siddoway 2006: Workflow in Interventional Radiology …

Reprint begins on the next page and is eight pages.

Workflow in Interventional Radiology: Nerve Blocks and Facet Blocks

Donald Siddoway[a], Mary Lou Ingeholm[a], Oliver Burgert[b],
Thomas Neumuth[b], Vance Watson[a], Kevin Cleary[*a],

[a]Imaging Science and Information Systems (ISIS) Center, Department of Radiology
Georgetown University, 2115 Wisconsin Ave. NW, Suite 603, Washington, DC 20007
[b]University of Leipzig, Innovation Center Computer Assisted Surgery (ICCAS), Philipp-Rosenthal-Str. 55, D-04103, Leipzig, Germany

ABSTRACT

Workflow analysis has the potential to dramatically improve the efficiency and clinical outcomes of medical procedures. In this study, we recorded the workflow for nerve block and facet block procedures in the interventional radiology suite at Georgetown University Hospital in Washington, DC, USA. We employed a custom client/server software architecture developed by the Innovation Center for Computer Assisted Surgery (ICCAS) at the University of Leipzig, Germany. This software runs in an internet browser, and allows the user to record the actions taken by the physician during a procedure. The data recorded during the procedure is stored as an XML document, which can then be further processed. We have successfully gathered data on a number if cases using a tablet PC, and these preliminary results show the feasibility of using this software in an interventional radiology setting. We are currently accruing additional cases and when more data has been collected we will analyze the workflow of these procedures to look for inefficiencies and potential improvements.

Keywords: Surgical Workflow, Workflow Management Tools, Workflow Optimization, Surgical PACS

1. INTRODUCTION

The ability to systems engineer clinical environments in terms of formal workflow descriptions of processes and procedures has significant implications. Workflow analysis has the potential to dramatically improve the efficiency and clinical outcomes of medical procedures. From an operations standpoint, it allows inefficiencies to be identified and remedied more quickly. From a technology perspective, it enables a methodical and scientific approach to the specification, simulation, design and prototyping of new technology, allowing development to occur more efficiently.[1,2] In either case, it allows the impact of a new strategy to be assessed objectively.

The application of workflow analysis to the clinical environment is only beginning to emerge and is likely to gain more interest in the upcoming years. Significant workflow analysis research is currently being done by the Innovation Center for Computer Assisted Surgery (ICCAS) in the area of surgical interventions as the basis for the development of computer assisted surgery (CAS) systems.[1,2,3] ICCAS has focused its efforts on modeling surgical workflows by recording data from real world surgical interventions that can be associated with well-defined task of the intervention with high granularity. The development of a computerized workflow editor tool to record workflow data is crucial to the capability of the recorder to capture fine-grained data. The tool draws upon ontologies developed for different surgical disciplines and also includes a visualization tool to analyze the data.

Interventional Radiology (IR) can benefit from a similar effort. IR is an image-guided therapy, and can take advantage of any and all imaging modalities, and accompanying computer and mechanical enhancements. The capability to model IR procedures will allow new technologies to be developed and evaluated more quickly. Additionally, the boundaries between IR and surgery are blurring. While IR procedures include increasingly more invasive therapeutics, such as tumor ablation, surgeons are adopting the techniques and principles of IR, and are relying more heavily on intra-operative imaging. Thus, it is timely to apply the workflow analysis approach developed for surgical interventions to IR procedures.

In this study, the ICCAS workflow tool is adapted to the specific requirements of IR workflow. It is then used to record workflow data for nerve block and facet block procedures in the IR suite at Georgetown University Hospital in Washington, DC. The intent of the study is to determine the feasibility of recording workflows in an IR setting and to analyze the workflow of these procedures, identify inefficiencies, and potentially improve the efficiency of these procedures. This paper describes the development, of an IR-specific workflow tool and the results of using it to record workflow in an IR setting.

2. METHODS

We recorded workflows using a software package developed at ICCAS that facilitates the structured recording of surgical workflows. The ICCAS software uses a workflow editor to support the difficult process of dealing with the complex relationships and concurrencies that occur during surgical interventions. It then generates a structured description of the intervention in XML format that can be used for visualization and further analysis. Although the software was developed to record surgical workflow, its design makes it easy to adapt to other disciplines by changing the underlying ontology.[2] Since IR workflow had not been previously recorded, the approach was to first start with a simple procedure that is performed with some frequency. Nerve and facet block procedures were selected since they fit the outlined criteria. In this way, the ontology could be developed and integrated with the workflow application. Actual recording could then be conducted with enough frequency to provide an understanding of the feasibility of recording workflow data in the IR setting.

2.1 Developing the interventional radiology (IR) ontology
Although commonalities exist between IR procedures and surgical interventions, there are significant enough differences that the ICCAS tool must be modified to support IR. Therefore, the first step was to generate the appropriate ontology for IR workflow of nerve block and facet block procedures. After a thorough analysis through observation of multiple nerve and facet blocks procedures, the procedures were broken down into specific tasks each comprised of four components (1) participants involved (2) actions performed (3) instruments used and (4) anatomic structures treated. By combining the components across all identified tasks in a block procedure, comprehensive lists for each component were generated (See Figure 1). Each task executed during a procedure is defined as a combination of items from each of these

Participants Involved

- operator (physician)

Actions Performed

- acquire image
- place
- insert
- remove
- insert syringe
- adjust angle and advance
- inject
- mix drugs

Instruments Used

- local anesthesia needle
- syringe
- local anesthesia needle with syringe
- block needle
- fluoroscopy

Anatomic Structures Treated

Nerve Blocks
- C1,C2,C3,C4,C5,C6,C7,C8
- T1,T2,T3,T4,T5,T6,T7,T8,T9,T10,T11,T12
- L1,L2,L3,L4,L5

Facet Blocks
-C1-2,C3-4,C5-6,C7-8
-T1-2,T3-4,T5-6,T7-8,T9-10,T11-12,T12-L1
-L1-2,L3-4,L5-S1

Side
-right
-left
-right/left

Spine Levels
C=Cervical
T=Thoracic
L=Lumbar
S=Sacral

Figure 1 – Specific ontology developed for IR

lists. Once the lists were completed, ICCAS incorporated the IR ontology into the workflow editor. The resulting interface is shown in Figure 2.

Figure 2 - ICCAS workflow editor modified to support IR nerve and facet block procedures

2.2 Technology description

For this study, we chose to run the software on a Tablet PC, which is portable and has a touch screen display for easy data entry. The workflow editor is run as a web application. It is programmed in Hypertext Preprocessor (PHP) which supports the development of web-based software applications. We used XAMPP, an easily installable and configurable Apache (A) distribution with combined MySQL (M), Perl (P) and PHP (P) support. The X stands for different distributions for Linux, MacOS and Windows.[4] We installed it on the PC in order to simplify the architecture and hardware requirements. For recording multiple workflows on multiple clients, a dedicated server and wireless network could be utilized. Pointing the Mozilla Firefox web browser to the PHP pages launches the application.

2.3 Workflow recording

Before recording can begin, the user must first collect data about the procedure. The workflow editor prompts the user to enter information about the recording person (user), location of the procedure, discipline, diagnosis, therapy, participants, and patient. Once this information has been entered, recording is initiated by selecting the 'Start' button to signify the start of the procedure. During the block procedure, the user selects the 'Start New Activity' button to indicate when a new task is beginning. The software records this timestamp as the start time of the task. The user then uses the graphical user interface (GUI) to select the items from each list that define the task, namely the participant (e.g. surgeon), action performed, the instrument used, and the anatomic structure involved. Once the participant has completed the action, the user selects the 'Stop' button and the software records this time as the stop time. This sequence is repeated for each task of the block procedure. Some procedures may involve multiple tasks occurring concurrently. The workflow editor handles this situation by providing a timeline of tasks on the screen. If a new task starts before the previous task ends,

the user simply selects the 'Start New Activity' button without stopping the previous task. The user may then use the timeline to access and signal completion of previous tasks.

When the block procedure ends and recording is completed, the user selects the 'Save' button. The workflow editor creates an XML file consisting of a header and a body that contains all of the recorded data. The header contains the contextual data about the procedure that was entered before the start of the procedure.[1] It includes the following data elements:

(a) the *discipline* with the child elements
 (a1) *diagnosis*
 (a2) *therapy*
 (a3) *participant* with the elements position (e.g. interventionalist, technologist, nurse) and a note field
 (a4) a *note* field for discipline related information
(b) the *date of recording*,
(c) the *place of recording*, with the child elements
 (c1) *country*
 (c2) *city*
 (c3) *hospital*
 (c4) *operating theatre*
 (c5) a *note* field for recording place related information
(d) the *recording person* with the child elements
 (d1) *first name*
 (d2) *last name*
 (d3) *status* (e.g. medical student, recording experience)
 (d4) a *note* field for recording person related information
(e) an input field for *notes* regarding the whole intervention.

In the body of the XML file, the data are partitioned into *tasks* that represent the work steps of the IR procedure.[1] Each task has the following structure:

(a) the *tasktime* with the child elements
 • *start time*
 • *stop time*
 • *duration*
(b) an *actuator* that
 • has the same *position* as indicated by the *participant* element inside *discipline* (e.g. interventionalist, technologist, nurse) and a note field
 • a *note* field for participant related information
 • an element that indicates various *used body parts* (in regarding of granularity level (ii) or (iii)), such as 'left hand', 'right hand'. The consideration of other parts of the body like 'right foot' for the operation of foot pedals or 'gaze' for the gathering of information from monitors is also possible.
(c) the accomplished *activity*,
(d) the *instrument* used in the work step,
(e) the treated *anatomic structure*,
(f) an input field for *notes*

Figure 3a and 3b illustrate the XML file The XML data can also be transformed into a two-dimensional Scalable Vector Graphic (SVG) for semantic analysis of the single workflow activities.[3] It allows the workflow to be generalized and analyzed, allowing suggestions to be made to improve the efficiency of the procedure.

```
<rec_workflow workflowID="wf1132676025687.2">
     <discipline discipline="Interventional Radiology">
          <diagnosis>pain</diagnosis>
          <therapy>nerve block</therapy>
          <participant>
                    <position>operator</position>
                    <name>Dr. E. Nostaw</name>
                    <note></note>
          </participant>
          <patient>
                    <age>84</age>
                    <sex>m</sex>
                    <position>prone</position>
                    <note></note>
          </patient>
          <note></note>
     </discipline>
     <rec_date>2005-11-22</rec_date>
     <rec_location>
          <country>USA</country>
          <city>Washington, DC</city>
          <institution>Georgetown Univ Hospital</institution>
          <building>CCC</building>
          <operatingtheatre>IR Room 6</operatingtheatre>
          <note></note>
     </rec_location>
     <rec_by>
          <name>Donald Siddoway</name>
          <status>medical student</status>
          <note></note>
     </rec_by>
```

```
<task taskID="1">
     <tasktime>
          <starttime>1122395258.1117</starttime>
          <stoptime>1122395261.2262</stoptime>
          <duration>3.1144998073578</duration>
     </tasktime>
     <actuator>
          <position>operator</position>
          <usedbodypart>operator</usedbodypart>
     </actuator>
     <activity>
          <action>place</action>
     </activity>
     <instrument>
          <usedinstrument>pointer</usedinstrument>
     </instrument>
     <anatomic_structure>
          <treatedStructure>
                    <structure>Nerve</structure>
                    <level>L3</level>
                    <side>Left</side>
          </treatedStructure>
     </anatomic_structure>
</task>
```

Figure 3a –Header component of
XML file for IR workflow

Figure 3a –Body component of
XML file for IR workflow

3. RESULTS

3.1 Workflow results

IR workflow was recorded for 7 nerve block procedures and 1 facet block procedure (Table 1). Analysis indicates that the tasks are short in duration and that the idle time between tasks is very short. The workflow editor successfully generated the appropriate XML files. These data files provide a thorough record of all the actions taken by the interventional radiologist during block procedures. Figure 4 shows a sample of an XML workflow file with the accompanying SVG representation. These can then be analyzed in order to assess the efficiency of the procedure, both on the basis of the individual case, and for the procedure in general.

3.2 Usability of the workflow editor in IR

The tablet PC is a good choice for recording workflow because it offers access to an external keyboard and a touch screen. Having access to a keyboard makes it easy to enter text data about the procedure while the tablet mode is better suited for the workflow recording - it is easier to hold in the procedure room, and the touch screen display eliminates the need for a mouse and keyboard. With respect to recording the workflow of block procedures, we found that the high level of granularity defined for the workflow editor combined with the very rapid pace of the block procedures made workflows difficult to record. In general, the tasks were very short in duration and the idle time between tasks was even shorter making it difficult for the recording person to accurately capture the end of one task and the start of a new one. It became particularly difficult when several short-duration tasks occurred sequentially. For example, when positioning the

needle, the steps of adjusting the needle and taking an X-ray image alternate until the needle is properly positioned. Neither of these steps takes very long and the idle time between them is short. It was not always possible to capture the task accurately or at all, thereby, decreasing the reliability of the data.

Procedure	Type	Number of tasks/procedure	Total time/procedure (seconds)	Mean duration time/task (seconds)	Mean idle time/task (seconds)
Workflow1	nerve	31	342.0	7.7	3.3
Workflow2	nerve	31	414.0	9.1	3.2
Workflow3	nerve	21	240.0	3.8	3.1
Workflow4	facet	10	192.0	15.1	4.0
Workflow5	nerve	25	453.0	13.4	3.5
Workflow6	nerve	24	257.0	7.9	2.8
Workflow7	nerve	10	245.0	17.8	6.6
Workflow8	nerve	21	265.0	8.1	4.9
Mean		21.6	301.0	10.4	3.9

Table 1 - IR workflow for eight procedures

The GUI itself exacerbated the issue because for each new task, the recording person must select a minimum of four buttons. Sometimes the task would be completed before all selections could be completed. There were also some problems adapting the software to our particular recording devices. Most notably, the GUI did not fit on the screen, so some scrolling was required to press some of the buttons. This further slowed the recording process. Some modifications were made to the GUI to allow for quicker recording. One such optimization involved the selection of the involved anatomic structure. For block procedures, the anatomic structure changes only once or not at all. To address this issue, the software was changed so that when an anatomic structure was selected, it would remain selected throughout the procedure.

4. DISCUSSION

As a proof of concept, this study has been successful in demonstrating the feasibility of recording workflow in IR and in providing important lessons learned that will be critical to improving subsequent workflow studies. This block procedure workflow study has established that the process of recording workflow in IR is feasible. The ICCAS workflow editor was able to be adapted to IR workflow, resulting in the appropriate XML data files and accompanying SVG graphical representations. Recording was not disruptive to the any aspect of the block procedure itself and from an ergonomic perspective the tablet PC was a good match for recording workflow.

The primary lesson learned was that the physical act of recording must be able to support the selected granularity of the procedure. It is critical to balance the type of procedure, the granularity of described tasks within the procedure and the interface to the workflow editor. The block procedures were selected because they represent straightforward procedures with very little concurrent tasks and they are performed weekly at Georgetown University Hospital. The basis for this choice was that it would allow rapid development of the necessary ontology and that recording could be conducted regularly, providing data for workflow analysis. The problem encountered is that in setting up the ontology, we chose a description of high granularity. We did not recognize that the rapid pace of the procedure coupled with such a detailed description would cause difficulty in accurately recording the procedure. Future studies must take this into account whether it means modifications to the recording interface or changing the granularity of the procedure description

For this study specifically, some of the issues can be remedied. The ontology can be collapsed where commonly used steps occur in a specific sequence extending the duration time. It is also possible to combine several commonly used steps in the ontology into fewer button presses. It may also be possible to integrate voice commands, rather than button

pushes, to allow for quicker recording and to allow the person using the workflow editor to always watch the procedure. Video recordings could also be used to validate workflow data and make corrections where necessary.


```
<task taskID="19">
    <tasktime>
        <starttime>1122394250.5829</starttime>
        <stoptime>1122394255.7404</stoptime>
        <duration>5.1575002670288</duration>
    </tasktime>
    <actuator>
        <position>operator</position>
        <usedbodypart>operator</usedbodypart>
    </actuator>
    <activity>
        <action>acquire image</action>
    </activity>
    <instrument>
        <usedinstrument>fluoro</usedinstrument>
    </instrument>
    <anatomic_structure>
        <treatedStructure>
        <structure>Nerve</structure>
        <level>L4</level>
        <side>Left</side>
        </treatedStructure>
    </anatomic_structure>
</task>
<task taskID="20">
    <tasktime>
        <starttime>1122394256.7118</starttime>
        <stoptime>1122394261.9593</stoptime>
        <duration>5.2474999427795</duration>
    </tasktime>
```
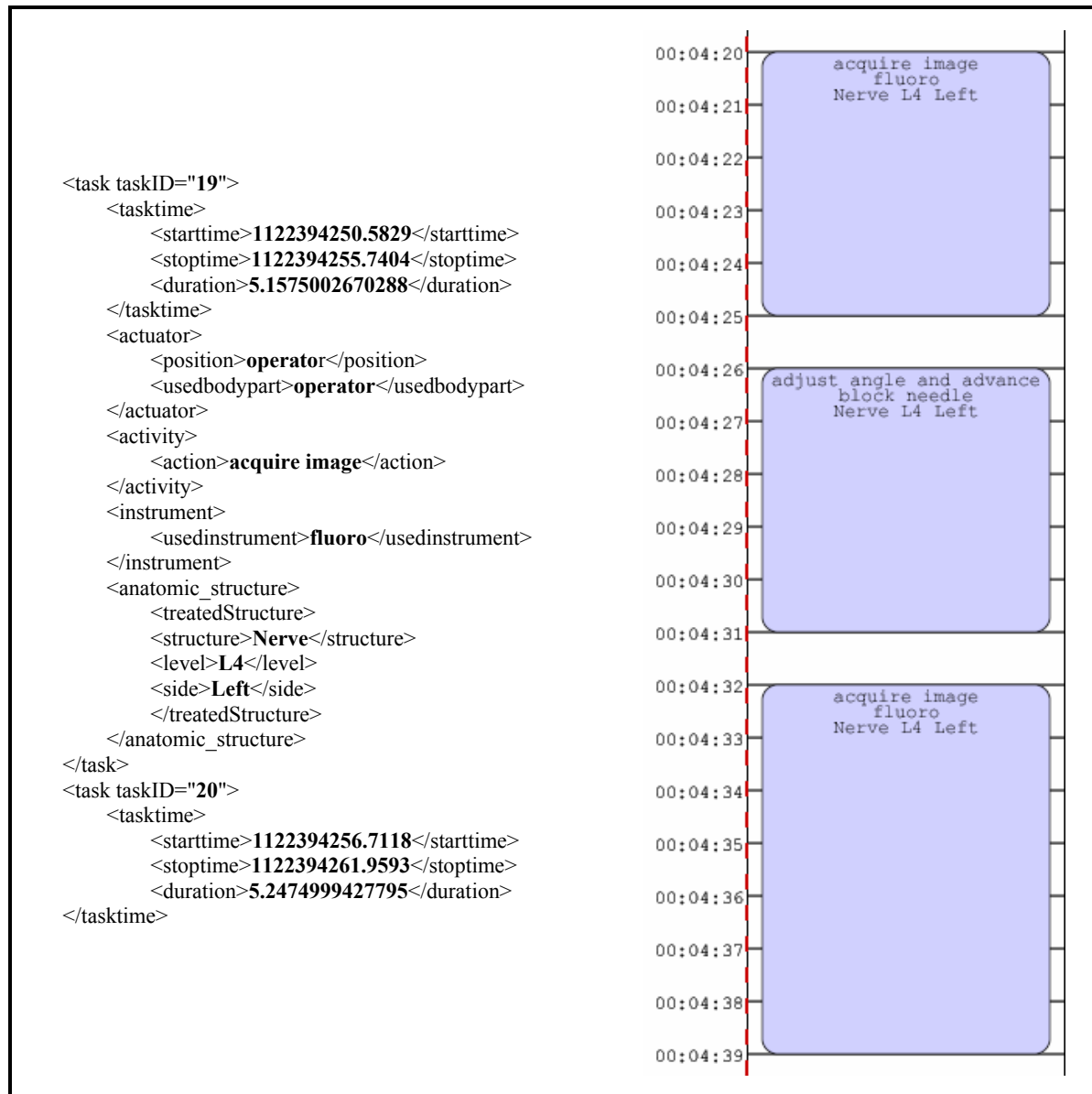
Figure 4 – Text on the left represents recorded data for tasks 19-20 in a typical case with the corresponding SVG representation on the right. Each blue blocks represents a task with the top of block indicating the start time and the bottom of the block indicating the stop time (the height of the block is the duration). The time between blocks represents idle time. The SVG representation allows one to quickly visualize the workflow.

5. CONCLUSION

Workflow recording and analysis in IR is a work-in-progress. It has the potential to be a valuable tool in creating formal descriptions of IR procedures that can then be used to evaluate new diagnostic and therapeutic strategies, and launch the development of new devices or image-guided systems (e.g. using a telemanipulator compared to manual intervention).

Workflow is also at the foundation of integrating IR with other clinical services using the Integrated Health Enterprise (IHE) approach and standards development such as Digital Imaging and Communications in Medicine (DICOM).[5,6] The intent is to refine the work done on block procedures by modifying granularity of the procedure description and further improve the workflow editor GUI to enable more accurate recording. The next step will be to incorporate more IR procedures into the workflow editor and begin collecting data on those procedures.

Although this study was limited to workflow recording of the procedure itself, workflow recordings could also provide additional benefit by expanding the scope beyond the actual procedure. Following the flow of patient along with the flow of the procedure is a critical component to creating a greater efficiency not only in the procedure room, but also in the perioperative environment. Many of the inefficiencies found in hospitals today involve the flow of patients, which should be optimized so as to minimize the time physicians spend waiting for the next patient, and minimizing the time that patients spend waiting for the physician. Using workflow recording and analysis at the departmental level may aid in revealing inefficiencies and assessing strategies to overcome them.

ACKNOWLEDGEMENTS

REFERENCES

1. T. Neumuth, N. Durstewitz, M. Fischer, G. Strauß, A. Dietz, J. Meixensberger, P. Jannin, K. Cleary, H.U. Lemke, "Structured Recording of Intraoperative Surgical Workflows", accepted for SPIE Medical Imaging 2006, PACS and Imaging Informatics.
2. O. Burgert, T. Neumuth, G. Strauß, C. Trantakis, V. Falk, H.U. Lemke, "Workflow-analysis of Surgical Interventions in ENT and Neurosurgery", in *Computer Aided Surgery around the Head - 3rd International Symposium Proceedings*, edited by S. Weber, F. Langlotz, J. Bier, T.C. Lueth, pp. 85 - 86., VDI Verlag, Düsseldorf 2005.
3. T. Neumuth, A. Pretschner, C. Trantakis, M. Fischer, H.U. Lemke O. Burgert, "An Approach to XML-based Description of Intraoperative Surgical Workflows", in *Berliner XML-Tage 2005*, edited by R. Eckstein, R. Tolksdorf, pp. 147-152, Berlin, 2005.
4. http://www.apachefriends.org/en
5. http://www.ihe.net
6. http://medical.nema.org

8.6 Tang 2005: Virtual Environment …

Reprint begins on the next page and is six pages.

IEEE Inter Conf on Rehabilitation Robotics

Proceedings of the 2005 IEEE
9th International Conference on Rehabilitation Robotics
June 28 – July 1, 2005, Chicago, IL, USA

ThP01-10

Virtual Environment for Robotic Tele-Rehabilitation

Jonathan Tang, Craig Carignan, Shailesh Gattewar

Abstract— Haptic and visual displays are combined to realize cooperative, force-feedback tasks over the internet. The operators "exert" forces on a virtual object which in turn generates a set of reaction forces to be displayed on the haptic devices. A novel cooperative control architecture based on wave variables is implemented to realize stable operation in the presence of time delays. The control scheme is validated experimentally for a manipulation task over the internet using a pair of InMotion2 robots. Preliminary results are also presented for 3D tasks rendered on a head-mounted display equipped with a head tracker for changing viewing angles.

I. INTRODUCTION

Robots have been explored as possible rehabilitation aids in laboratory settings for well over a decade. These investigations have recently expanded into the field of "teletherapy," whereby a clinician can interact with patients in remote locations over the internet. The focus of our research is to enable cooperative rehabilitative tasks in virtual environments intended to simulate active daily living tasks. The use of a "haptic" (force-feedback) device in conjunction with a video display will allow the clinician to remotely assess the patient's condition as well as assist the patient while performing rehabilitation tasks.

This article describes an architecture for cooperative rehabilitation over the internet using wave variables in a virtual environment. The article begins with a brief review of previous work on cooperative haptics and time-delay compensation. An example cooperative beam task is presented in Section V. A haptic/VR interface currently under development is described in Sections III and IV shown in Figure 1. The effects of internet time delay and a method to compensate for packet jitter is described in Section VII. Conclusions on the implementation of the cooperative rehabilitation environment are given in Section VIII along with some directions for future research.

II. PREVIOUS WORK

There have been several successful demonstrations of the use of force-feedback devices for rehabilitation. Researchers at the University of Reading have incorporated a three degree-of-freedom (DOF) Haptic Master in their prototype

system for stroke therapy [1]. The GENTLE/S is used as an orthosis to support the arm and has a haptic display for "reach-and-grasp" tasks inside a virtual room. The use of a haptic interface allows reach and grasp movements to be retrained by either assisting movement, or directing movement towards a specified target. The virtual environment is used to replicate the subject's viewpoint in the real world, where the background mats and shapes are used to help perception of movement and space.

Fig. 1. Top view of *InMotion^2* workstation showing four-bar linkage, direct drive motors, workstation, and flat panel display.

Cooperative control using haptic devices has been attempted on several virtual reality platforms. A pair of 2-DOF master manipulators was used by Harvard investigators to simulate thumb and index fingertip contact with an object during a peg-in-hole insertion task [2], [3]. Japanese researchers using a pair of 6-DOF PHANToM devices to simulate dual-arm contact with a steering wheel for arm motor control training [4]. A pair of 6-DOF, parallel mechanism force displays were used by researchers at the University of Tsukuba, Japan to perform interactive patient-therapist tasks over the internet [5]. Although predictive displays were used to help operators adjust for up to 3 sec delays, explicit time-delay compensation was not implemented. Several investigators have incorporated explicit time-delay compensation in the force-feedback loops of haptic systems. Wave variables were introduced by M.I.T. investigators for a variety of master/slave scenarios with widely varying time delay [6]. Passivity control was implemented by researchers at the University of Washington to enable stable interaction with virtual environments in the presence of time delay [7].

365

III. HARDWARE

The Imaging Science and Information Systems (ISIS) Center at Georgetown University Medical Center has recently assembled a robot rehabilitation testbed consisting of a pair of *InMotion² Shoulder-Elbow Robots* from Interactive Motion Technology, Inc. [8]. The *InMotion²* (IM2) Robot is a direct-drive, four-bar linkage with a planar workspace of 90 x 60 cm and maximum continuous force output of 30 N in each direction (see Figure 1). The handle is pinned to the distal end of the outboard link, providing a third, unactuated degree of freedom. The low friction and apparent mass at the handle (1.33 kg) makes the IM2 Robot ideally suited as a haptic device for conducting physical therapy over the internet. These two characteristics will allow the clinician to remotely assess the patient's condition as well as help the patient perform rehabilitation tasks. Implementing force-feedback in the presence of time-delay is key to realizing this technology over the internet and is a cornerstone of the control architecture presented here.

A. Virtual Reality Equipment

The 3D graphical environment was projected on a head-mounted display as shown in Figure 2. The SVGA 3D Pro I-Glasses have a resolution of 800 600 pixels and run at 60 Hz, the same rate as the refresh rate of the video card. The I-Glasses take VGA input from the computer. An InterSense InterTrax2 headtracker mounted on top of the HMD tracks the orientation of the operator's head to within 0.02 deg about all three axes. The headtracker is an inertia measurement unit with triaxial gyros and accelerometers. It is connected to the computer via USB and supported on linux with open source drivers.

Fig. 2. Subject performs virtual beam task while donning 3D Pro I-Glasses. The vantage angle is changed by using output from an InterTrax2 head tracker mounted on the brow of the display.

IV. SOFTWARE

The *InMotion² Shoulder-Elbow Robot* is controlled via an AMD XP 1800 desktop running RTLinuxFree on RedHat

7.2. RTLinux is a hard real time operating system that loads the linux kernel as a module in the real time kernel. There are a total of three processes running concurrently to calculate dynamics for realistic haptic feedback, draw a 3d graphical environment, and communicate scene information over the internet. Interprocess communication is achieved through shared memory. The control process was implemented as a hard real-time task and uses approximately 1.2% of the CPU time at a rate of 200Hz. The virtual object generator is implemented as described in Section V in the control process. Scene information was sent as a 16 byte dataset using the UDP protocol.
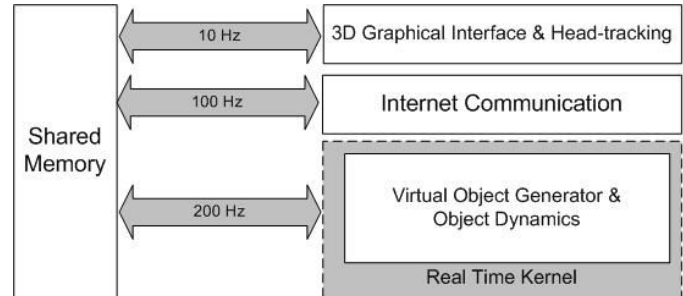

Fig. 3. Interprocess communication is through shared memory for three concurrent processes that calculate dynamics, draw 3d graphics, and communicate over internet

A. User Interface

The graphical user interface (GUI) shown in Figure 4 was built with the Tool Command Language/Toolkit (Tcl/Tk) and allows the user to change parameters for the virtual beam task. The virtual beam must stay within the workspace boundaries shown in orange. Buttons at the top of the screen are used to select the task and display position and time delay. Control and beam parameters are set using the sliders beneath. In the current configuration, we have designated the gravity vector to point in the sagital plane of the operator so that s/he is pushing away when lifting the beam, i.e. toward the screen in Figure 1. A reduced gravitational acceleration of $=3$ m/s^2 was used in order not to exceed the force capacity of the robot.

B. 3D Graphics

The 3D graphical environment shown in Figure 5 was built using Silicon Graphics Open Inventor Toolkit and sits on top of OpenGL giving a higher level control of the 3D workspace. The visual rendering typically takes place at about 10 Hz, and the position coordinates of the virtual object are read from the computer's shared memory at every cycle to update its position in the virtual scene. The head-tracker driver returns a quarternion which is used to transform the camera viewpoint in the Open Inventor scene graph such that the camera view changes with the head movements of the user. At the moment, we are only able to run the 3d graphics with a refresh rate of 10hertz because the video card is an outdated Nvidia TNT2. We anticipate the ability
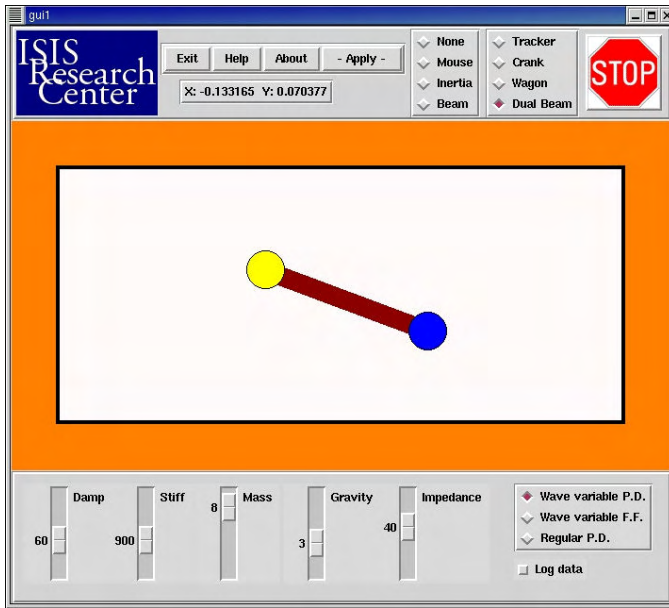
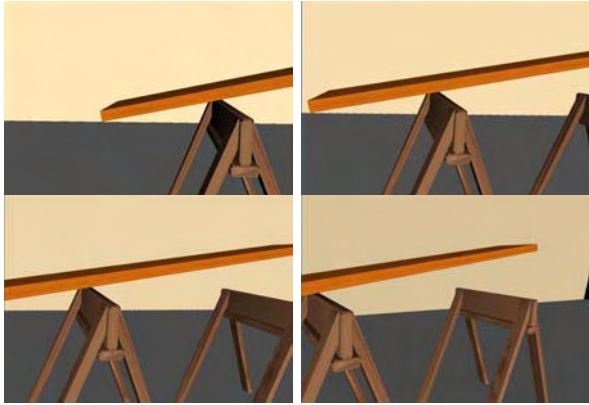Fig. 4.   Graphical user interface developed for 2D virtual beam task.

Fig. 5.   Graphical scene for 3D cooperative beam task generated with Open Inventor Toolkit. This is a series of views from left side through the head-mounted display as subject pans his head right.

to run graphics at much higher refresh rates when we find a faster video card supported by the kernel.

V. COOPERATIVE CONTROL

The technique for realizing cooperative control for performing tasks over the internet is through a virtual object generator as shown in Figure 6. In this scenario, both robots are considered "masters"that independently interact with the virtual object, which is considered the "slave". The virtual object generator (VOG) applies the sensed "interaction" forces from the masters and then calculates the dynamics response of the object. The motion of the object at each "contact" point is then transmitted back to each master where it is tracked by a PD controller.

The virtual object dynamics are calculated via a separate process on one of the master arm computers. $_1$ and $_2$ are time delays caused by computational processing and internet transit time. If the object dynamics are being calculated
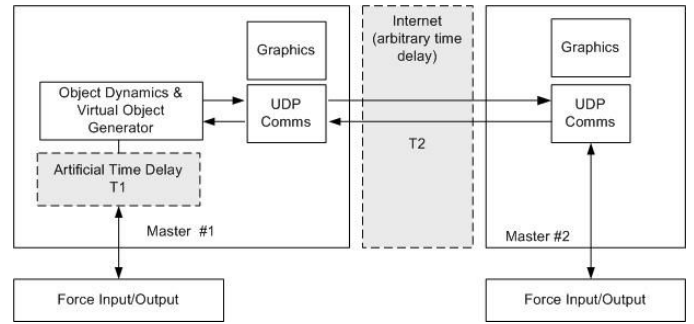

Fig. 6.   System diagram for cooperative virtual object manipulation over the internet.

on the Master 1 computer, then $_1$ is primarily due to the computational delay for the VOG process (essentially zero), and $_2$ is the time delay caused by internet transit. To maintain a truly cooperative task and avoid evoking a leader-follower strategy, an artificial time delay $_1$ based on a moving average of $_2$ is applied to the control computer hosting the virtual object process (Master 1 in this case).

An example of a cooperative rehabilitation task is shown in Figure 7. The patient and therapist "pick up" opposite ends of a virtual beam by grasping the handle that coincides with their end of the beam. Object parameters such as mass, length, and inertia can be adjusted to correspond to real-life objects using a graphical user interface on the therapist's computer. As the object is "lifted," the side that is lower will begin to feel more of the weight, thus stimulating the participants to maintain the beam in a horizontal position. Also, if one side tugs on the object, the other side feels it, thus encouraging a cooperative strategy to lift the object. The complete dynamics for the virtual beam can be found in [9].
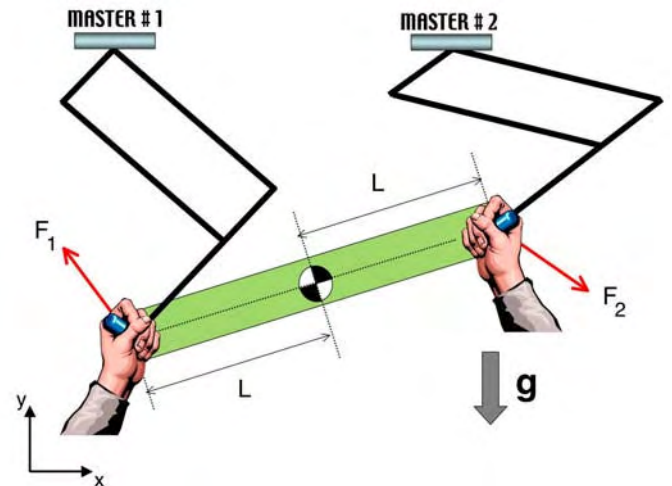

Fig. 7.   Cooperative manipulation task showing haptic masters manipulating opposite ends of a "virtual" beam across the internet.

There are ways to deal with instability caused by time delay. We have been using the wave variable approach to manipulate objects over the internet[10], [11]. Instead of sending a direct velocity or force command, an impedance

367

"wave" command is issued by the master, and then an impedance "wave" is reflected by the slave. How much of the push wave is reflected depends upon the impedance on the slave side. A soft, spring-like environment has a low impedance and will not reflect the incoming wave as greatly as a rigid environment. In addition to its impedance/admittance analog, the performance of the wave variable controller degrades only gradually with increasing time delay and is thus is well-suited to the internet. When using the wave variable approach, it is important to distinguish between which object(s) is the "master" and which is the "slave". In our application, the virtual object is regarded as the "slave" and is acted upon by virtual forces from the two IM2 robots which are the "masters".

The control architecture for the cooperative task using admittance control with wave variables is shown in Figure 8. In this scenario, each haptic master is interacts independently with the virtual object which is considered the "slave". The virtual object process then decodes the wave variables from each master into a set of force commands to be imparted on the slave. The virtual object generator calculates the resultant motion at each of the "contact" points and transmits it via wave variable back to the master. Each master control process then decodes the slave wave variables into desired velocities at its "contact" point and is then input to the master's tracking controller.
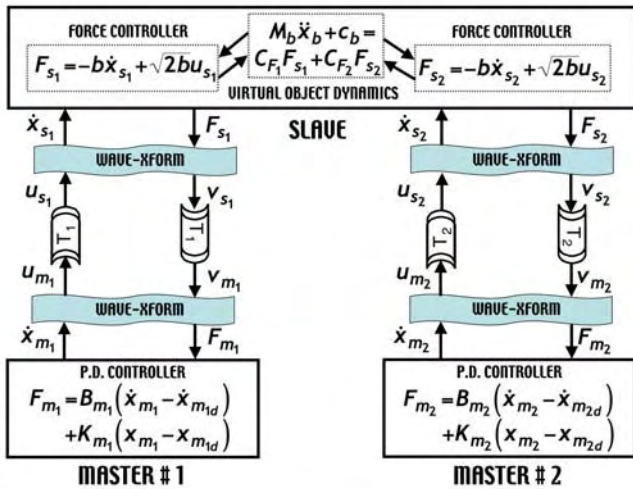

Fig. 8.   Admittance control architecture implemented with wave variables.

VI. EXPERIMENTS WITH COOPERATIVE AND UNCOOPERATIVE TASKS

Two tasks were performed within the confines of the workspace to simulate both cooperative and noncooperative control. The GUI in Figure 4 was used to activate the control process and change parameters. The nominal beam parameters were chosen to correspond to a 1×6 ft (0.305 $\times$ 1.829 m) wood (pine) shelf with mass $_b$=5.575 kg and inertia $_b$=6.215 kg-m^2. Full gravitational acceleration of =10 m/s^2 was applied to the shelf in these tests to give as realistic a simulation as possible. The control gains

were increased to $_m$=1800 N/m and $_m$=90 N/m/s to accommodate the heavier weight of the beam.

In the first task, the subject on the left attempts to lift their end of the shelf while the subject on the right holds their end fixed. The resulting beam angle in Figure 9 shows the shelf angle becoming growing in magnitude as the left end lifts up and pivots about the right side being held fixed by the uncooperative subject. The forces on the right side are plotted in Figure 10. The vertical force remains relatively constant at approximately half the shelf weight, but the force in the horizontal direction increases as the subject on the left tries to lift the beam vertically while being forced to follow a circular arc by the uncooperative subject on the right side.
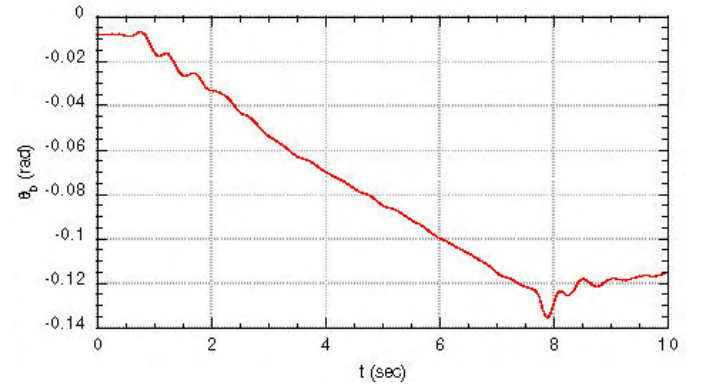

Fig. 9.   Beam angle during uncooperative lifting task.
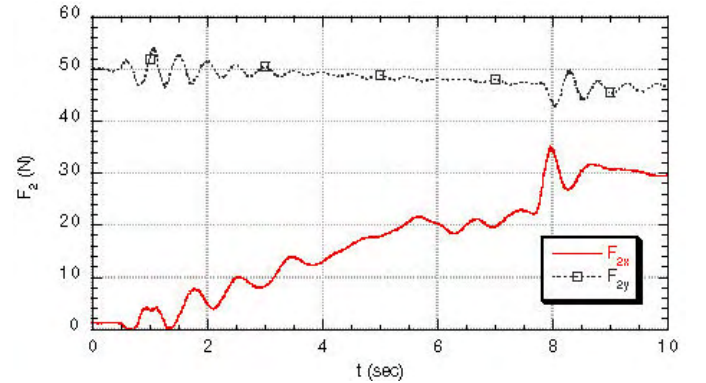
Fig. 10.   Forces on right side during uncooperative lifting task.

In the second task, both subjects attempt to lift their ends simultaneously while holding the shelf as level as possible. The shelf angle in Figure 11 remains reasonably close to zero as the shelf is lifted off the sawhorses. The forces on the right side are shown in Figure 12. The vertical force is again approximately half the shelf weight. However, the force in the horizontal direction is nearly zero since both ends are now lifting together.

VII. EXPERIMENTS WITH TIME DELAY

A. Effect of Time Delay on Wave Variables

The effect of an increase in time delay on the wave variable implementation is to decrease the system's natural

Fig. 11. Beam angle during cooperative lifting task.

Fig. 12. Forces on right side during cooperative lifting task.

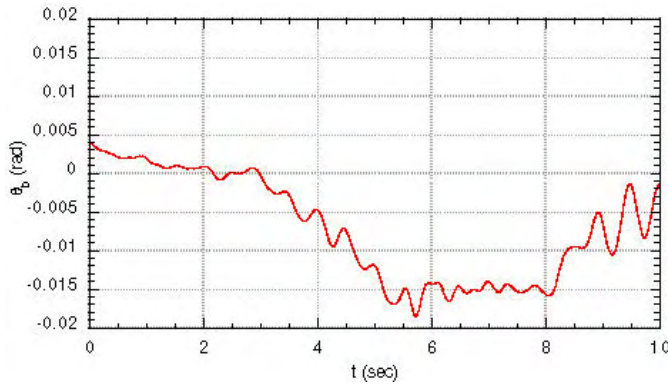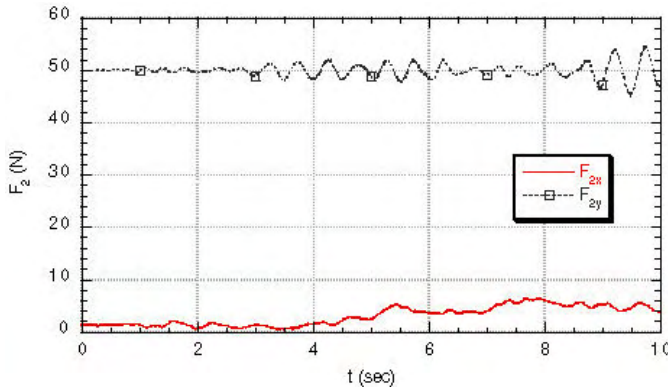frequency. The "communications stiffness" $_{com}$ is given by $_{delay}$; thus, the wave impedance should be increased in proportion to the time delay to maintain system bandwidth [6]. However, the time delay also introduces an apparent mass proportional to delay, $_{com} = _{delay}$, which produces a heavier feel at the handle as the time delay (or wave impedance) increases. Thus, a tradeoff exists in wave impedance between maintaining high system bandwidth and low inertia at the handle.

To demonstrate the robustness of the wave variable approach to time delays, a network emulation package called NIST Net was used to simulate longer internet delays. NIST Net was designed at the National Institute of Standards and Technology (NIST) for use on Linux operating systems. The emulator allows controlled, reproducible experiments with network performance sensitive applications in laboratory settings. In the time delay experiments, the beam starts out horizontally. The subject on the left side raises their side until the beam is at a 45 degree angle, while the subject on the right side maintains position. After pausing for 2-3 seconds, the left subject continues until the beam is vertical and lets the right subject (now below the left subject) support the total weight of the beam. After this, the operator on the right side lifts their side of the beam and mirrors the actions done on the left side until the beam is horizontal.

Simulation results for constant roundtrip delays of 250, 500, and 1000 msec are superposed in Figure 13 along with

the zero time delay case. The decrease in system stiffness from the zero delay test is evidenced by the lower frequency oscillations of the beam angle as the time delay gets larger. In addition, the apparent mass at the handle increases from approximately 0.5 kg for a 50 ms roundtrip delay to 20 kg for a roundtrip delay of 1 sec making manipulation of the beam even more difficult.
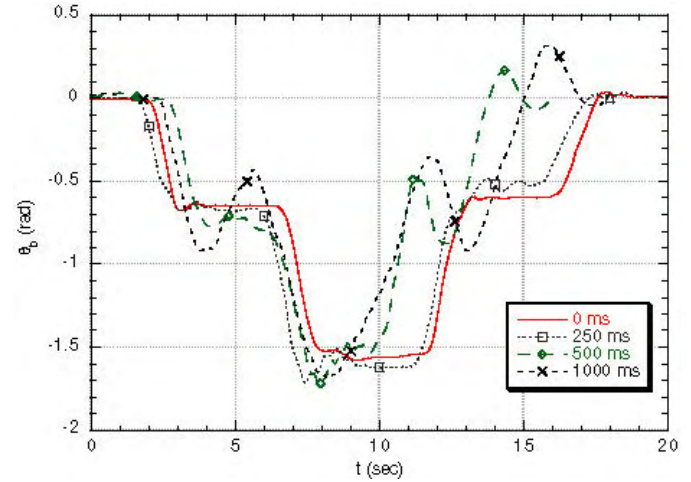

Fig. 13. Beam angle for 10 kg mass and constant time delays of 0, 250, 500, and 1000 ms under wave variable control.

B. Compensating for Packet Jitter

The User Datagram Protocol (UDP) is a non-guaranteed, best-effort datagram delivery protocol and offers less reliability than TCP in exchange for lower overhead and speedier delivery of data. These qualities makes it useful for applications such as videoconferencing and streaming multimedia, where data must be streamed constantly. An application program using UDP must deal directly with end-to-end communication problems such as packet retransmission, reordering, packetization, and reassembly. Figure 14 shows the roundtrip time for UDP packets between the John P Murtha Neuroscience Center (Johnstown, PA) and Georgetown University (Washington, DC) observed over a period of 60 seconds. Figure 15 shows the variability of the time delay, known as packet jitter, calculated from the difference between the time delay of each sample. The communications frame rate is fixed at 100 Hz (period of 10 ms) however the data shows that only 72% of all incoming packets arrive within 10 ms of the previous packet. We are currently developing for the receiving end an adaptive jitter buffer that is capable of maintaining the framerate and order of most packets. All packets arriving into the buffer are held for a specified amount of time, allowing packets that arrive later to be placed in the correct order in the buffer. Data from the buffer is fed into the dynamics process at a fixed rate of 100 Hz. By dynamically changing the size of the buffer based on the amount of packet jitter, we can keep the buffer size minimal while maintaining a certain level of jitter compensation. This technique reduces packet jitter at the expense of increasing the apparent time delay. Figure 16

shows the distribution of packet jitter for the sample data collected. According to the chart, if the jitter buffer is set to 20ms, the average time delay is increased by 20ms whereas 86% of packets arrive in correct order and at a fixed rate.
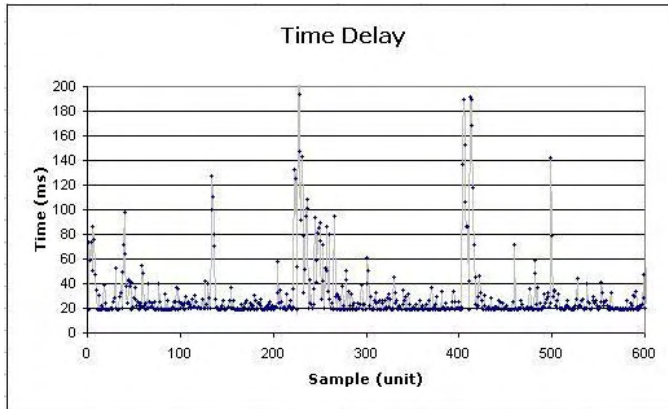

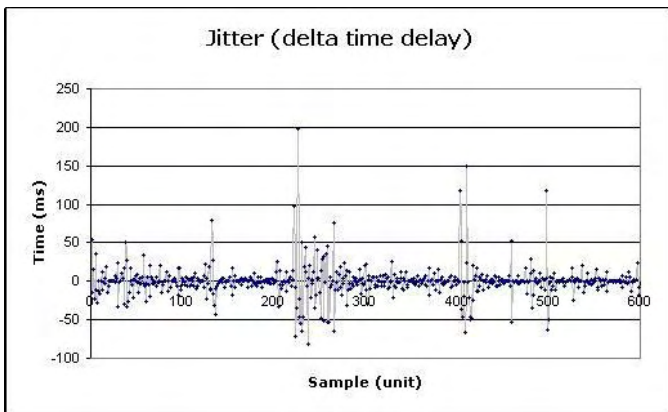Fig. 14. Time delay of packets between Washington, DC and Johnstown, PA over 60 seconds.

Fig. 15. Packet jitter of packets between Washington, DC and Johnstown, PA

VIII. CONCLUSIONS

The focus of our research is to enable cooperative rehabilitative tasks in virtual environments using force-feedback devices. This paper has outlined a strategy for cooperative, force-feedback control of virtual objects over the internet based on an admittance control architecture using wave variables. The wave variable approach was stable for a wide range of time delays tested, including artificial delays of over 1 sec. The virtual environment was created using the Open Inventor Toolkit rendered on a orientation tracked head-mounted display. Future work will focus on generating more realistic 3D tasks created using the Open Inventor Toolkit aimed at improving recovery from stroke paralysis and other neurological disorders.
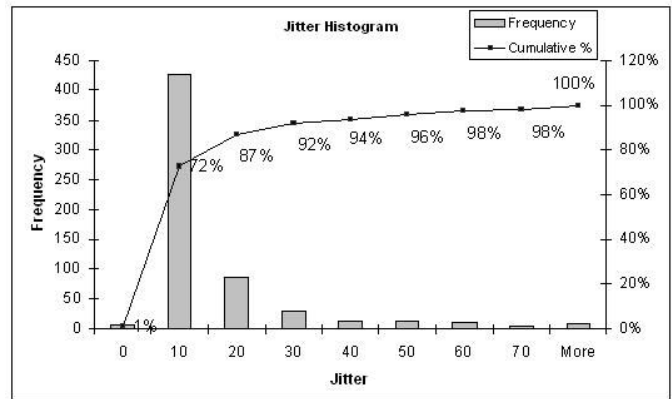
IX. ACKNOWLEDGMENTS

Fig. 16. Distribution of packet jitter

REFERENCES

[1] R. C. V. Loureiro, C. F. Collin, and W. S. Harwin, "Robot aided therapy: challenges ahead for upper limb stroke rehabilitation," in *Proc. 5th Int. Conf. on Disability, Virtual Reality and Assoc. Technologies*, Oxford, UK, 2004, pp. 33 – 39.

[2] R. Howe and D. Kontarinis, "Task performance with a dextrous teleoperated hand system," in *Proc. of SPIE*, vol. 1833, 1992, pp. 199–207.

[3] G. C. Burdea, *Force And Touch Feedback For Virtual Reality*. New York: John Wiley and Sons, 1996.

[4] I. Goncharenko, M. Svinin, S. Matsumoto, S. Hosoe, and Y. Kanou, "Design and implementation of rehabilitation haptic simulators," in *Proc. Int. Workshop on Virtual Rehabilitation*, 2003, pp. 33–39.

[5] H. Yano and H. Iwata, "Cooperative work in virtual environment with force feedback," in *Proc. 7th Int. Conference on Artificial Reality and Tele-existence (ICAT'97)*, 1995, pp. 203–210.

[6] G. Niemeyer and J.-J. Slotine, "Designing force reflecting teleoperators with large time delays to appear as virtual tools," in *Proc. IEEE Int. Conf. on Robotics and Automation*, 1997, pp. 2212–2218.

[7] R. J. Adams and B. Hannaford, "Stable haptic interaction with virtual environments," *IEEE Trans. on Robotics and Automation*, vol. 15, no. 3, pp. 465–474, June 1999.

[8] H. I. Krebs, N. Hogan, W. Hening, S. Adamovich, and H. Poizner, "Procedural motor learning in parkinsons disease," *Experimental Brain Research*, no. 141, pp. 425–437, 2001.

[9] C. Carignan and P. Olsson, "Cooperative control of virtual objects over the internet using force-reflecting master arms," in *Proc. IEEE Int. Conf. on Robotics and Automation*, 2004, pp. 1221–1226.

[10] G. Niemeyer and J.-J. Slotine, "Using wave variables for system analysis and robot control," in *Proc. IEEE Int. Conf. on Robotics and Automation*, 1997, pp. 1619–1625.

[11] G. Niemeyer and J.-J. Slotine, "Towards force-reflecting teleoperation over the internet," in *Proc. IEEE Int. Conf. on Robotics and Automation*, 1998, pp. 1909–1915.

370

8.7 Wilson 2006: Electromagnetic Tracker Accuracy …

Reprint begins on the next page and is eight pages.

Electromagnetic tracker accuracy in the CyberKnife suite

Emmanuel Wilson*[a], Rebecca Slack[b], Filip Banovac[a], Sonja Dieterich[c], Hui Zhang[a], Kevin Cleary[a]

[a]Imaging Science and Information Systems (ISIS) Center, Department of Radiology, Georgetown University, 2115 Wisconsin Avenue, Suite 603, Washington, DC
[b] Department of Biostatistics, Bioinformatics, and Biomathematics, Georgetown University
[c] Department of Radiation Medicine, Georgetown University Hospital / MedStar Health,

ABSTRACT

Electromagnetic trackers have found inroads into medical applications as a tool for navigation in recent years. Their susceptibility to interference from both electromagnetic and ferromagnetic sources have prompted several accuracy assessment studies in past years. To the best of our knowledge, this is the first accuracy study conducted to characterize measurement accuracy of an NDI AURORA electromagnetic tracker within a CyberKnife radiosurgery suite. CyberKnife is a frameless, stereotactic radiosurgery device used to ablate tumors within the brain, spine and in recent years, the chest and abdomen. This paper uses a data collection protocol to collect uniformly distributed data points within a subset of the AURORA measurement volume in a CyberKnife suite. The key aim of the study is to determine the extent to which large metal components of the CyberKnife stereotactic radiosurgery device and robot mount contribute to overall system performance for the AURORA electromagnetic device. A secondary goal of the work is to determine the variation in accuracy and device behavior with the presence of ionizing radiation when the LINAC is turned on.

Keywords: electromagnetic tracking, CyberKnife, Aurora, radiosurgery, accuracy analysis.

1. INTRODUCTION

The use of electromagnetic tracking systems (EMTS) as a tracking modality for medical applications has grown sharply in recent years. This has in part been due to the miniaturization of tracking sensor coils and refinement of tracking algorithms. Their main benefit over other conventional tracking modalities such as optical trackers is their lack of dependence on line-of-sight for operation. This allows for greater freedom of operation for the surgeon and facilitates the tracking of flexible endoscopes and needles within the body.

The main drawback of EMTS however, is their susceptibility to electromagnetic interference. The interferences can arise from electrical sources and ferromagnetic metals in close proximity to the electromagnetic tracker [6]. Measurement errors are largely idiosyncratic in nature and vary greatly between environments. Therefore, quantification of these errors can be performed in each environment prior to deployment of an Image-Guided Surgery (IGS) procedure, by collecting data using a calibration phantom [1, 4, 5].

The effectiveness of any surgical navigation is largely dependent on the accuracy and reliability of the tracking system. The purpose of accuracy studies therefore, is to quantify the measurement errors within an operating volume and determine optimal work conditions. For this reason, accuracy studies for medical applications of EMTS thus far have largely been for interventional applications where the use of an IGS system is anticipated [1, 7].

---

* WilsonE@isis.georgetown.edu, Tel: (202) 687 2902, Fax: (202) 784 3479

To the best of our knowledge, this is the first study conducted to quantify the accuracy of an EMTS within a CyberKnife (Accuray Inc., Sunnyvale, CA) suite. The CyberKnife device functions as an ablative tool by delivering multiple beams of highly focused radiation to tumor sites. CyberKnife is a non-invasive, frameless, stereotactic radiosurgery device, initially used for the treatment of largely immobile tumors such as spine and brain. The device consists of a 6-MeV medical grade linear accelerator (LINAC) mounted on a robotic arm (KUKA, Germany). The recent addition of the Synchrony system enables the tracking and compensation of tumor motion due to respiration. This is achieved through the use of a stereo X-ray imager and a FlashPoint infrared optical tracker. Infrared markers are affixed to the patient vest. Small (0.8mm diameter) gold fiducials are implanted percutaneously near the tumor site. Prior to treatment a correlation model between internal fiducials and external IR markers is generated. The robot is then commanded to follow this model. During treatment, X-ray images are acquired every 30-40 seconds to verify this correlation model.

CyberKnife is the only radiosurgery system available today that is capable of targeting tumors with respiratory motion artifacts. One potential issue is the radiation dose from the periodic X-ray imaging used to verify internal tumor location. A real-time, non ionizing, method of continuously tracking internal tumor location would thus be desirable. Current EMTS are capable of providing measurements in real-time and could potentially satisfy this requisite function, provided they are able to offer sufficient accuracy in the CyberKnife environment.

There are two key goals for this study. The first is to quantify baseline accuracy of an EMTS within the CyberKnife suite. The second is to provide a formal analysis of changes in measurement accuracy and device performance in the presence of ionizing radiation while the CyberKnife system is active.

2. MATERIALS AND METHODS

2.1 Measurement device

A prototype unit of the NDI AURORA electromagnetic tracking device (Northern Digital Inc., Waterloo, Canada) was evaluated within the CyberKnife suite. The device consists of a flat field generator (FG) that creates a pulsed AC magnetic field. The FG is connected to a system control unit (SCU), which interfaces to the computer through an RS-232 serial connection. The AURORA device has a manufacturer quoted RMS positional accuracy of 0.8mm and RMS orientation accuracy of 0.3°. The quoted accuracy is for tests conducted in a ferromagnetically clean environment and often hard to repeat in a typical work environment. However, we have found device accuracy in a 'clean' office environment, at our research facility void of any metal components within a 1-meter radial distance from the field generator, to be 1.5mm RMS positional and 0.5° RMS orientation errors. Measurements were made using a pair of 5-DOF (degree of freedom) MagTrax needles (Traxtal Technologies, Bellaire, TX, USA) with embedded sensor coils. An NDI Optotrak infrared optical tracking device was used also to collect measurements simultaneously with the AURORA device. Optotrak records measurement with 3-DOF and has an RMS position accuracy of 0.1mm. Since the accuracy of this device is close to one magnitude better than AURORA accuracy, it was chosen to use this device as ground truth.

2.2 Calibration phantom

A precision tri-stage motion platform consisting of 3 linear actuators driving lead screws along 3 orthogonal axes was used for the data collection. The motion along each axis is accurate to 0.05mm. Since the motion platform is largely made of aluminum, a sensor mount was machined out of plexiglass to mount sensor needles and IR markers at the distal end of the arm. A control program was written to move the motion platform along a predetermined path at fixed intervals and poll the AURORA and Optotrak devices for position measurements successively. A total of 100 measurement cycles from each device were logged on the host computer at each data collection node. A data collection volume of 240 x 240 x 240mm located 75mm in front of the AURORA FG was defined for the data collection. Data collection nodes were distributed evenly at 40mm intervals along the X, Y and Z-axes. Fig 1 provides a view of the test setup within the CyberKnife suite.
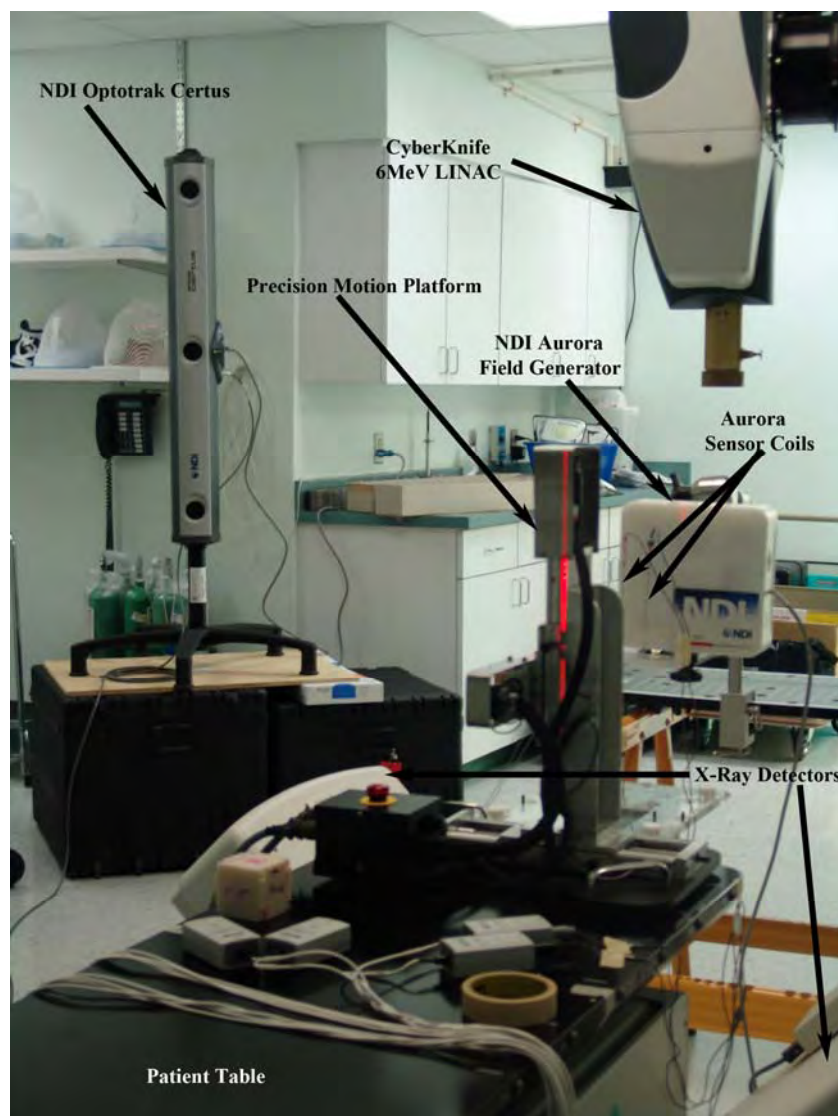
Figure 1: Test setup within the CyberKnife suite

2.3 CyberKnife test

A total of 10 baseline tests and 3 tests with the CyberKnife LINAC beam turned on were conducted around the robot isocenter. The CyberKnife treatment plan devised consisted of 2 paths and was typical of those used to treat liver tumors. A 20mm collimator was used for all beam ON tests and the robot isocenter used as the target for beam convergence. The first treatment path consisted of 41 beams delivering a total of 804 MU (monitor units) of radiation and the second path consisted of 22 beams delivering a total of 438 MU. The CyberKnife device is calibrated such that 1MU of radiation is equivalent to 1 rad (or 1cGy) at the CyberKnife collimator tip. All beams were of 2s duration and the entire procedure lasted 20 minutes.

2.4 Position error

A least square minimization of errors technique was used to transform data points from the AURORA coordinate space to Optotrak coordinate space [3]. Measurement at each point was taken as the average of the 100 data samples. Position error was defined as the Euclidean distance between transformed AURORA points and corresponding measured Optotrak points. 8 points were manually selected for registration based on proximity to FG so as to provide low initial error. The same 8 registration points were used for all tests.

2.5 Orientation error

Since the needles are fixed firmly within the mount, the relative orientations of the needles theoretically do not change during a test. In practice however, slight variability will exist and for purposes of this study have been characterized as the orientation error. The orientations at the 8 registration nodes were averaged to provide a reference orientation. At each node, orientation error was then evaluated as the angular difference between reference orientation and the average of 100 orientation samples at the specific node. In addition, the variance within the 100 samples at each data node was evaluated as a measure of the jitter in AURORA measurements.

2.6 Statistical analysis

Generalized linear models were utilized for repeated measures regression to investigate the relationships between both the position and orientation errors and field generator (FG) to sensor separation separately for each error measure and test condition for multiple repeated tests. It is known that error distribution is non-isotropic for EMTS [2]. Therefore, it was chosen to model the errors not only as a function of FG to sensor separation, but also as a function of position along the X, Y and Z axes. The natural log of the error data was taken prior to analysis to accommodate the assumption of normally distributed errors around the model estimate. The regression model included the three axes, all possible interactions of the axes, the FG to sensor separation, and an indicator variable for needle 1. Additionally, to check for consistency across experiments, an exploratory analysis was done examining the significance and parameter direction for each test separately. Any factor was considered significantly associated with error measurement if the p-value for the parameter estimate was less than 0.05. P-values indicate whether the parameter estimate is significantly different from 0, indicating an effect of that variable on the specified measurement error. The sign of the parameter estimate is an indication of whether the error increases or decreases with increasing values of the variable.

3. RESULTS

3.1 Baseline results

An RMS position error of 3.1mm and average position error of 2.7mm were computed for the 10 baseline tests. RMS orientation error was evaluated to be 0.9°, mean orientation error of 0.7°. Boxplots of position and orientation errors for the 10 tests is provided in Fig 2. Fig 3a and 3b provide histograms of collective position and orientation errors for the two needles over the 10 tests. The errors were shown to fit a log-normal distribution.
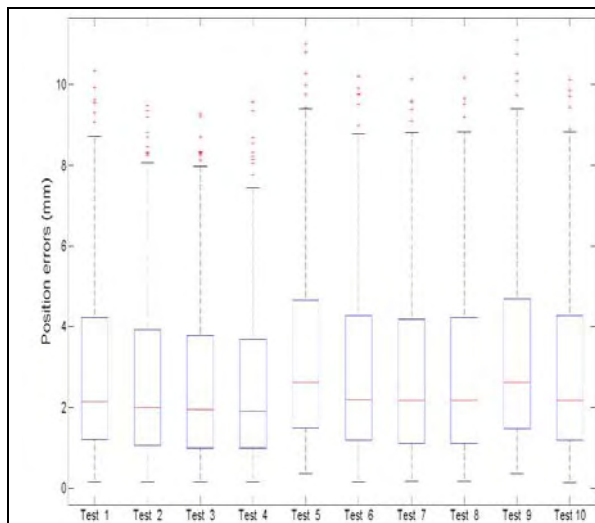
Figure 2a: Boxplot summary of position errors for baseline tests	Figure 2b: Boxplot summary of orientation errors for baseline tests
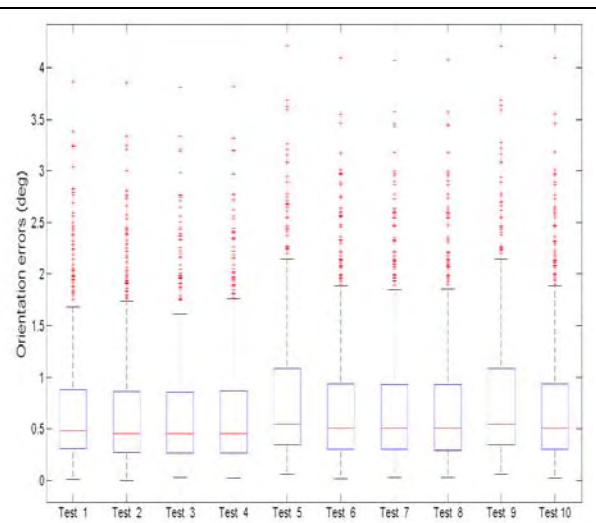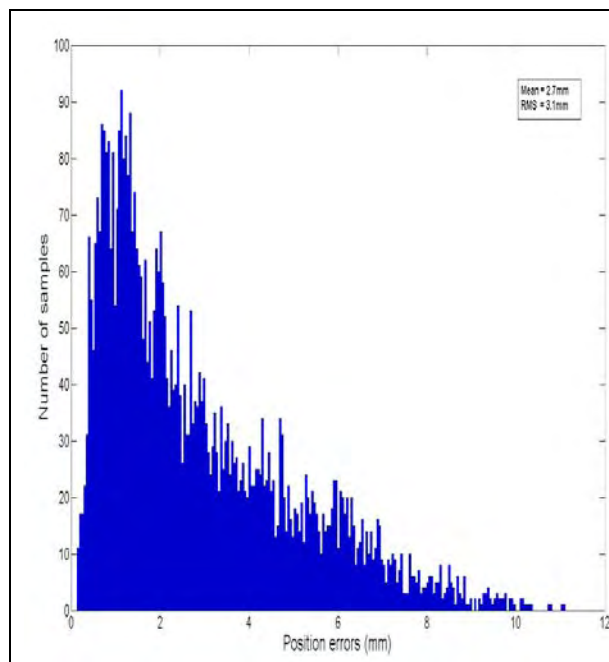
| Figure 3a: Histogram of position error for baseline tests | Figure 3b: Histogram of orientation error for baseline tests |
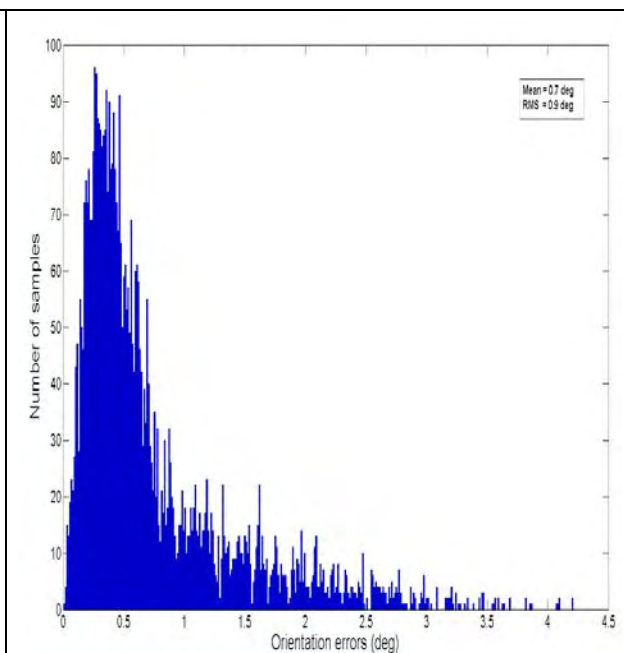
3.2   LINAC beam ON results

RMS position error of 2.3mm and average position error of 1.7mm were noted for the 3 baseline tests. RMS orientation error was evaluated to be 0.9° and mean orientation error to be 0.6°. Boxplots of the position and orientation errors are provided in Fig 4a and 4b respectively. Fig 5a and 5b provide histograms of collective position and orientation errors for the two needles. The reduced position and orientation errors for CyberKnife beam ON tests are largely explicable due to the reduced number of tests (10 tests for baseline as opposed to 3 tests for beam ON).

| Figure 4a: Boxplot summary of position errors for LINAC beam on tests | Figure 4b: Boxplot of orientation errors for LINAC beam on tests |

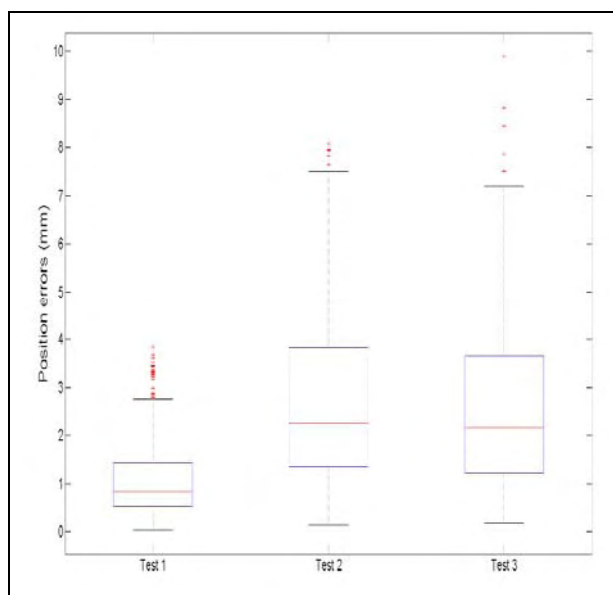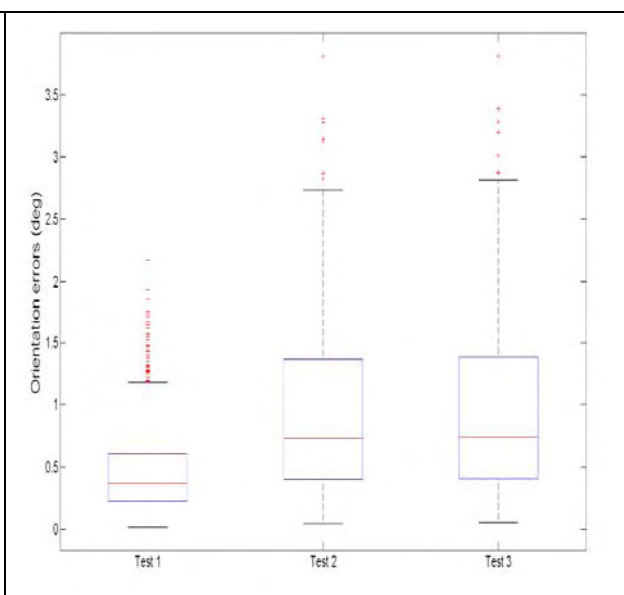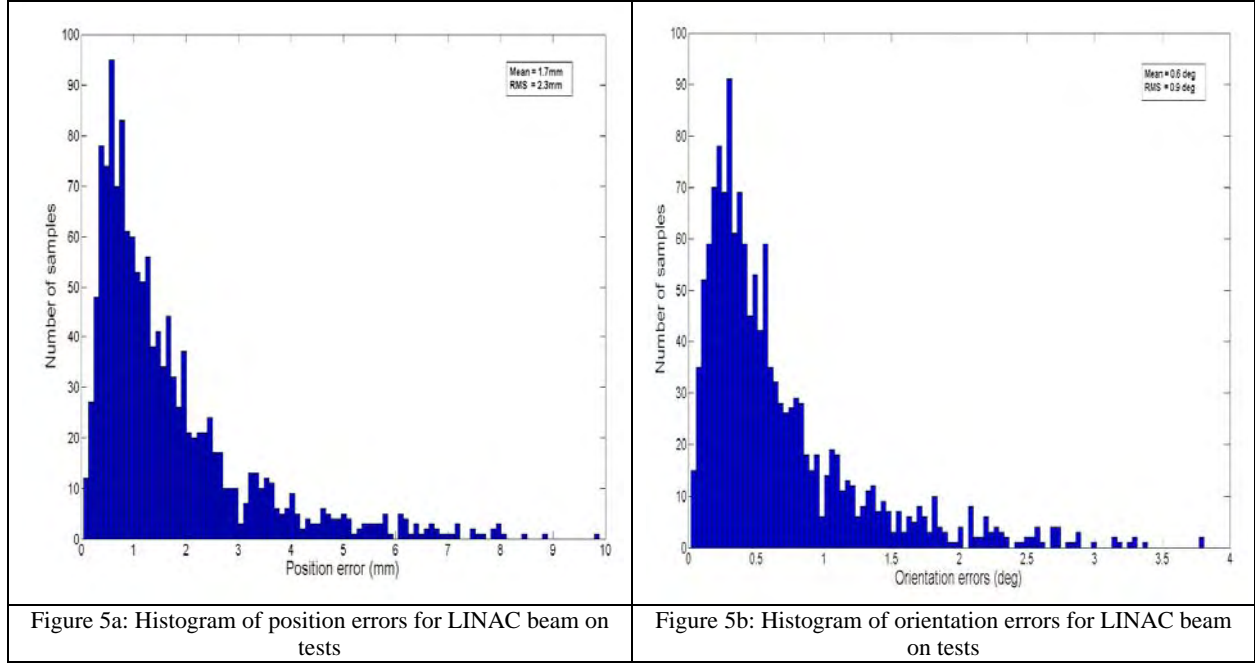| Figure 5a: Histogram of position errors for LINAC beam on tests	Figure 5b: Histogram of orientation errors for LINAC beam on tests

3.3 Model results

Baseline versus LINAC beam ON conditions were significantly different from each other for both magnitude and orientation ($p<0.0001$ for each). The overall results are presented in Table 1 for baseline experiments and Table 2 for active experiments. This difference is most notable in the Y axis since the direction of the parameter estimates (positive versus negative) change depending on the condition (baseline versus active).

The parameters from these models, displayed in Tables 1 and 2, can be used to create regression equations that model the position and orientation errors as a function of the data point within the AURORA measurement volume, FG to sensor separation (d_{FG}) and the interactions between the individual axes. The regression equation defining position error for baseline (Err_{Lpos}) and LINAC (Err_{Bpos}) active tests are provided in Equations 1 and 2 respectively. The needle effect is ignored for further discussion as it is included as a control for appropriate estimation, but is not of interest as a condition affecting accuracy.

$$\ln(Err_{Lpos}) = -1.63 - 0.005X - 0.002Y + 0.0004Z + 0.009d_{FG} + 0.061Needle1 \qquad \text{(Eq. 1)}$$
$$- 0.000007XY - 0.000009XZ - 0.0001YZ - 0.00000005XYZ$$

$$\ln(Err_{Bpos}) = -2.242 + 0.003X + 0.008Y + 0.001Z + 0.012d_{FG} - 0.066Needle1 \qquad \text{(Eq. 2)}$$
$$- 0.00005XY + 0.00002XZ + 0.00001YZ - 0.0000008XYZ$$

The most noticeable trend from the linear model analysis was the reversal of the effects of the Y axis and the interaction of Y and Z axes between baseline tests and LINAC beam on tests. This shows the primary differences between testing conditions. Additionally, there was decreased significance between position errors and Z-axis locations for beam ON tests compared to baseline tests. In contrast, the largest parameter estimates were consistently for FG to sensor separation, regardless of test type or error type. Note that each measure is highly statistically significant. However, the parameter size indicated a small effect of each parameter, indicating small errors. Table 3 presents estimates of errors for specific values of X, Y, and Z for needle 1. The position errors range from (min) to (max), all of which are very small. Similarly, the orientation errors range from (min) to (max), indicating successfully small errors throughout the measurement space.

For the analyses examining each experiment separately, parameters with larger p-values, such as the Z- axis, the significance fluctuated more between tests. In addition a distinct sign change for Y-axis and Y-Z-axis interactions was observed between baseline and beam ON trials, indicating that the effect of the Y axis on the magnitude of the errors was reversed in the Cyberknife suite, consistent with findings in the overall analyses above. In contrast, for both baseline tests and beam ON tests, the significance for FG to sensor separation was strong for all tests and the estimate always positive, implying that an increase in FG to sensor separation was strongly associated to an increase in error.

Table 1: Model results for baseline tests

	Position Error			Orientation Error	
Parameter	*Estimate*	*p-value*		*Estimate*	*p-value*
Intercept	-1.630	<0.0001		-2.667	<0.0001
X-Axis	-0.005	<0.0001		-0.007	<0.0001
Y-Axis	-0.002	<0.0001		-0.002	<0.0001
Z-Axis	0.0004	0.0012		0.006	<0.0001
FG Distance	0.009	<0.0001		0.012	<0.0001
Needle = 1	0.061	<0.0001		0.104	<0.0001
Interaction X-Y- Axes	-0.000007	<0.0001		-0.000002	0.29
Interaction X-Z- Axes	-0.000009	<0.0001		-0.00004	<0.0001
Interaction Y-Z- Axes	-0.00001	<0.0001		-0.000008	<0.0001
Interaction X-Y-Z- Axes	-0.00000005	<0.0001		-0.00000007	<0.0001

Table 2: Model results for beam ON tests

	Position Error			Orientation Error	
Parameter	*Estimate*	*p-value*		*Estimate*	*p-value*
Intercept	-2.242	<0.0001		-2.403	<0.0001
X-Axis	0.003	<0.0001		-0.009	<0.0001
Y-Axis	0.008	<0.0001		0.008	<0.0001
Z-Axis	0.001	0.012		0.012	<0.0001
FG Distance	0.012	<0.0001		0.016	<0.0001
Needle = 1	-0.066	0.0008		0.193	<0.0001
Interaction X-Y- Axes	-0.00005	<0.0001		-0.00008	<0.0001
Interaction X-Z- Axes	0.00002	<0.0001		-0.00005	<0.0001
Interaction Y-Z- Axes	0.00001	0.002		0.000002	0.49
Interaction X-Y-Z- Axes	-0.00000008	0.003		-0.0000002	<0.0001

Table 3. Comparison of estimated and actual errors from model equations for arbitrary position values.

Variables				Actual Errors		Estimated Errors	
X	Y	Z	FG distance	Position	Orientation	Position	Orientation
175.48	139.3	-92.26	242.31	0.2	0.4	0.69	0.42
55.38	21.88	-135.51	148.01	0.62	0.06	0.60	0.18
54.17	-139.27	-134.92	201.33	0.7	0.39	1.08	0.38
185.52	-18.19	-371.73	415.85	5.43	2.56	5.20	4.75
-105.01	102.03	-220.65	264.81	2.54	0.46	2.77	0.34

4. DISCUSSION

Continual refinement of electromagnetic tracking algorithms and sophistication in hardware implementations has brought about improvements in measurement accuracy and reliability for electromagnetic tracking systems. This study has evaluated the accuracy of an EMTS within this environment under the influence of ionizing radiation.

The results of this study indicate that while there are noticeable trends in AURORA system performance with and without the presence of ionizing radiation, the overall effect on measurement accuracy is minimal. Based on these results the AURORA device has the potential to work well within the CyberKnife suite, either as part of an IGS application or as a means for direct, continuous tumor tracking during a stereotactic radiosurgery procedure within the CyberKnife suite. Further studies are planned to verify this supposition.

ACKNOWLEDGEMENTS

REFERENCES

[1]   W Birkfellner, F Watzinger, F Wanschitz et al., "Calibration of tracking systems in a surgical environment" IEEE Trans. Med. Imaging 17(5) 1998; 737-742

[2]   D. D. Frantz, A. D. Wiles, S. E. Leis and S. R. Kirsch "Accuracy assessment protocols for electromagnetic tracking systems" Phys. Med. Biol (48) 2003; 2241-2251

[3]   B. K. P. Horn "Closed-form solution of absolute orientation using unit quaternions" Opt. Soc. Of America (7) April 1987; 629-642

[4]   J Hummel, M. R. Bax, M. L. Figl et al., "Design and application of an assessment protocol for electromagnetic tracking systems" Med. Phys. 32(7) July 2005; 2371-2379

[5]   J Hummel, M. L. Figl, C. Kollmann et al., "Evaluation of a miniature electromagnetic position tracker" Med. Phys. 29(10) October 2002; 2205-2212

[6]   M. A. Nixon, B. C. McCallum and N. B. Price "The effects of metals and interference fields on electromagnetic trackers" Presence 7(2) April 1998; 204-218

[7]   K Schicho, M. L. Figl, M Donat et al., "Stability of miniature electromagnetic tracking systems" Phys. Med. Biol. (50) 2005; 2089-2098

[8]   A Schweikard, H Shiomi and J Adler "Respiration tracking in radiosurgery without fiducials" Int. J Medical Robotics and CAS 1(2) 2005; 19-27

8.8 Xu 2006: CT Fluoroscopy-Guided Robotically …

Reprint begins on the next page and is eight pages.

CT Fluoroscopy-Guided Robotically-Assisted Lung Biopsy

Sheng Xu[*][a], Gabor Fichtinger[a], Russell H. Taylor[a], Filip Banovac[b],
and Kevin Cleary[b]

[a]Engineering Research Center, Johns Hopkins University,
Baltimore, MD 21218, MD USA;
[b]Imaging Science and Information Systems (ISIS) Center, Department of Radiology,
Georgetown University Medical Center, Washington, DC 20007 USA

ABSTRACT

Lung biopsy is a common interventional radiology procedure. One of the difficulties in performing the lung biopsy is that lesions move with respiration. This paper presents a new robotically assisted lung biopsy system for CT fluoroscopy that can automatically compensate for the respiratory motion during the intervention. The system consists of a needle placement robot to hold the needle on the CT scan plane, a radiolucent Z-frame for registration of the CT and robot coordinate systems, and a frame grabber to obtain the CT fluoroscopy image in real-time. The CT fluoroscopy images are used to noninvasively track the motion of a pulmonary lesion in real-time. The position of the lesion in the images is automatically determined by the image processing software and the motion of the robot is controlled to compensate for the lesion motion. The system was validated under CT fluoroscopy using a respiratory motion simulator. A swine study was also done to show the feasibility of the technique in a respiring animal.

Keywords: lung biopsy, robot, motion tracking, computer integrated surgery

1. INTRODUCTION

1.1 Clinical Significance

Lung biopsy is a common interventional radiology procedure. The purpose of the procedure is to obtain a tissue sample from a suspicious lesion in the lung. This tissue sample is then analyzed by a pathologist to determine if cancer is present. As lung cancer screening becomes more prevalent, an increasing number of suspicious lesions will be found, and more lung biopsies will be required[1].

One of the difficulties in lung biopsy is that lesions move with respiration, which can make it difficult to locate lesions and accurately perform the biopsy. CT fluoroscopy (CTF) combines the advantages of both CT and fluoroscopy in that moving lesions in internal organs can be viewed in nearly real-time, allowing compensation for respiratory motion during the intervention. It is also possible to see the needle's interaction with the target lesions under CTF, resulting in improved success rate of the percutaneous biopsy[2] (CTF 93.7% vs. CT 88.2%). Additionally, CTF decreases procedure time by at least a factor of 2 compared with conventional CT guided procedures[3].

Currently, lung biopsy is performed freehand. Based on preoperative image data, the physician identifies the skin entry point and the lesion, thus defining the desired needle trajectory. The physician then aligns the needle by hand and partially inserts it towards the lesion. The physician proceeds with further insertion of the needle, checking the position of the needle by re-scanning as necessary. The main problem with freehand biopsy is that the physician's accuracy is limited when initially lining up the needle and then staying on course throughout the procedure. Additionally, when the physician releases the needle, the needle can drift or tilt away from the desired path. In

---

[*] sheng@cs.jhu.edu; phone 1 301 594-2073; fax 1 410 516-5553

response to these problems, we propose integrating CTF imaging with a medical robot for precise placement of the needle.

1.2 Prior Technical Developments

For robotically assisted needle placement, one important concept is the remote center of motion (RCM) which provides rotational motion around a fixed fulcrum point in space. Stoianovici developed a two degrees-of-freedom (DOF) RCM robot with a radiolucent needle driver for percutaneous renal access under fluoroscopic guidance[4]. Taylor adapted the RCM module for microsurgical augmentation[5].

In addition to the hardware developments, many robotic systems have been integrated with guiding imaging modalities. Hong[6] presented an ultrasound-driven needle-insertion robot for percutaneous cholecystostomy. Loser[7] presented a system for needle insertion guided by visual servoing in a CTF scanner. Bascle presented an approach for needle placement under X-ray fluoroscopy[8]. Susil[9] developed a registration method using a Z-frame for needle insertion inside a CT scanner.

2. METHOD

2.1 System Components

As shown in figure 1, the main system components include a CTF scanner, a needle insertion robot with an associated control computer, a Z-frame, a frame grabber, and an image processing computer.
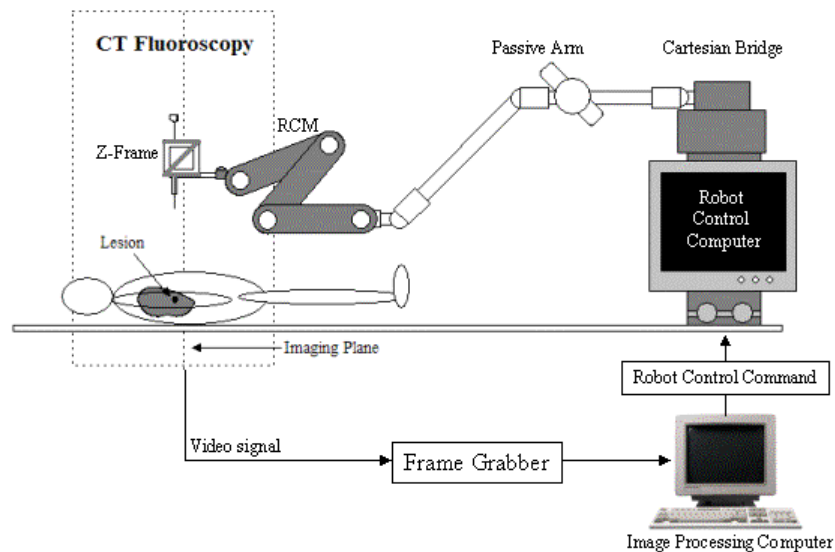
Figure 1: System components

The CTF scanner is a Siemens Somatom Volume Zoom. The maximum frequency of the CTF scan is approximately 6Hz. The needle placement robot was developed by the Urology Robotics Group at Johns Hopkins Medical Institutions[10]. It includes a 3-Degrees-Of-Freedom (DOF) Cartesian motion stage mounted on the CT table so that the robot will move with the CT table. The Cartesian stage is connected to a 7-DOF adjustable unencoded passive arm, used for gross positioning of the needle drive stage. The rotation stage is a 2-DOF RCM. The needle drive stage is a 1-DOF friction transmission with a radiolucent end-effector[8] integrated with a Z-frame for registration of the robot and CT[9]. During the lung biopsy intervention, CTF images are obtained as needed to position the needle. The real-time display from the CTF monitor is captured using a frame grabber (Accustream 170, Foresight Imaging,

Lowell, Massachusetts, USA). The frame grabbed images are processed by an image processing computer to estimate the real-time position of the target lesion. The image processing computer then uses the inverse kinematics of the robot to generate control commands which are sent to the robot through an ethernet cable and TCP/IP connection. The robot then moves accordingly to compensate for the respiratory motion of the patient.

2.2 Clinical Workflow

The envisioned scenario for CTF-guided robotically assisted lung biopsy is as follows:

1. The patient is scanned under breath holding to obtain a 3D preoperative CT volume at the end-of-inspiration.
2. The physician selects the entry and target locations of the biopsy path in the CT volume.
3. The physician starts the CTF scan, allowing the system to track the real-time position of the target lesion.
4. Patient's skin at the entry point is anesthetized with 1% Lidocaine.
5. The robot moves the needle to the entry point, aligns the needle with the path, and inserts the needle into the target lesion based on the motion tracking result.
6. The robot releases the needle.
7. The physician manually inserts the needle under the guidance of the needle holder of the robot.
8. The physician injects the therapeutic agent or takes the biopsy sample.

In order to increase safety, the physician supervises the needle insertion at the robot control computer. The system can be halted at any time by the physician. Before the needle enters the body, the robot can make quick adjustments of the needle pose based on the real-time position of the target lesion. The patient holds their breath during the needle insertion to ensure accurate targeting and to avoid potential needle bending. Once the needle is in the lesion, the robot should release the needle so that the patient can breathe again and the needle can move freely with respiration. The current needle driver does not allow us to release the needle, but a new version of the needle driver is being designed to include this feature.

2.3 Three Dimensional Motion Tracking of Pulmonary Lesions

In lung biopsy, the position of the target lesion may vary due to intrinsic causes such as respiratory motion or extrinsic reasons such as interactions between the tissue and a surgical tool. The positioning information of the lesion obtained from the preoperative CT scan may not be correct during the intervention. Therefore, it is necessary to track the lesion's motion in 3D space. CTF can be used for motion tracking in that it allows the tissue inside the imaging plane to be viewed in real-time. In order to estimate both in-plane and out-of-plane motion of the lesion, the patient needs to be positioned carefully on the CT table so that the lesion moves within a certain distance from the imaging plane during respiration. This is feasible because respiratory motion is limited to a few centimeters, allowing the off-plane motion of the target lesion to be estimated using the lung tissue inside the imaging plane. The motion-tracking algorithm is based on minimizing the Zero-mean Sum of Squared Differences (ZSSD) between a reference CTF image region and a corresponding region in the preoperative CT volume. The relative position between the target and the reference CTF region can be obtained in the preoperative CT volume, which can be used to estimate the lesion's real-time position with respect to the CTF imaging plane. The details of this tracking algorithm are described in [11].

2.4 Registrations and Coordinate Transformations

The goal of this system is to insert the needle into the target. The real-time transformation between the needle and the target can be calculated as following:

$$F_{T\arg et}^{Needle} = F_{Z-frame}^{Needle} \bullet F_{CT}^{Z-frame} \bullet F_{CTF}^{CT} \bullet F_{T\arg et}^{CTF} \tag{1}$$

where F_A^B represents a 4x4 homogeneous transformation matrix from the source coordinate system A to the target coordinate system B.

From the right of to the left of equation (1), $F_{T\arg et}^{CTF}$ contains the real-time position of the lesion with respect to the CTF imaging plane, obtained from the motion-tracking algorithm[11]; F_{CTF}^{CT} consists of the fixed translation from the origin of the frame grabbed CTF image to the origin of the preoperative CT volume, obtained from a translation registration (3-DOF) of a static rigid body in both images. Since the Z-frame is attached to the robot, $F_{CT}^{Z-frame}$ is a fixed transformation from the CT space to the robot space. The Z-frame contains three "Z"s that are formed by seven radiolucent fiducial rods located at known positions. As shown in figure 2, a single cross sectional CT image allows the rigid-body transformation between the CT and the Z-frame to be determined[7]. $F_{Z-frame}^{Needle}$ is the fixed transformation from the Z-frame to the needle space.

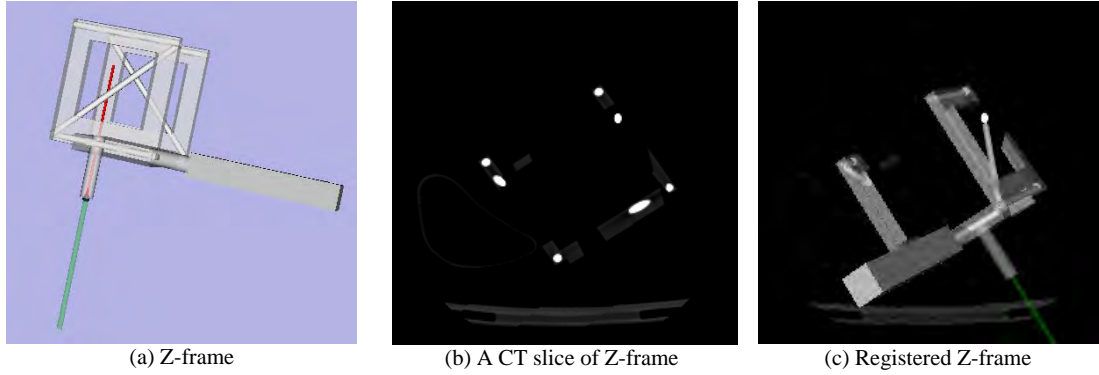| (a) Z-frame | (b) A CT slice of Z-frame | (c) Registered Z-frame |

Figure 2: Registration of Z-frame to CT

Since the RCM and Cartesian stages are connected by a passive arm, they need to be registered to the CT space separately. The RCM is registered through the attached Z-frame. Since the Cartesian stage is rigidly attached to the CT table using a curved mount and nylon straps, (figure 3.a), it is considered to be aligned with coordinate system of the CT scanner. This assumption is reasonable because respiratory motion is limited to a few centimeters. In such a small motion range, the motion error of the robot introduced by any misalignment of the Cartesian stage and CT table is negligible. To move the needle from its current needle position to the target position, the motion of the robot can be calculated from $F_{T\arg et}^{Needle}$ and the inverse kinematics of the robot.

2.5 Compensation for the Motion of Target Lesion

To compensate for the motion of the target lesion, a control loop is executed in the software. The needle is retracted from the RCM center to avoid any potential collision with the patient during the tracking. The following steps are executed inside the loop:

1. Process the CTF image to obtain the real-time position of the target lesion.
2. Update the biopsy path using the result of motion tracking.
3. Apply the inverse kinematics of the robot to update the needle pose according to the new path.

This is a typical control strategy that combines the visual sensing and manipulation in an open loop fashion, "looking then moving"[5], in which the CTF is the camera or the eye fixed on the ground. As a prototypical system, the skin entry point is currently assumed to be independent from respiration. Therefore, only the needle orientation needs to be updated to compensate for respiratory motion. In reality, the motion of the skin entry point may not be negligible. Although both the hardware and software of the system are capable of compensating for the lesion's motion in nearly real-time, for safety reasons, we envision that in any clinical use the needle will be manually inserted by the physician after the needle is aligned. Particularly in lung biopsy, automatic needle insertion using robot may increase the chance of pneumothorax. Therefore, the patient is asked to hold his or her breath during the insertion to avoid potential needle bending. The needle's position is automatically adjusted only before it enters the patient.

3.   EXPERIMENTS AND RESULTS

To test the system's performance, both phantom and swine studies were conducted at Georgetown University Medical Center on a Siemens Volume Zoom CT/CTF scanner. The frame rate of the CTF scans was 6 Hz.

3.1 Phantom Study

The accuracy of the system was evaluated in a phantom study using a respiratory motion simulator. Since the motion-tracking algorithm relies heavily on the texture of the lung, we developed a lung phantom with similar texture information. The phantom was made from seashells and rice packaged in a tennis ball container as shown in figure 3.b. The phantom was mounted on a 3D translational stage which held the phantom on the CTF scan plane and could be computer controlled to simulate any motion pattern. This 3D translational stage was originally developed to serve as a respiratory motion simulator during CyberKnife radiotherapy motion compensation experiments[12].
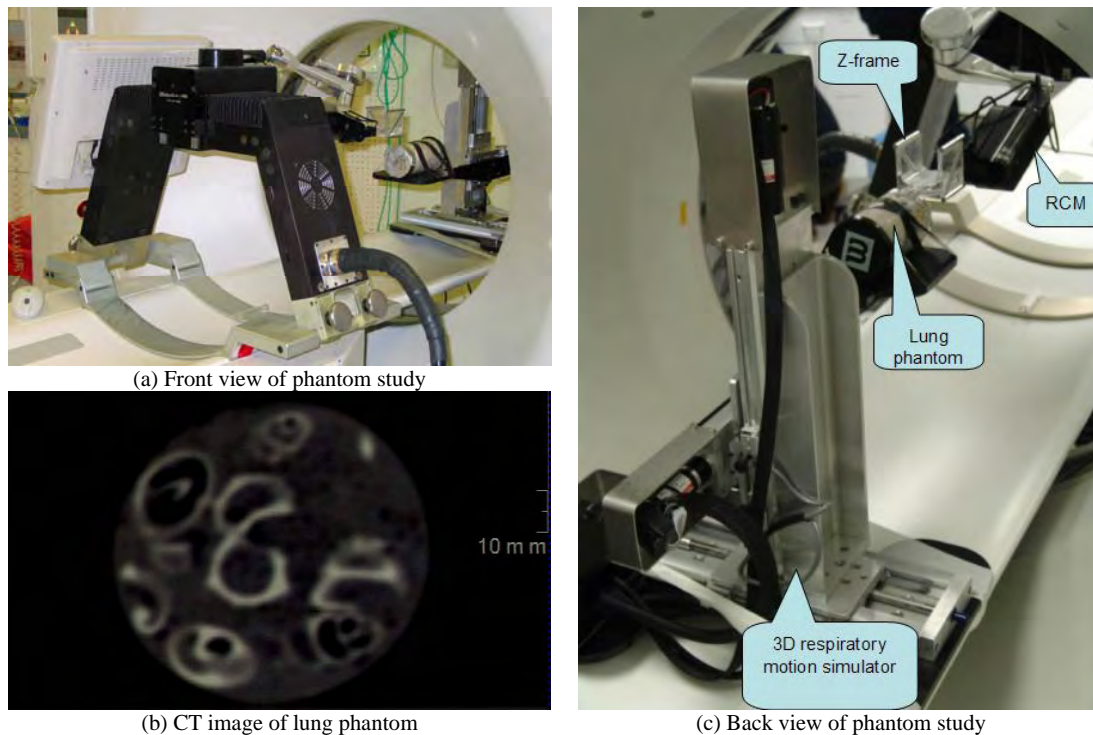

(a) Front view of phantom study

(b) CT image of lung phantom

(c) Back view of phantom study

Figure 3: Phantom study

Before the experiments, the motion simulator was manually aligned with the CT table. Several 1 mm fiducials were attached to the surface of the phantom. The phantom was CT scanned with a 1 mm slice thickness and 0.74 mm pixel size. A fiducial on the phantom surface was selected as the needle target. The needle entry point was selected to be in the air above. After the system was initialized, the phantom was moved by the respiratory motion simulator from its original position to some other known position. A CTF image at the new position was obtained. The frame grabbed CTF image was processed to obtain the position of the target lesion. The robot then moved, aligned and drove the needle to the target. The difference between the target and the final robot position was measured to obtain the accuracy of the system.

To measure the system error, the encoders of the robot were used as a precision measuring device. The robot was manually moved using its translational stage until the needle tip touched the target fiducial. The amount the robot had to be moved was recorded as the system error as shown in Table 1. The tracking error was also estimated in this study by comparing the motion amplitude detected by the tracking algorithm to the programmed amplitude (Table 1).

Table 1: Experimental Results

Parameter Measured	Number of Trials	Average Error	Variance of Error
System error	10	1.7 mm	0.5 mm
Tracking error	10	0.4 mm	0.3 mm

Although the motion in the above study was not continuous, comparable results were observed in another study under continuous phantom motion. As shown in figure 4, the respiratory motion simulator was commanded to move in sinusoid curves along the three principal axels simultaneously. Since no synchronization was used in the study, the results of motion tracking were fit to the ground truth of the programmed motion.
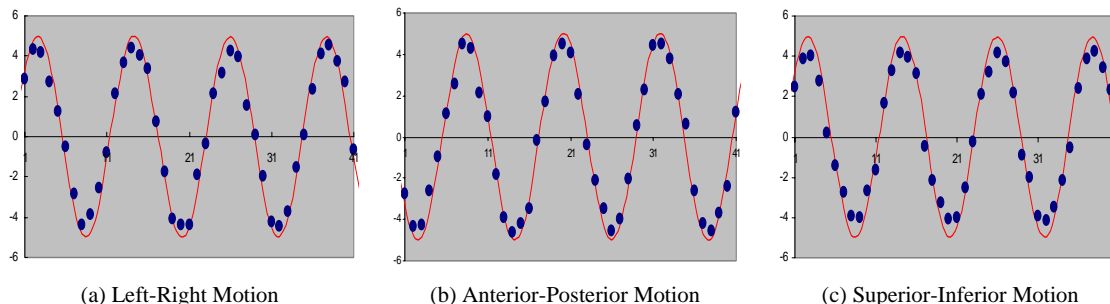

(a) Left-Right Motion (b) Anterior-Posterior Motion (c) Superior-Inferior Motion

Figure 4: Results (blue dots) of motion tracking in mm. Red lines are the ground truth.

3.2 Swine Study

The system was also tested in animal studies under an approved animal care protocol, with endotracheal intubation and under general anesthesia. A 3D CT scan was taken with the ventilator held in end respiratory phase of the tidal volume breathing cycle. To avoid the risk of inducing a pneumothorax and compromising the animal, no fiducial markers was implanted in the lung. Instead, an anatomical location of the lung was identified in the CT volume as the target point. During the treatment, the swine was mechanically ventilated. The CTF images were used to track the motion of the target point. At a certain respiratory phase, the ventilator was stopped to simulate the breath holding of the swine. The end-effector was aligned based on the motion-tracking algorithm; then, the needle was pushed into the lung by hand. Figure 5.a shows one of the animal studies. Figure 5.b shows the planned path in the preoperative CT volume, and figure 5.c shows the actual needle path. Although there was no numerical ground truth to validate the needle insertion, good correspondence between the two paths was observed from the images, meaning that the system was able to accurately align the needle. While this is just a preliminary result, this gives us confidence that the system can track the respiratory motion of the lung, and further animal studies are planned.
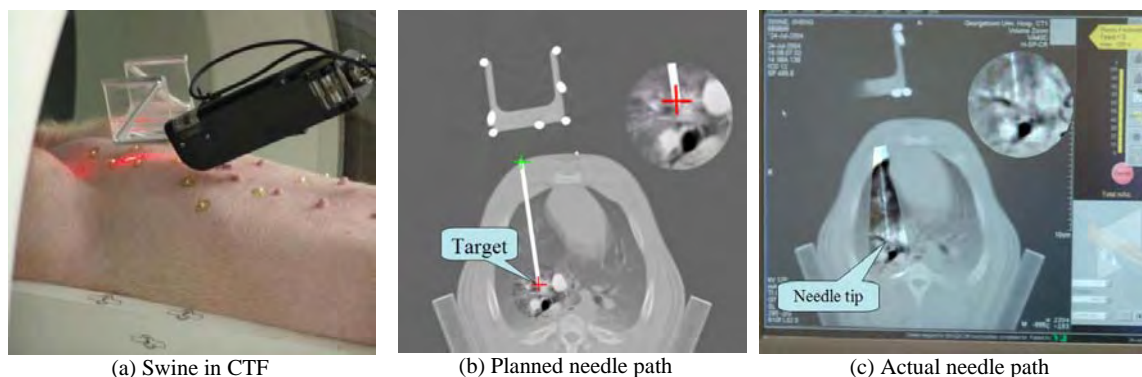

(a) Swine in CTF (b) Planned needle path (c) Actual needle path

Figure 5: Swine study

4. CONCLUSION AND DISCUSSION

In this paper, we presented the feasibility of using an image-guided surgical robot to assist lung biopsy. The system integrates a real-time non-invasive tracking algorithm to detect the motion of a pulmonary lesion. An open-loop control is used to automatically compensate for the target's motion. Initial experimental results showed that the biopsy system worked well with a respiratory motion simulator and had reasonable performance in a swine study. There are currently no other published systems for noninvasive real-time motion compensation of pulmonary tumors.

While the experiments validated the overall system concept, several weaknesses were identified that need to be addressed. First, we did not achieve a sufficient working volume, due to interference among the relatively large Z-frame, the RCM and the patient. We could not reach all clinically significant locations in the phantom and swine studies, especially considering oblique angles. The robot's passive arm had to be very carefully manipulated to ensure that not only the Z-frame stayed in the CTF filed of view but also the RCM didn't collide on the patient. Therefore, the RCM and the Z-frame need to be redesigned to allow for more clearance for the robot during needle placement. Second, the robot was rather sluggish in following the target's motion. We must note, however, that typical surgical robots are not supposed to perform quick motions, in order to reduce potential injury to the patient. Finally, the motion-tracking algorithm is only accurate when the target is close to the CTF imaging plane[13]. The algorithm is not robust for lung regions that don't have enough texture.

In addition to improving the tracking algorithm's robustness and accuracy, future work will include developing a new needle driver so that the needle can be automatically released from the needle driver once the needle has reached the desired position[14]. As a safety feature, it would also be desirable to integrate force sensing in the needle driver so that the needle could be released when abrupt motion of the patient is detected by processing real-time CTF image. Finally, the real-time needle position can also be obtained by tracking the Z-frame in the CTF image. Using a method such as visual servoing, the needle position can be automatically detected and used to adjust the needle's pose with respect to the target lesion. The control loop of the system can then be closed, which is called "dynamic look-and-move"[7].

ACKNOWLEDGEMENT

REFERENCES

1. K. Cleary, M. Mulcahy, R. Piyasena, T. Zhou, S. Dieterich, S. Xu, K. Wong, "Organ motion due to respiration: the state-of-the-art and applications in interventional radiology and radiation oncology", Proc. *SPIE: Visualization, Image-Guided Procedures and Display, Medical Imaging*, vol. 5744, pp. 53-9, 2005.
2. D. Gianfelice, L. Lepanto, P. Perreault, C. Chartrand-Lefebvre, and P. C. Milette, "Value of CT fluoroscopy for percutaneous biopsy procedures," J Vasc Interv Radiol, vol. **11**, pp. 879-84, 2000.
3. E. M. Law, A. F. Little, and J. C. Salanitri, "Non-vascular intervention with real-time CT fluoroscopy," Australas Radiol, vol. **45**, pp. 109-12, 2001.
4. D. Stoianovici, L. L. Whitcomb, J. H. Anderson, R. H. Taylor, and L. R. Kavoussi, "A Modular Surgical Robotic System for Image-Guided Percutaneous Procedures," *MICCAI*: *Lecture Notes in Computer Science*, vol. 1496, pp. 404-410, Springer-Verlag, 1998.
5. R. H. Taylor, P. Jensen, L. Whitcomb, A. Barnes, R. Kumar, D. Stoianovici, P. Gupta, Z. Wang, E. deJuan, and L. Kavoussi, "A Steady-Hand Robotic System for Microsurgical Augmentation," International Journal of Robotics Research, vol. **18**, no. 12, pp. 1201-1210, Dec. 1999.

6. J. Hong, T. Dohi, M. Hashizume, K. Konishi, N. Hata: "An Ultrasound-driven Needle Insertion Robot for Percutaneous Cholecystostomy" , Physics in Medicine and Biology, Vol.49, No.**3**, pp.441-455, 2004.
7. M. Loser and N. Navab, "A new robotic system for visually controlled percutaneous interventions under CT Fluoroscopy," *MICCAI*: *Lecture Notes in Computer Science*, vol. 1935, pp 887-896, Springer Verlag, 2000.
8. B. Bascle, N. Navab, M. Loser, B. Geiger, R. Taylor, "Needle placement under X-ray fluoroscopy using perspectiveinvariants", Mathematical Methods in Biomedical Image Analysis, pp. 46-53, 2000.
9. R. C. Susil, J. H. Anderson, R. H. Taylor, "A Single Image Registration Method for CT-Guided Interventions," *MICCAI*: *Lecture Notes in Computer Science*, vol. 1679, pp. 798-808, Springer-Verlag, 1999.
10. D. Stoianovici, K. Cleary, A. Patriciu, D. Mazilu, A. Stanimir, N. Craciunoiu, V. Watson, and L. R. Kavoussi, "AcuBot: a robot for radiological interventions," IEEE Transactions on Robotics and Automation, vol. **19**, pp. 927-930, 2003.
11. S. Xu, G. Fichtinger, R. H. Taylor, and K. R. Cleary, "3D motion tracking of pulmonary lesions using CT fluoroscopy images for robotically assisted lung biopsy," Proc. *SPIE: Visualization, Image-Guided Procedures and Display, Medical Imaging*, vol. 5367, pp. 394-402, 2004.
12. T. Zhou, J. Tang, S. Dieterich, and K. Cleary, "A robotic 3-D motion simulator for enhanced accuracy in CyberKnife stereotactic radiosurgery," *Computer Aided Radiology and Surgery (CARS)*, pp. 323-328, Elsevier, 2004.
13. S. Xu, G. Fichtinger, Lindisch D, K. Cleary, "Validation of 3D Motion Tracking of Pulmonary Lesions for Image-Guided Lung Biopsy," Proc. *SPIE: Visualization, Image-Guided Procedures and Display, Medical Imaging*, Vol. 5744, pp. 60-68, 2005.
14. I. Iordachita, R. Wiard, G. Fichtinger, I. Sakuma, and D. Stoianovici, "Controllable motorized devices for accurate percutaneous needle placement in soft tissue target," *the 11th World Congress in Mechanisms and Machine Science*, pp. 82-86, 2004.

8.9 Yaniv 2006a: Realistic Simulation Framework …

Reprint begins on the next page and is eight pages.

A realistic simulation framework for assessing deformable slice-to-volume (CT-fluoroscopy/CT) registration

Ziv Yaniv[a], Roland Stenzel[a,b], Kevin Cleary[a], and Filip Banovac[a,c]

[a]Imaging Science and Information Systems (ISIS) Center, Dept. of Radiology,
Georgetown University Medical Center, Washington, DC,USA
[b]University of Karlsruhe, Institut für Technische Informatik - IAIM, Karlsruhe, Germany
[c]Georgetown University Hospital, MedStar Health, Washington, DC, USA

ABSTRACT

Lung cancer screening for early diagnosis is a clinically important problem. One screening method is to test tissue samples obtained from CT-fluoroscopy (CTF) guided lung biopsy. CTF provides real-time imaging; however on most machines the view is limited to a single slice. Mentally reconstructing the direction of the needle when it is not in the imaging plane is a difficult task. We are currently developing 3D visualization software that will augment the physician's ability to perform this task. At the beginning of the procedure a CT scan is acquired at breath-hold. The physician then specifies an entry point and a target point on the CT. As the procedure advances the physician acquires a CTF image, at breath-hold; the system then registers the current setup to the CT scan, enabling comparison between the plan and current situation. As the CT and CTF data are acquired at different breath-holds we expect them to exhibit displacements of up to 4mm. To assess the performance of different registration algorithms for CTF/CT registration we propose to use simulated CTF images. These images are created by deforming the original CT volume and extracting a slice from it. Realistic deformation of the CT volume is achieved by using positional information from electromagnetically tracked fiducials, acquired throughout the respiratory cycle. To estimate the dense displacement field underlying the sparse displacement field provided by the fiducials we use radial basis function interpolation. Finally, we evaluated Thirion's "demons" algorithm, as implemented in ITK, for the task of slice-to-volume registration. We found it to be unsuitable for this task, as in most cases the recovered displacements were less than 50% of the original ones.

Keywords: Image-Guided Therapy, CT-Fluoroscopy, deformable registration, simulated respiration, radial basis functions

1. INTRODUCTION

Lung cancer is a leading cause of death in the United States with an overall cure rate (five year survival) of only about 15%.[1] Lung cancer screening has the potential of leading to early diagnosis and treatment, thus increasing chances of survival.[2] One screening method is to test tissue samples obtained from CT-Fluoroscopy (CTF) guided lung biopsy.

The outcome of this approach is highly dependent on the ability of the physician to accurately place the biopsy needle within the suspected nodule based on the CTF images. CTF provides the physician with real-time imaging, however on most machines it is limited to a single slice. Mentally reconstructing the direction of the needle, when it is not in the imaging plane, using a single slice as feedback can be a difficult task, even for experienced physicians.

We are currently developing 3D visualization software that may augment the physician's ability to perform this task. The system works as follows. At the beginning of the procedure a CT scan is acquired at breath-hold. The physician then specifies an entry point and a target point on the CT. As the procedure advances, the physician acquires a CTF image at breath-hold; the system then registers the current setup to the CT scan, enabling comparison between the plan and current situation. As the CT and CTF data are acquired at different breath-holds we need to deformably register them.

E-mail: {zivy,stenzel,cleary}@isis.georgetown.edu

As the whole system depends on accurate CTF/CT registration we first need to evaluate the performance and limitations of different deformable registration algorithms. We propose to use a simulation framework for respiratory based motion, allowing us to validate registration results with regard to a known transformation. To simulate a CTF image we extract a slice from a second volumetric data set whose transformation with regard to the original volume is known. Three possible methods to obtain a second volumetric data set with known deformations are: (1) Ad-hoc methods; (2) Registration based methods; and (3) Finite element methods (FEM).

Ad-hoc methods receive as input a volumetric data set and a sparse displacement field describing the deformation. They output a dense displacement field and a corresponding deformed volume. The sparse displacement field is generated by manually displacing a small number of points. The points are usually anatomical landmarks with the displacement field generated via interpolation[3] or approximation.[4] Points may also be the intersections of a regular grid that overlaps the image with the displacement field generated via free-form deformations.[5] The popularity of this approach is due to its simplicity, and that it does not require additional data (i.e. only the original volume is required). Unfortunately, as the approach is not constrained, physically impossible deformations are easily generated.

Registration based methods receive as input multiple volumetric data sets under different deformations. They output a dense displacement field describing the deformation between pairs of volumes.[6,7] This approach does not incorporate bio-mechanical knowledge, but works well if the deformation between the registered data sets is smooth. Applying this approach to structures that deform considerably requires acquisition of multiple data sets throughout the deformation process (e.g. a set of MRI volumes acquired between end expiration and end inspiration). Note that using the displacement field generated by this approach as a gold standard can be biased if the same algorithm is used for volume-to-volume and slice-to-volume registrations.

Finite element methods receive as input a volumetric data set, a segmentation of the anatomical structures according to the different tissue types, and the bio-mechanical properties of the tissue types. They output a dense displacement field and a corresponding deformed volume. These methods have have been studied extensively, mainly in the context of surgical simulation,[8,9] and registration.[10,11] This approach is considered the most physically accurate, and has been used to validate free-form registration of mammographic MRI data.[12]

Our approach to simulating deformation due to respiratory motion can be classified as a constrained version of the ad-hoc approach. We deform the original volumetric data based on the motion of a sparse set of points, electromagnetically tracked fiducials, which are acquired from organ motion of a respiring animal. As is the case with the ad-hoc approach, computing the deformation is still an under-constrained problem. The difference is that now the deformations are driven by physical measurements and not arbitrary displacements. Figure 1 classifies the different approaches according to their computational complexity and physical realism.

Similar approaches to our own have been recently described in the context of real-time deformation update of a CT volume.[13,14] Both papers estimate deformations of small volumes using electromagnetically tracked fiducials. In[13] the deformation field is obtained using a variational approach, with a regularization term that enforces smoothness. No quantitative results are given and the weighing of the regularization term is unspecified. In[14] the deformation is assumed to be affine which is plausible for very small volumes.

Computational Complexity

low ⟶ high

ad hoc   our method   registration based   FEM

non ⟶ realistic
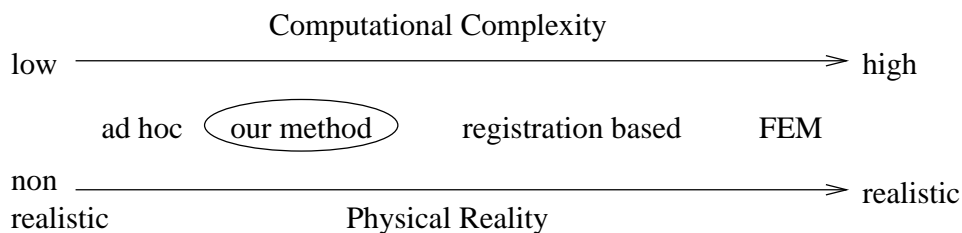realistic   Physical Reality

Figure 1. Classification of approaches for creating a ground truth displacement field and deformed volumetric data set.

2. MATERIALS AND METHODS

To assess the accuracy of deformable slice-to-volume (CTF/CT) registration we have developed a simulation based framework for respiratory based motion, providing a ground truth to which registration results can be compared. Our method is based on simulating CTF images using a CT scan acquired at end expiration that is deformed according to data obtained from electromagnetically tracked fiducials.

2.1. Data simulation

Simulating CTF images at different stages of the respiratory cycle is a four step process: (1) Acquire a CT scan and positional information from electromagnetically tracked fiducials; (2) Compute a deformation field based on the electromagnetic tracking data, and segment the lung region in the CT. (3) Deform the original volume in the region of the lungs using the segmentation and deformation field from the previous step. (4) Extract a slice from the deformed volume, this is our simulated CTF image.

Data acquisition proceeds as follows. First, four magnetically tracked fiducials are placed in the animal's liver (Fig. 2(a)), under an approved protocol, and a CT is acquired at end expiration. Then the animal is transferred to an environment where there are no ferromagnetic materials and positional data from the fiducials is acquired throughout several respiratory cycles. CT acquisition is performed at end expiration to ensure that there are no motion artifacts during imaging. In our setup the animal is on a respirator and we allow its lungs to deflate prior to imaging. The needles were placed in the liver instead of the lungs, as placing them in the lungs may result in a pneumothorax (Fig. 2(b)). This is a condition where air collects in the space surrounding the lungs causing them to collapse.

Deformation field computation is based on the known motion of fiducials inside the volume. This data is used to estimate the motion of all points in the volume, using radial basis function interpolation. As a pre-processing step we need to orient the electromagnetic system's coordinate frame with the CT coordinate frame (Fig. 2(c)). When three or more needles are used we compute the orientation using rigid registration.[15] If less than three needles are used we obtain the orientation by analyzing their motion pattern using principle component analysis. We transform the motion data to the coordinate system defined by the principle components and identify the main direction of motion with the CT's z axis (cranial-caudal), and the direction with least motion with the CT's x axis (left-right). This identification is based on the assumption that maximal motion is in the cranial-caudal direction and least motion is in the left-right direction. Finally, the initial positions of the needles are translated so that they are inside the lung region.

Once the data is oriented and translated we have the motion of the tracked fiducials, in the CT coordinate system, throughout the respiratory cycle. For different points in time we have corresponding vectors specifying the fiducial displacement from its initial location. This allows us to compute deformation fields corresponding to different points in the respiratory cycle. The fields are computed using radial basis functions with the input being the original point locations, and corresponding displacements.

In general the radial basis function interpolator is of the form:

$$s(\mathbf{x}) = p(\mathbf{x}) + \sum_{i=1}^{n} \lambda_i \phi(\|\mathbf{x} - \mathbf{x_i}\|)$$

where $p(\mathbf{x})$ is a polynomial that ensures the invertibility of the associated set of linear equations, λ_i are real coefficients, $\phi : \mathbb{R}^+ \to \mathbb{R}$ is the basis function, and $\mathbf{x_i} \in \mathbb{R}^d$ are the interpolation points such that $s(\mathbf{x_i}) = f_i$. In our case $\mathbf{x_i}$ are the fiducial locations at end expiration, and f_i are the corresponding translations in the x, y and z directions.

The radial basis function we use is a Gaussian, $\phi(r) = e^{-cr^2}, c > 0$, as it guarantees the existence of a solution without any restrictions on the spatial location of the known points.[16] This eliminates the need for the polynomial term $p(\mathbf{x})$ giving a linear equation system with a symmetric positive definite matrix $A_{ij} = \phi(\|\mathbf{x_i} - \mathbf{x_j}\|)$:

$$A \begin{bmatrix} \lambda_1 \\ \vdots \\ \lambda_n \end{bmatrix} = \begin{bmatrix} f_1 \\ \vdots \\ f_n \end{bmatrix}$$
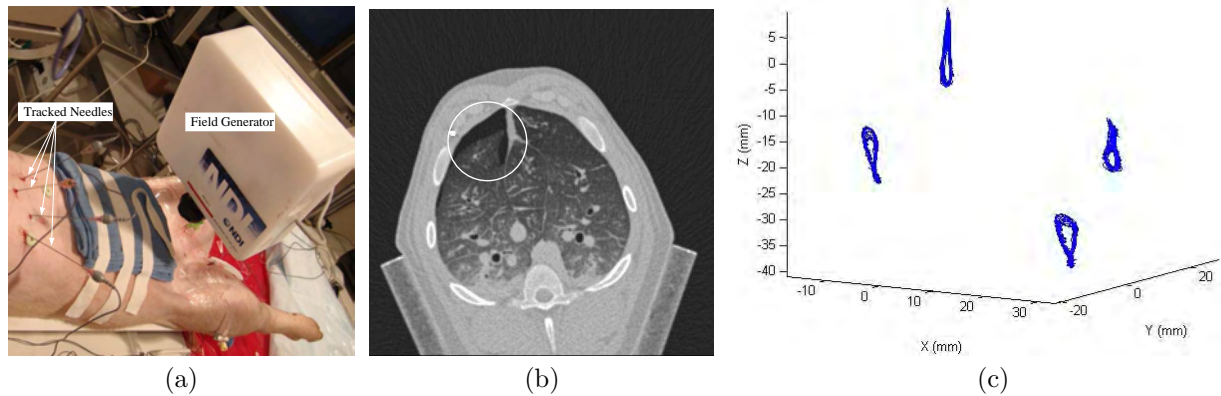
(a)   (b)   (c)

Figure 2. Electromagnetic tracking data acquisition: (a) needles placed in animals' liver; (b) circle marks pneumothorax caused by a needle inserted into the animal's lung; and (c) tracking data acquired throughout several breathing cycles oriented to the CT coordinate system (x axis is left-right, y axis is anterior-posterior, and z axis is cranial-caudal).

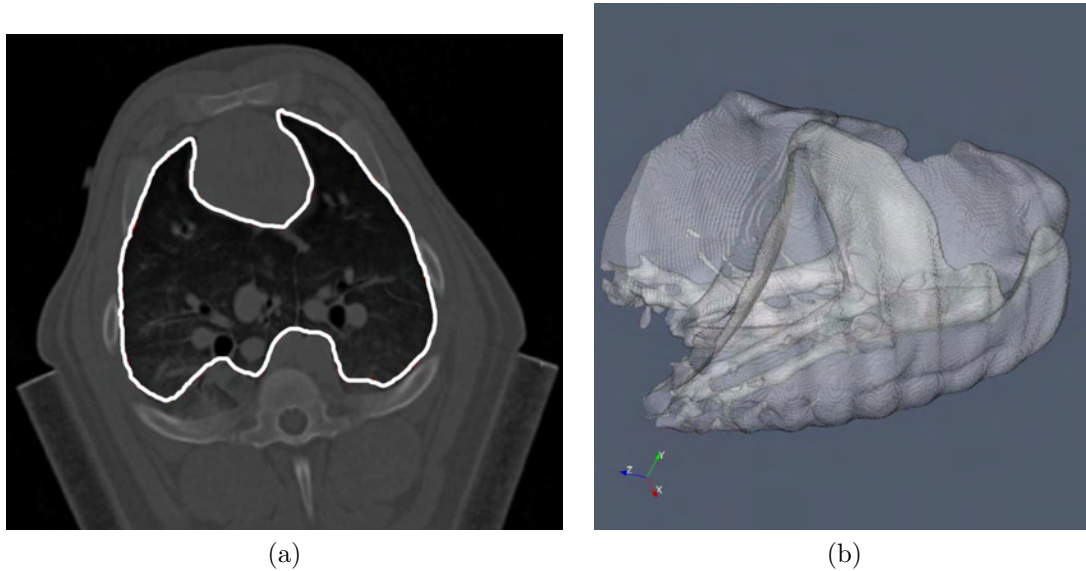(a)   (b)

Figure 3. Segmentation of lung region from CT data set (a) slice and (b) volume rendering of segmented region.

Generally, the use of radial basis functions with infinite support is viewed as a deficiency, as each interpolation point influences the function approximation at all locations. In our case, as we are dealing with a very small number of interpolation points, we do want them to effect the function evaluation throughout the volume. By choosing a Gaussian as our basis function each interpolation point effects the whole volume while at the same time its influence diminishes as a function of the distance.

This most likely yields an inaccurate approximation of the underlying function, mainly due to the spatial sparseness of the sampling, but it is still plausible as assessed by visual inspection. Additionally deformation sizes are limited to reasonable ones. This is achieved by empirically setting the Gaussian's standard deviation to values such that the estimated motion is smaller than 1.5 times the maximal known motion from electromagnetic tracking.

Finally, as we are only interested in the region of the lungs we segment them both in the CTF and CT images so that the resulting images include only the region of interest. The deformation field is then limited to this region. Segmentation of the lungs is done by first blurring the images using a Gaussian kernel with a standard
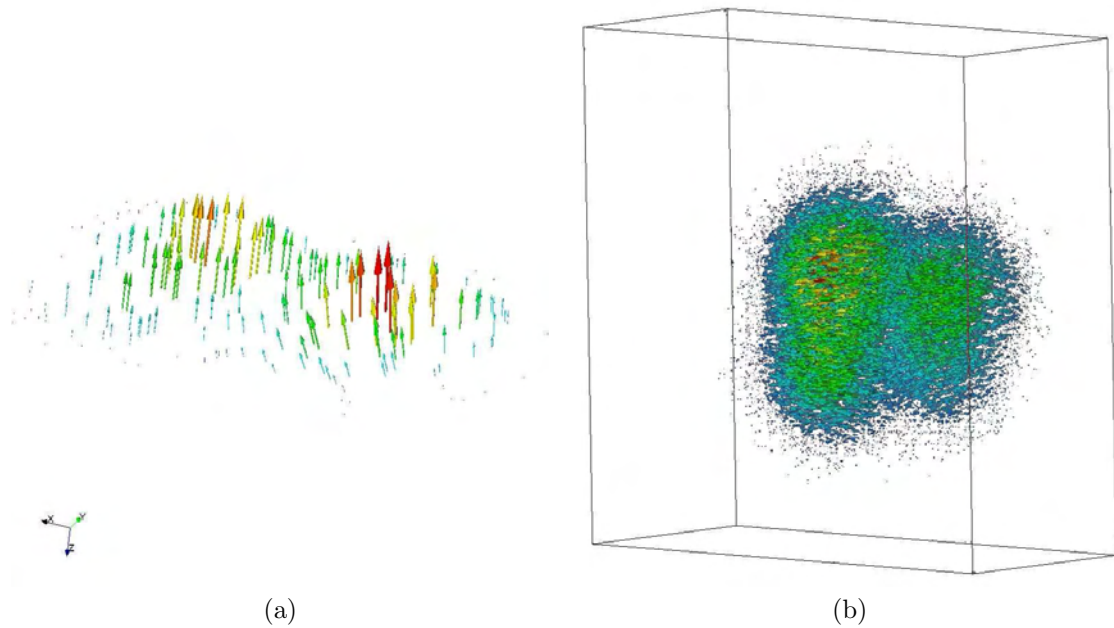
(a)   (b)

Figure 4. Deformation field limited to region of the lungs (a) single slice, and (b) whole field.

deviation of $2mm$, and then applying a threshold based region growing method. Seed points are placed in the left and right lungs and all voxels whose intensity is less than the threshold (0 HU) are considered as part of the lung. This approach is viable, as there is a clear intensity boundary between the lungs and the surrounding tissue (Fig. 3). In our case, segmentation accuracy is not an issue, as the results are only used as a region of interest. Fig. 4 is an example of the final deformation field limited to the region of the lung.

3. EXPERIMENTAL RESULTS

In all experiments CT images were acquired using a Siemens Somatom Volume Zoom machine, with slice resolution of 512X512 and pixel spacing of $0.61X0.61mm$ and $1mm$ slice spacing. Electromagnetic data was acquired using MagTrax needles from Traxtal Technologies (Belaire, Texas, USA), and the Aurora electromagnetic tracking system from Northern Digital Inc. (Ontario, Canada). Acquisition rate of the tracking data was 25Hz.

CT and electromagnetic data were acquired in two swine animal studies, under an approved protocol, and used to simulate seven CTF images per data set. As both the CT and CTF images are acquired with similar breath-holds, we expect the two acquisitions will exhibit small deformations of up to $4mm$. Simulated CTF images were generated accordingly, with deformations in the range 0.4–4.2mm.

The CT data and simulated images were then used to assess the capabilities of Thirion's "demons" algorithm,[17] as implemented in ITK,[18] to perform slice-to-volume deformable registration. This algorithm is an optical flow based method, most notably it assumes that the constant brightness constraint[19] is satisfied, that is, a point's intensity does not change between images. In the case of CTF/CT registration this assumption is indeed satisfied.

Two factors that can effect the convergence range of the registration process are its initialization, and the size of the displacements that we are trying to recover. In our case CT and CTF images are different modes of operation of the same machine, so their coordinate systems are intrinsically aligned. This allows us to use the slice location of the CTF image as our initial transformation, an approach we also apply in our simulation studies. The size of the displacements we are trying to recover is relatively small, less than $4mm$, but it varies with the slice location in the lung. To assess the effect of slice location, for each simulated deformation we registered four slices from lung apex to diaphragm, as shown in Figure 5.
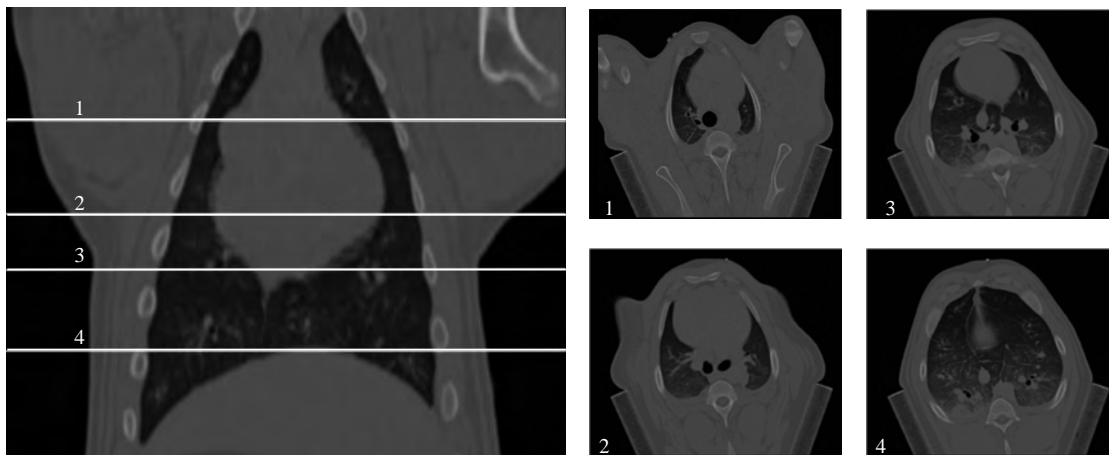
Figure 5. To assess the registration performance for different regions of the lung we register four different slices from apex (1) to diaphragm (4).
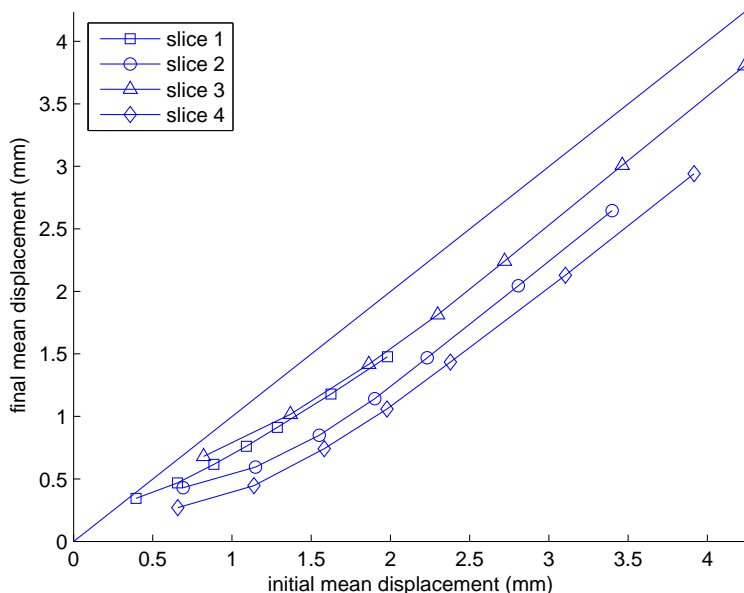

Figure 6. Registration results using slices from different locations in the lung. Slices correspond to those in Fig. 5, and are ordered from apex (1) to diaphragm (4). Results are below the diagonal, indicating that the algorithm was able to reduce the original displacements. However, the accuracy of the final results is not sufficient for our application.

In all our experiments the "demons" algorithm failed to converge to the global optimum. The results of our experiments are summarized in Figure 6. In all experiments the algorithm was able to reduce the initial displacements, results are below the diagonal indicating decrease in the mean displacement. Unfortunately, in most cases the final recovered displacements are less than 50% of the original ones.

4. DISCUSSION AND CONCLUSIONS

We have presented a simple method for simulating soft tissue deformation. The method estimates the deformation based on a small set of landmarks whose displacement is precisely known. Although the resulting deformations

are not physically accurate, they are still plausible ones, and are generally more accurate than deformations generated by manual methods.

In this work positional data of internal points was obtained via electromagnetic tracking. In general, our approach does not require an electromagnetic tracking system. Other options include the use of rigid needles and optical tracking, or the use of fiducials and bi-plane fluoroscopy to track internal organ motion throughout the respiratory cycle.[20]

Finally, we have assessed the performance of Thirion's "demons" algorithm, as implemented in ITK, for slice-to-volume registration using our simulation framework. According to our experiments using this algorithm for deformable slice-to-volume registration does not yield satisfactory results.

Although deformable slice-to-volume is an ill posed problem we initially expected the "demons" algorithm would be able to recover the correct displacements as they are relatively small (less than $4mm$). Given our results we will investigate the possibility of acquiring multiple (two or three) CTF images at different slice positions instead of a single CTF image. This will change our registration approach from slice-to-volume to volume-to-volume. As the volume-to-volume approach incorporates more information it is better conditioned and has a better chance of recovering the correct deformations.

ACKNOWLEDGMENTS

REFERENCES

1. "American cancer society: Cancer facts and figures," 2004.
2. O. S. Miettinen, "Screening for lung cancer," *Radiol. Clin. North. Am.* **38**(3), pp. 479–486, 2000.
3. F. L. Bookstein, "Principal warps: Thin-plate splines and the decomposition of deformations.," *IEEE Trans. Pattern Anal. Machine Intell.* **11**(6), pp. 567–585, 1989.
4. K. Rohr, H. S. Stiehl, R. Sprengel, T. M. Buzug, J. Weese, and M. H. Kuhn, "Landmark-based elastic registration using approximating thin-plate splines.," *IEEE Trans. Med. Imag.* **20**(6), pp. 526–534, 2001.
5. D. Rueckert, L. I. Sonoda, C. Hayes, D. L. G. Hill, M. O. Leach, and D. J. Hawkes, "Non-rigid registration using free-form deformations: Application to breast MR images.," *IEEE Trans. Med. Imag.* **18**(8), pp. 712–721, 1999.
6. D. J. Hawkes *et al.*, "Tissue deformation and shape models in image-guided interventions: a discussion paper," *Medical Image Analysis* **9**(2), pp. 163–175, 2005.
7. T. Rohlfing, C. Maurer, Jr., W. G. O'Dell, and J. Zhong, "Modeling liver motion and deformation during the respiratory cycle using intensity-based free-form registration of gated MR images," *Medical Physics* **31**(3), pp. 427–432, 2004.
8. H. Delingette, "Towards realistic soft tissue modeling in medical simulation," *Proceedings of the IEEE : Special Issue on Surgery Simulation* , pp. 512–523, 1998.
9. J.-M. Schwartz, M. Denninger, D. Rancourt, C. Moisan, and D. Laurendeau, "Modelling liver tissue properties using a non-linear visco-elastic model for surgery simulation," *Medical Image Analysis* **9**(2), pp. 103–112, 2005.
10. K. E. Lunn, K. D. Paulsen, D. W. Roberts, F. E. Kennedy, A. Hartov, and L. A. Platenik, "Nonrigid brain registration: synthesizing full volume deformation fields from model basis solutions constrained by partial volume intraoperative data," *Computer Vision and Image Understanding* **89**, pp. 299–317, 2003.
11. M. Ferrant, S. K. Warfield, A. Nabavi, F. A. Jolesz, and R. Kikinis, "Registration of 3d intraoperative MR images of the brain using a finite element biomechanical model.," in *Medical Image Computing and Computer-Assisted Intervention*, pp. 19–28, 2000.
12. J. A. Schnabel, C. Tanner, A. D. Castellano-Smith, A. Degenhard, M. O. Leach, D. R. Hose, D. L. G. Hill, and D. J. Hawkes, "Validation of non-rigid image registration using finite element methods: Application to breast MR images.," *IEEE Trans. Med. Imag.* **22**(2), pp. 238–247, 2003.

13. M. Vetter *et al.*, "Navigation aids and real-time deformation modeling for open liver surgery," in *SPIE Medical Imaging: Visualization, Image-Guided Procedures, and Display*, pp. 58–68, 2003.

14. H. Zhang, F. Banovac, N. Glossop, and K. Cleary, "Two-stage registration for real-time deformable compensation using an electromagnetic tracking device," in *Medical Image Computing and Computer-Assisted Intervention*, pp. 992–999, 2005.

15. B. K. P. Horn, "Closed-form solution of absolute orientation using unit quaternions," *Journal of the Optical Society of America A* **4**(4), pp. 629–642, 1987.

16. M. J. D. Powell, "The theory of radial basis function approximation in 1990," in *Advances in Numerical Analysis Volume II: Wavelets, Subdivision Algorithms and Radial Basis Functions*, W. A. Light, ed., Oxford University Press, 1992.

17. J. P. Thirion, "Image matching as a diffusion process: an analogy with maxwell's demons," *Medical Image Analysis* **2**(3), pp. 243–260, 1998.

18. L. Ibáñez, W. Schroeder, L. Ng, and J. Cates, *The ITK Software Guide*, Kitware Inc., 2005.

19. B. K. P. Horn and B. G. Schunck, "Determining optical flow," *Artificial Intelligence* **17**(1–3), pp. 185–203, 1981.

20. Z. Yaniv and K. Cleary, "Fluoroscopy based accuracy assessment of electromagnetic tracking," in *SPIE Medical Imaging: Visualization, Image-Guided Procedures, and Display*, 2006.

8.10 Yaniv 2006b: Fluoroscopy Based Accuracy …

Reprint begins on the next page and is seven pages.

Fluoroscopy based accuracy assessment of electromagnetic tracking

Ziv Yaniv and Kevin Cleary

Imaging Science and Information Systems (ISIS) Center, Dept. of Radiology, Georgetown University Medical Center, Washington, DC, USA.

ABSTRACT

Tracking organ motion due to respiration is important to enable precise interventions in the regions of the abdomen and thorax. Respiratory induced motion in these regions may limit the accuracy of interventions which do not employ some type of tracking. One method of tracking organ motion is to use a predictive model based on external tracking that is correlated to internal motion. This approach depends on the accuracy of the model used for correlating the two motions. Ideally, one would track the internal motion directly. We are investigating the use of electromagnetically tracked fiducials to enable real-time tracking of internal organ motion. To investigate the in-vivo accuracy of this approach we propose to use stereo-fluoroscopy. In this paper we show that stereo-fluoroscopy is accurate enough to serve as a validation method, displaying sub-millimetric accuracy (maximal error of 0.66mm). We study the effect of the bi-plane fluoroscopes on the electromagnetic systems' accuracy, and show that placing the bi-plane fluoroscopes in a typical intra-operative setup has a negligible effect on the tracking accuracy (maximal error of 1.4mm). Finally, we compare the results of stereo-fluoroscopy tracking and electromagnetic tracking of needles in an animal study, showing a mean (std) difference of 1.4 (1.5)mm between modalities. These results show that stereo-fluoroscopy can be used in conjunction with electromagnetic tracking with minimal effect, and that the electromagnetic system is accurate enough for motion tracking of internal organs.

Keywords: Image-Guided Therapy, localization, electromagnetic tracking, accuracy assessment

1. INTRODUCTION

Tracking target motion due to respiration is important for precise interventions in the regions of the abdomen and thorax. Respiratory induced motion in these regions can be up to several cm,[1,2] thus severely limiting the accuracy of interventions which do not employ some type of tracking. This is an important issue in radiotherapy procedures. The goal of these procedures is to irradiate a tumor while limiting the radiation delivered to adjacent normal tissue.[3–5] Internal organ tracking is also an issue in percutaneous procedures involving soft tissue, where the target is continuously moving. For example, different types of biopsies, where a needle must be inserted into a tumor, and the TIPS procedure,[6] where a needle is passed through two blood vessels inside the liver.

Two common methods for real-time respiratory induced motion tracking are direct observation,[3,7] and use of a surrogate signal which is correlated with the motion of the region of interest (ROI).[8,9] Direct observation methods track the ROI by using continuous imaging, usually X-ray radiography. These methods either track visible anatomical landmarks or implanted fiducials. Methods that use surrogate signals establish a correlation between the motion of the ROI as observed via imaging and other measures due to respiration, such as movement of the thorax and abdomen. Once the correlation is established the surrogate signal is used to predict the motion of the ROI.

Ideally one would use direct observation as it does not make assumptions with regard to the nature of the motion, while the use of a surrogate signal assumes systematic motion. This assumption does not always hold, and requires occasional validation by use of intra-operative imaging.[9] While direct observation is an ideal method of tracking it also has its limitations, mostly due to the employed modality, X-ray imaging. In many cases the delivered radiation dose due to imaging may be too high.[4] Another limitation to this approach is

---

E-mail: {zivy,cleary}@isis.georgetown.edu

its inability to work for extended periods of time. This is due to heating of the X-ray tube during the image acquisition process.

We are currently investigating the use of electromagnetically tracked fiducials, which will allow direct tracking without the need for X-ray imaging.[10] This approach will enable real-time tracking for extended periods of time without any assumptions with regard to the nature of the motion due to respiration.

To asses the in-situ accuracy of electromagnetic (EM) tracking we propose to use stereo-fluoroscopy, specifically a bi-plane fluoroscopic C-arm unit. The 3D measurements obtained by stereo-fluoroscopy will serve as our ground truth. This approach is motivated by previous studies[11] that have shown that the accuracy of stereo-fluoroscopy, after calibration, is sub-millimetric. EM tracking accuracy is then evaluated by simultaneously acquiring X-ray images from both C-arms and data from the tracking system, after which the data from both systems is compared.

A major concern in our approach is the effect of our observation method on the tracking accuracy, as it may degrade due to the proximity of the metallic C-arm frames. Previous studies[12] have concluded that placing a C-arm fluoroscopy unit near the EM tracking system causes considerable distortion ($18.66 \pm 24.9mm$). More recent studies[13, 14] conclude that EM tracking systems have improved their robustness to the presence of metallic objects, although they do not specifically test the effect of a C-arm unit.

This paper describes the proposed validation method and presents our experimental results. We assess the accuracy of EM tracking given a known motion, the effect of our observation method on the tracking accuracy, and we compare the in-vivo results obtained by stereo-fluoroscopy and EM tracking from a swine animal study.

2. MATERIALS AND METHODS

To use the bi-plane fluoroscopic C-arm unit for stereo reconstruction we need to calibrate each of the C-arms and to establish the spatial relationship between them.

We model each of the fluoroscopic C-arm units as a pinhole camera with geometric distortion, as this has been shown to be an appropriate approximation of the X-ray imaging process.[15, 16] An important aspect of C-arm calibration is that the camera parameters are orientation dependent. In our case, this does not pose a problem as we can calibrate the stereo pair in the predetermined setup that is used for data acquisition.

Calibrating each of the C-arms is a two step process, consisting of estimation of the geometric distortion followed by estimation of the camera internal and external parameters.[15, 16] To estimate the geometric distortion we acquire an image of a fiducial grid which is attached to the image intensifier of each of the C-arms. We then acquire an image of a calibration target from both C-arms simultaneously. This establishes the spatial relationship between the pair of C-arms, as their respective poses are computed relative to the same coordinate system. Once both C-arms are calibrated and their spatial relationship is established we apply the standard triangulation technique to reconstruct the 3D information.[17]

To compare between the 3D data obtained using the EM tracking system and the stereo-fluoroscopy we need to establish the spatial and temporal relationships between the data sets. To minimize the temporal difference between the data sets we try to start the data acquisition simultaneously. As this is done manually we cannot start data acquisition at exactly the same time. However, we can ensure that both data sets start on the same breathing cycle and have a temporal difference of less than two seconds between them.

As both data sets describe the same point motion in different coordinate systems we align them using a constrained iterative closest point (ICP)[18] approach. The constraint we add to the matching process enforces the known temporal order of the points. We also incorporate the knowledge that there is a shift of at most $k = 2$ seconds between data sets. Starting with the first point in one data set we search for the closest point in the other data set among all points which were acquired in the first k seconds. From here on the search for the next match is constrained to the set of points in the k second interval starting at the previously matched point.

In all our experiments we used a Siemens Neurostar bi-plane fluoroscopy unit, with an image resolution of 1024×1024, the Aurora EM tracking system from Northern Digital Inc. (Ontario, Canada), and MagTrax needle probes from Traxtal Technologies (Belaire, Texas, USA) were used as fiducials. The calibration target used for stereo calibration is built of Delrin and consists of 36 stainless steel fiducial spheres distributed on two planes $70mm$ apart (Fig. 1).
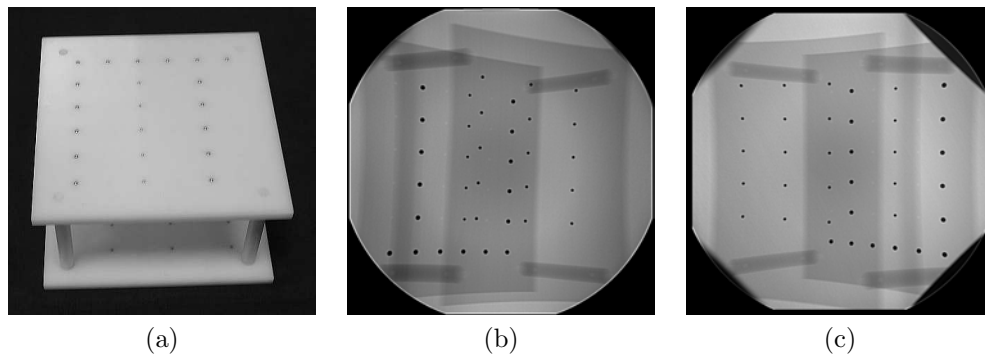
(a)   (b)   (c)

Figure 1. (a) Calibration target and (b),(c) pair of stereo-fluoroscopy images.

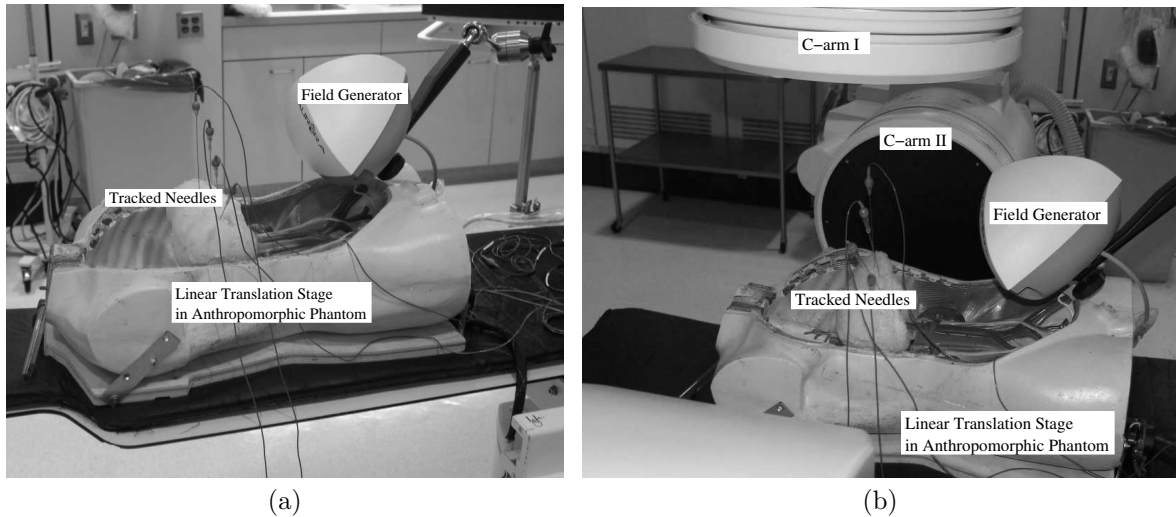(a)   (b)

Figure 2. Photographs of (a) baseline accuracy setup (b) bi-plane fluoroscopy in a typical imaging position over the range of motion (20mm).

3. EXPERIMENTAL RESULTS

To verify the validity of our approach we performed three experiments using a linearly translating stage (Bearing Engineers Inc., USA) whose accuracy is better than $0.1mm$. In each experiment we placed needles on the linear stage and translated it through ten positions with increments of $2mm$ between consecutive positions. This process was repeated twice in each of the experiments. We then computed two error measures, errors in distances between points and deviation of points from a straight line.

Distance errors were computed by comparing the known distances between all points and those obtained using the measurement method we were assessing, EM tracking or stereo-fluoroscopy. The deviation from a straight line was computed using Principle Component Analysis. As we know that the points are on a line we can perform a least squares fit of that line using PCA. The line is defined by the mean of the points and the first principle component, the direction of maximal variance. The point's distance from this line is the second error measure we use.

In the first experiment we assessed the accuracy of the 3D reconstruction obtained using bi-plane fluoroscopy. First the bi-plane fluoroscopes were calibrated. Then we placed three needles on the linear stage and translated it as described above. We then computed the two error measures. Our results show that the accuracy of stereo-fluoroscopy is better than $0.3mm$ when comparing distances and better than $0.7mm$ when comparing the deviation from the known direction of motion, confirming that stereo fluoroscopy is accurate enough for use as a validation for EM tracking. The results of this experiment are summarized in Table 1.
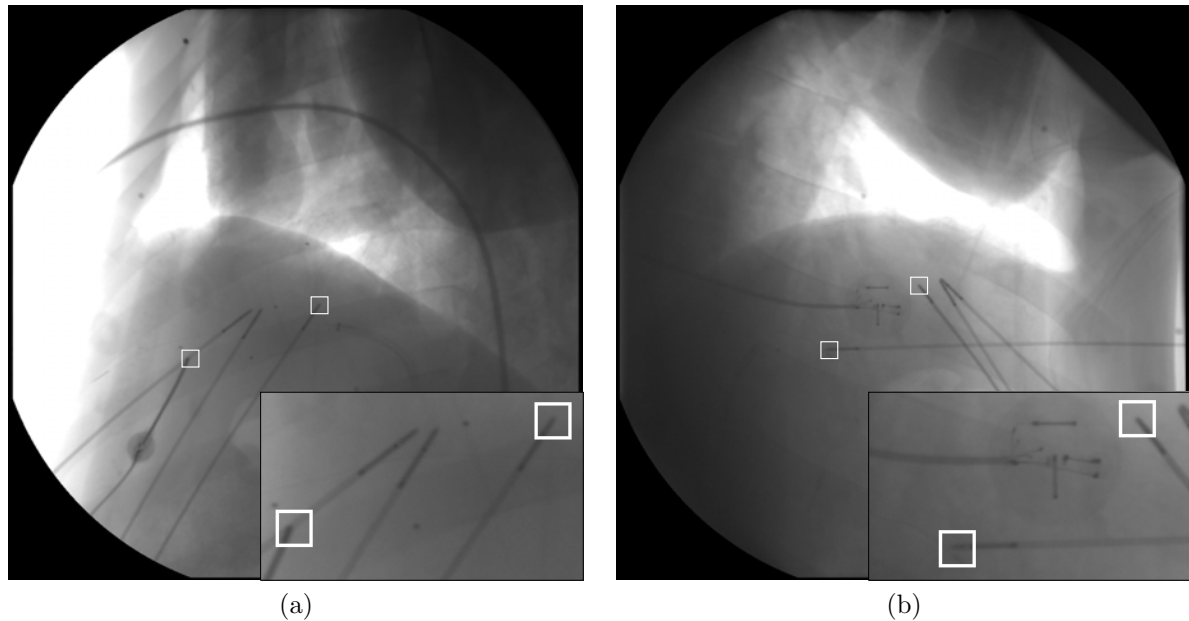
(a)   (b)

Figure 3. Pair of stereo images of electromagnetically tracked needles placed inside of swine liver. Boxes denote needle tips used for stereo reconstruction (zoomed version in insets).

The second experiment assessed the accuracy of the EM tracking system in the interventional suite under the best possible conditions and serves as our baseline. We placed four electromagnetically tracked needles on the linear stage, Fig. 2(a), and translated it as described above. At each position we acquired a reading from the tracking system. We then computed the two error measures. Our results show that the accuracy of the EM tracking system is better than $1.3mm$ when comparing distances and better than $0.2mm$ when comparing the deviation from the known direction of motion, confirming that EM tracking is accurate enough for our purposes. The results of this experiment are summarized in Table 2.

The third experiment assessed the effect of our validation method on the accuracy of the EM tracking system. As our method requires placing the bi-plane fluoroscopes in the vicinity of the EM field generator and tracked fiducials we expect it to effect the accuracy of the system.[12] We repeated the second experiment, only this time both C-arms were placed in the imaging setup which is used for stereo reconstruction, Fig. 2(b). The EM field generator was placed as close as possible to the tracked needles, within a clinically viable setup. Our results show that the accuracy of the EM tracking system is better than $1.5mm$ when comparing distances and better than $0.1mm$ when comparing the deviation from the known direction of motion. We conclude that although both C-arms are placed near the EM field generator and the tracked fiducials their effect on the system in this setup is negligible. The results of this experiment are summarized in table 3.

Finally, we performed a swine study, under an approved protocol, to validate the accuracy of EM tracking in a respiring animal. Four electromagnetically tracked needles were placed in a swine liver (Fig. 3). The animal was ventilated and we simultaneously acquired images with the fluoroscopes and readings from the EM tracking system. Three $40sec$ data sets were acquired. Only two of the four needles were used for stereo reconstruction as the tips of the other two needles were too close to each other and were overlapping in most images. We then aligned the stereo-fluoroscopy data to the EM tracking data as describe in section 2. Figure 4 shows an aligned data set for both needles. Our results show that the mean (std) distance between the stereo data and the EM tracking data for both needles is less than 1.4 (1.5)mm with a median of less than $0.8mm$. The maximal distance was less than $6.2mm$. This error is most likely due to the difference in sampling rates between the EM system (20Hz) and the stereo fluoroscopy system (6Hz) that leads to incorrect matches of points acquired during rapid respiratory motion. These initial results are promising, and suggest that direct tracking of internal organs using electromagnetically tracked fiducials in the interventional suite is possible.

Needle	Distance Error		Deviation From Straight Line	
	mean (std)	max	mean (std)	max
1	0.09 (0.09)	0.25	0.22 (0.13)	0.44
2	0.08 (0.06)	0.18	0.23 (0.09)	0.38
3	0.07 (0.06)	0.18	0.25 (0.16)	0.66

Table 1. Errors between known distances and those computed using stereo-fluoroscopy, and distances between computed points and the line corresponding to the first principle component. All measurements are in mm.

Needle	Distance Error		Deviation From Straight Line	
	mean (std)	max	mean (std)	max
1	0.5 (0.32)	1.2	0.04 (0.02)	0.06
2	0.19 (0.12)	0.52	0.02 (0.01)	0.03
3	0.14 (0.09)	0.37	0.03 (0.02)	0.09
4	0.26 (0.17)	0.64	0.06 (0.04)	0.12

Table 2. Baseline errors between known distances and those computed using data acquired by the EM tracking system, and distances between acquired points and the line corresponding to the first principle component. All measurements are in mm.

Needle	Distance Error		Deviation From Straight Line	
	mean (std)	max	mean (std)	max
1	0.6 (0.38)	1.4	0.03 (0.01)	0.05
2	0.23 (0.15)	0.56	0.02 (0.01)	0.03
3	0.2 (0.13)	0.49	0.04 (0.02)	0.07
4	0.12 (0.09)	0.32	0.04 (0.03)	0.09

Table 3. Effect of bi-plane fluoroscopes on accuracy of EM tracking. Errors between known distances and those computed using data acquired by the tracking system, and distances between acquired points and the line corresponding to the first principle component. All measurements are in mm.
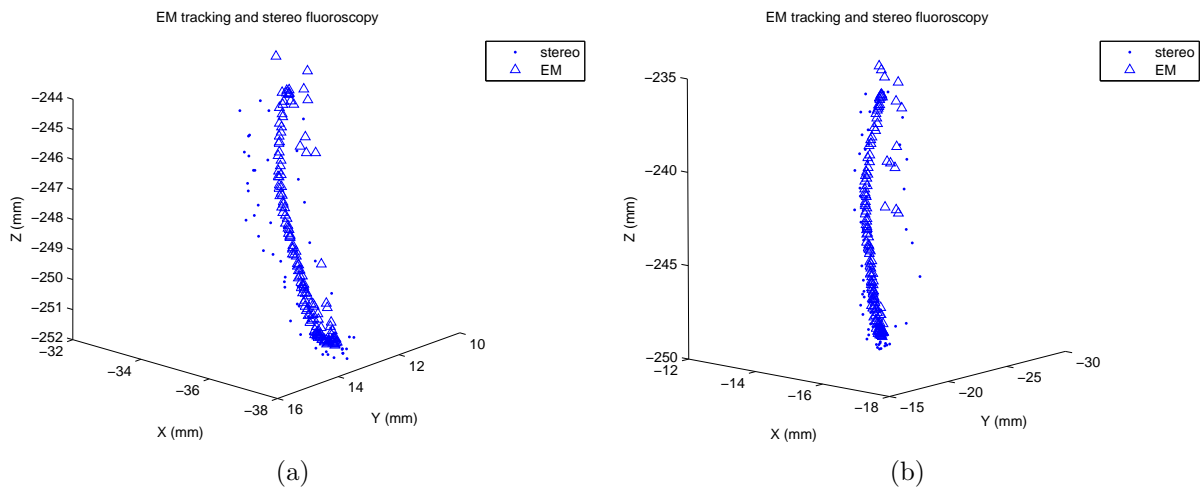

Figure 4. Data from stereo-fluoroscopy and EM tracking system after application of ICP alignment for two needles implanted in swine liver.

4. DISCUSSION AND CONCLUSIONS

Tracking target motion due to respiration is important for precise interventions in the regions of the abdomen and thorax. Respiratory induced motion in these regions can be up to several cm, severely limiting the accuracy of interventions which do not employ some type of tracking. We are currently investigating the use of EM tracked fiducials which will enable direct tracking of anatomy for extended periods of time. To validate the accuracy of the tracking we proposed to use stereo-fluoroscopy.

In this paper we have shown that stereo-fluoroscopy is accurate enough to serve as a validation mechanism for in-situ tracking, exhibiting sub-millimetric accuracy (errors below $0.7mm$). We have also shown that concurrent acquisition of fluoroscopic images and EM tracking data is possible, with a negligible effect on the accuracy of EM tracking due to the proximity of the C-arm frames (errors below $1.5mm$). Finally, we assessed the in-situ accuracy of EM tracking in a swine animal study using stereo fluoroscopy as our ground truth. Our results show a mean (std) difference of 1.4 (1.5)mm with a median of less than $0.8mm$, and a maximal difference $6.2mm$ between stereo fluoroscopy and EM tracking. This maximal error is most likely due to erroneous point matches arising from points sampled during rapid respiratory motion.

ACKNOWLEDGMENTS

REFERENCES

1. K. Cleary, M. Mulcahy, R. Piyasena, T. Zhou, S. Dieterich, S. Xu, F. Banovac, and K. Wong, "Organ motion due to respiration: the state-of-the-art and applications in interventional radiology and radiation oncology," in *SPIE Medical Imaging: Visualization, Image-Guided Procedures, and Display*, pp. 53–59, 2005.
2. M. A. Clifford, F. Banovac, E. Levy, and K. Cleary, "Assesment of hepatic motion secondary to respiration for computer assisted interventions," *Computer Aided Surgery* **7**(5), pp. 291–299, 2002.
3. J. Brewer, M. Betke, D. P. Gierga, and G. T. Chen, "Real-time 4D tumor tracking and modeling from internal and external fiducials in fluoroscopy," in *Medical Image Computing and Computer-Assisted Intervention*, pp. 594–601, 2004.
4. M. Murphy, "Tracking moving organs in real time," *Seminars in Radiation Oncology* **14**(1), pp. 91–100, 2004.
5. C. Ozhasoglu and M. J. Murphy, "Issues in respiratory motion compensation during external-beam radiotherapy," *Int. J. Radiation Oncology Biol. Phys.* **52**(5), pp. 1389–1399, 2002.
6. V. Venkatraman, M. H. V. Horn, S. Weeks, and E. Bullitt, "Liver motion due to needle pressure, cardiac, and respiratory motion during the TIPS procedure," in *Medical Image Computing and Computer-Assisted Intervention*, pp. 66–72, 2004.
7. H. Shirato *et al.*, "Physical aspects of a real-time tumor-tracking system for gated radiotherapy," *Int. J. Radiat. Oncol. Biol. Phys.* **48**(4), pp. 1187–1195, 2000.
8. A. Schweikard, G. Glosser, M. Bodduluri, M. J. Murphy, and J. R. Adler, "Robotic motion compensation for respiratory movement during radiosurgery," *Computer Aided Surgery* **5**(4), pp. 263–277, 2000.
9. A. Schweikard, H. Shiomi, and J. Adler, "Respiration tracking in radiosurgery without fiducials," *Int. J. Medical Robotics and Computer Assisted Surgery* **1**(2), pp. 19–27, 2005.
10. E. Wilson, H. Zhang, and K. Cleary, "Electromagnetic tracker accuracy in cyberknife suite," in *SPIE Medical Imaging: Visualization, Image-Guided Procedures, and Display*, 2006.
11. S. Schreiner, J. Funda, A. C. Barnes, and J. H. Anderson, "Accuracy assessment of a clinical biplane fluoroscope for three-dimensional measurements and targeting," in *SPIE Medical Imaging: Image Display*, pp. 160–166, 1997.
12. J. Hummel, M. Figl, C. Kollmann, H. Bergmann, and W. Birkfellner, "Evaluation of a miniature electromagnetic position tracker," *Med. Phys.* **29**(10), pp. 2205–2212, 2002.

13. J. B. Hummel, M. R. Bax, M. L. Figl, Y. Kang, C. Maurer, Jr., W. W. Birkfellner, H. Bergmann, and R. Shahidi, "Design and application of an assessment protocol for electromagnetic tracking systems," *Med. Phys.* **32**(7), pp. 2371–2379, 2005.

14. K. Schicho, M. Figl, M. Donat, W. Birkfellner, R. Seemann, A. Wagner, H. Bergmann, and R. Ewers, "Stability of miniature electromagnetic tracking systems," *Phys. Med. Biol.* **50**(9), pp. 2089–2098, 2005.

15. H. Livyatan, Z. Yaniv, and L. Joskowicz, "Robust automatic c-arm calibration for fluoroscopy-based navigation: a practical approach," in *Medical Image Computing and Computer-Assisted Intervention*, pp. 60–68, 2002.

16. P. M. Tate *et al.*, "Performance and robustness of automatic fluoroscopic image calibration in a new computer assisted surgery system," in *Medical Image Computing and Computer-Assisted Intervention*, pp. 1130–1136, 2001.

17. R. I. Hartley and A. Zisserman, *Multiple View Geometry in Computer Vision*, Cambridge University Press, 2000.

18. P. J. Besl and N. D. McKay, "A method for registration of 3d shapes," *IEEE Trans. Pattern Anal. Machine Intell.* **14**(2), pp. 239–255, 1992.